Master of Science Thesis

Multiscale Modeling of the Effect of sub-ply voids on the failure of composites

A Progressive Failure Model

G. de Jong

Faculty of Aerospace Engineering · Delft University of Technology

Multiscale Modeling of the Effect of sub-ply voids on the failure of composites

A Progressive Failure Model

Master of Science Thesis

For obtaining the degree of Master of Science in Aerospace Engineering at Delft University of Technology

G. de Jong

February 12, 2018

Faculty of Aerospace Engineering · Delft University of Technology

Delft University of Technology
Faculty of Aerospace Engineering
Department of Aerospace Structures and Materials

GRADUATION COMMITTEE

Dated: February 12, 2018

Chair holder: Dr. S. R. Turteltaub

Committee members: Dr. B. Chen

Dr. Ir. F.P. van der Meer

Abstract

To reduce the weight of aerospace structures, composite materials are used more and more often. These composite structures have complicated fracture patterns and the fracture properties show a large influence by the manufacturing process. This is mainly caused by the defects that can develop during the manufacturing of the composites. To know the effect of the defects on the fracture properties of the composite is of vital importance. This project was carried out to determine the effect of sub-ply voids on the macroscopic fracture properties. For this, a comprehensive parametric study on the different microscopic void parameters is performed using a multiscale method.

The multiscale method as developed by Turteltaub et al. [53] was adapted to determine the effect of sub-ply voids on the macroscopic fracture properties. The defects are discretely modeled on the microscale. The microscopic information is determined using numerical simulations of a 2-Dimensional (2D) volume element. A computational homogenization technique is then applied to determine the effect of the sub-ply voids on the macroscopic fracture. The macroscopic fracture is defined using an effective traction separation law.

The fracture in the volume element is modeled using zero thickness cohesive interface elements. These cohesive elements are embedded between the continuum elements throughout the whole computational domain. The volume element contains random distributed carbon fibers and voids in an epoxy. A random mesh is applied to this volume element to reduce the mesh dependency of the cohesive elements on the fracture. Periodic boundary conditions are applied to ensure the volume element is part of a larger structure. This geometry and the boundary conditions are inserted into a `Abaqus`® input file. The input file is executed on the Delft University of Technology computational cluster.

Due to the computational limitations a Microstructural Volume Element (MVE) size of $75 \times 75\mu$m was used in this research. It was assumed that the trends that are found at this MVE size are similar to that of the Representative Volume Element (RVE) size. Three different void cases were studied. Firstly a baseline case was selected of matrix voids with nearly constant diameter. Secondly the microstructure contained both interfiber voids, which are gaps between fibers, and matrix voids. These gabs between fibers are created due to the resin being unable to flow between the fibers. This case was used to determine the effect of

the different type of voids on the effective properties. Lastly a microstructure with a large deviation in the matrix void diameter was studied. Using this case and the constant diameter void case, the size effect of the matrix voids was investigated.

For each void case the void content is increased from 0 to 8 %. In all three void cases for a pure shear and mixed mode loading case, both the effective tangential fracture energy and strength decrease with increasing void content. A critical value can be observed for these tangential properties, at which below this critical void content no effect of the effective properties is found. For the constraint extension case only the effective energy decreases and no critical value is observed.

When comparing the three void cases, the effective properties were within standard deviation of each other with increasing void content. It is concluded that the void content is the main variable when determining the effect of sub-ply voids on the effective properties. The type of voids and the size of the voids show to be only a second order effect on the effective properties.

Table of Contents

List of Figures

List of Tables

List of Acronyms

1D	1-Dimensional
2D	2-Dimensional
3D	3-Dimensional
BVP	Boundary Value Problem
CFRP	Carbon Fiber Reinforced Plastic
CZM	Cohesive Zone Model
DOF	Degree of Freedom
ETSL	Effective Traction Separation Law
FE	Finite Element
FEM	Finite Element Method
FRP	Fiber Reinforced Plastic
LEFM	Linear Elastic Fracture Mechanics
MVE	Microstructural Volume Element
PBC	Periodic Boundary Conditions
RoM	Rule of Mixtures
RVE	Representative Volume Element
SEM	Scanning Electron Microscope
SVD	Singular Value Decomposition
TSL	Traction-Separation Law
TU Delft	Delft University of Technology

List of Symbols

Greek Symbols

$\bar{\epsilon}$	Applied strain tensor
Γ	Crack surface
Ω	Microscopic domain
$\partial\Omega$	External boundary of the microscopic domain
α	Correction factor for the Hill-Mandel condition
$\boldsymbol{\sigma}$	Strain tensor

Latin Symbols

$\boldsymbol{m}$	Crack normal
$\boldsymbol{m}^v$	Void boundary normal
$\boldsymbol{t}$	Tracion vector
$\boldsymbol{u}$	Displacement vector
$[\![\boldsymbol{u}]\!]$	Crack opening
$[\![\dot{\boldsymbol{u}}]\!]$	Crack opening rate
$()^f$	Effective properties
G	Fracture energy
N_R	Number of realizations
P	Rate of work
S_d	Deviation of the void size
V_C	Void content

Operators

$\mathrm{div}\,(\mathbf{A})$ $\nabla \cdot \mathbf{A}^T = \frac{\partial T_{ij}}{\partial x_j}$

div $(\mathbf{a})$ $\nabla \cdot \mathbf{a} = \frac{\partial a_i}{\partial x_i}$

grad $(\mathbf{A})$ $\nabla \mathbf{A} = \frac{\partial A_{ij}}{\partial x_k}$

grad $(\mathbf{a})$ $\nabla \mathbf{a} = \frac{\partial a_i}{\partial x_j}$

$\mathbf{AB}$ $A_{ij}B_{jk}$

$\mathbf{Ab}$ $A_{ij}b_j$

$\mathbf{A} \cdot \mathbf{B}$ $A_{ij}B_{ij}$

$\mathbf{a} \otimes \mathbf{b}$ $a_i b_j$

Acknowledgments

First, I would like to express my gratitude to my thesis supervisor Dr. Sergio Turteltaub. His guidance and support throughout the thesis and his broad knowledge on the subject of fracture and solid mechanics has helped me tremendously. Dr. Turteltaub always put a lot of time and effort in this project and has been a huge support.

Secondly, I would like to thank my girlfriend, Eva Raquel Schenk, for her help proofreading and her support throughout the thesis. I would also like to thank my friends Bas de Rooij and Ties Delnooz for there help on the report by proofreading and teaching me Abobe illustrator.

Finally, I would also like to acknowledge Christian Hirsch and Rubén Suárez Millán. We were working on similar projects using the same multiscale theory. The discussion with them helped each solve the individual problems and develop new ideas for the multiscale theory.

Delft, University of Technology G. de Jong
February 12, 2018

Chapter 1

Introduction

In the aerospace industry, there is an increasing interest in composite structures. As composite materials enable significant weight savings compared to the conventional metals. This is mainly attributed to their high specific strength and stiffness. These weight savings result in fuel savings and thus more efficient structures and lower cost. Both Boeing and Airbus are currently developing high end composite airplanes, with for instance the Airbus A350 XWB. Over 50% of the complete aircraft structural weight is made of composite material. This shows the importance of the fiber reinforced composites and their potential. The Carbon Fiber Reinforced Plastic (CFRP) is the mainly used composite. This composite consists of two materials, the carbon fibers and an epoxy. The combination of these two materials exploits the strong points of each constituent. The carbon fiber ensures the strength and stiffness of the material and the epoxy ensures the toughness, protection and support for the fibers. Due to the combination of the two components, the failure mechanisms are more complicated when comparing them to conventional metals. The complex failure mechanisms are often caused by the difference in properties of the two constituents such as fiber/matrix interface.

The properties of the composite show a large influence on the manufacturing parameters. This is caused by the difficulty and uncertainty which is caused by manufacturing the two constituents together. In this case, random and undesired defects can form. These defects can range from large dry spots on the composite to microvoids in the matrix. The influence of these defects on the macroscopic response, and especially the failure of the composite is important to know. Currently, this is mainly determined using extensive and expensive testing procedures. However, due to the computational possibilities of today, an increasing focus is on the computational modeling and prediction of failure. To model the complete model with both the macro and micro structure modeled discretely is computationally expensive and requires multiple processes to take the fiber distribution and defects into account. The multiscale concept couples the macro and micro structure using a homogenization technique, which uses the effective behavior of the fine scale for the response of the larger scale. This concept enables the development for a failure prediction based on the micromechanical behavior of the composite. Research of advanced multiscale methods that allow fracture have been proposed.

However, these new methods are often only able to simulate simple loading cases and defects are often neglected.

A new multiscale approach was developed in Turteltaub et al. [53]. In this research the Effective Traction Separation Law (ETSL) is determined from the microscale fracture using a computational homogenization technique with a Representative Volume Element (RVE). Using this method, there are no restrictions to the loading conditions or formation of the crack. This thesis will apply this method and adapt it further to take microscopic defects into account. The objective is formulated as followed:

The objective of this MSc. Thesis it to determine the influence of sub-ply defects and its parameters to a micromechanically derived Traction-Separation Law (TSL), by using multiscale modeling with a computational homogenization technique and a cohesive zone damage model.

To complete this objective, the multiscale framework that is used contains a Cohesive Zone Model (CZM) with embedded zero-thickness interface elements on the microscale, from which the effective fracture properties can be determined. The microscopic analysis is using a RVE, which definition is explained later in this thesis. The objective can be divided into four sub-objectives:

- Create the Microstructural Volume Element (MVE), which captures the composite microstructure in the transverse plane containing the representative microvoids in a Finite Element (FE) model
- Adapt the current multiscale method to take microvoids into account
- Determine the RVE size by using a convergence study
- Determine the ETSL properties as a function of the microvoid parameters

The structure of the reports is as follows: In Chapter 2 a comprehensive literature review is given and the summary of the literature study [15]. Three theories that are relevant to this project are discussed here, which are the microvoids, CZM and multiscale analysis. The theory that is used throughout this project is presented in Chapter 3. The numerical implementation of this theory is discussed in Chapter 4. This numerical implementation is verified and the RVE convergence is done in Chapter 5. The results of the study on the influence of the void parameters on the ETSL are presented and discussed in Chapter 6. Finally, the conclusion and recommendations are presented in Chapter 7.

Chapter 2

Literature Review

In this chapter the literature review is discussed. It covers all the aspects that are of interest for this thesis and summarizes the literature study [15]. First the defects that are present on the sub-ply level of a fiber-reinforced composite are discussed in Section 2.1. The Cohesive Zone Model (CZM) is elaborated on in Section 2.2. The multiscale analysis which is required for this study is discussed in Section 2.3. Finally a conclusion of the literature is discussed in Section 2.4.

2.1 Defects in composites

There are several types of defects present on the microscopic sub-ply level of a fiber-reinforced composite. In this study only microvoids or porosities are evaluated and discussed. The issue with microvoids is that they are still hard to investigate using the current experimental methods. The two main methods used to determine properties of the microvoids are Scanning Electron Microscope (SEM) and Micro-CT. The effect of voids on the macroscopic properties of a fiber-reinforced composite has been extensively researched and has been established that the voids have a large effect on the fracture properties. Although this effect is often only found after the void content exceeds a critical value, this critical value is still a debated value. For instance Tang et al. [51] states that the critical void content is around 3 - 4 % for the compressive and shear properties, while Jeong [30] using a fracture mechanics approach suggests it is 1 %.

2.1.1 Void morphology and distribution

In Figure 2.1 and Figure 2.2 examples of the microstructure of fiber reinforced composites can be found [13, 50]. Although Figure 2.2 is a CAS/Sic-carbon composite, the voids between the fibers are similar to that of a carbon fiber with an epoxy matrix. Another example can be found by in Figure 2.3. Similar to Figure 2.2 voids trapped between the fibers can be found. This is caused by the fibers blocking the resin to flow properly between the fibers [59, 57].

The type of voids that are thus present on a microscale level are matrix voids and gaps between the fibers, which are called interfiber voids throughout this study.

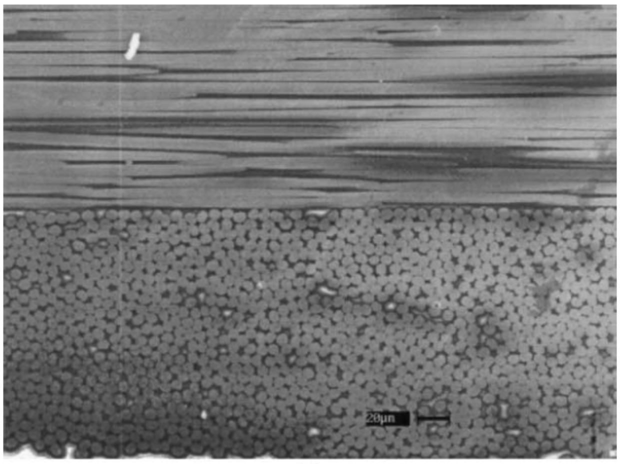

Figure 2.1: Voids found in a 0 and 90 ply using SEM image analysis. Here, the voids are white, the fibres are gray and the matrix is black [13]

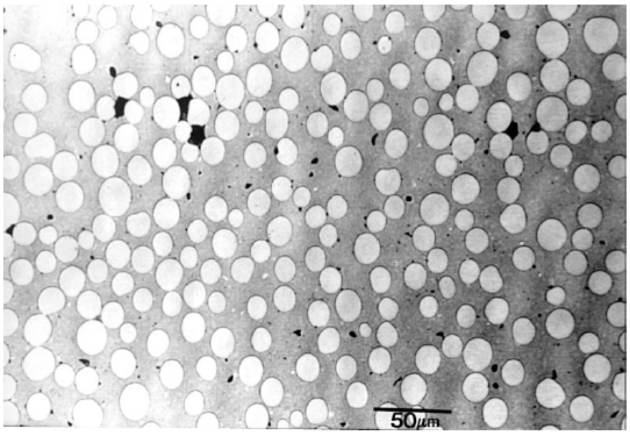

Figure 2.2: Typical micro-voids found using optical micrograph, it can be seen here that two dominate type of voids are present: voids between fibres and voids in the matrix [50]

For a parametric determination of the void property distributions, three studies have been used. The research of Chambers et al. [8] inspected several aerospace quality composites using image analysis. Here, a distribution of the transverse parameters have been made. This distribution has been divided into four different groups of void areas, as is shown in Table 2.1. An example of type 1 and 2 voids are shown in Figure 2.4. Type 1 voids are the most common, with around 65 % of the total void content. The contribution of the void type decreases with increasing of size. Type 1 voids have a lower bound due to the fact that voids of a lower area are assumed to not have an influence on the properties [8]. Although, voids of a smaller cross sectional area are in fact present in the composite.

Not only the size was investigated in Chambers et al. [8], also the distribution of the aspect ratio was determined as is shown in Table 2.2.

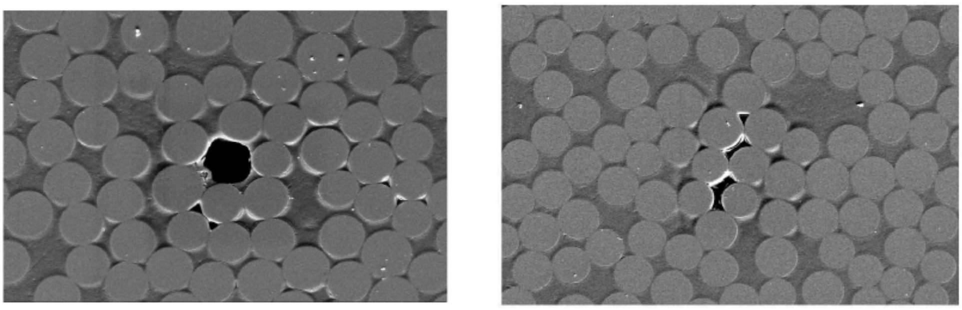

(a) **(b)**

Figure 2.3: SEM image of a Glass fibre/epoxy laminate done. Here the two typical voids can be found [56]

Table 2.1: Void areas split into groups in an uni-directional laminate [8]

Type	Cross sectional area
1	$8 \cdot 10^{-6} < V < 0.004$ mm^2
2	$0.004 < V < 0.01$ mm^2
3	$0.01 < V < 0.03$ mm^2
4	$V > 0.03$ mm^2

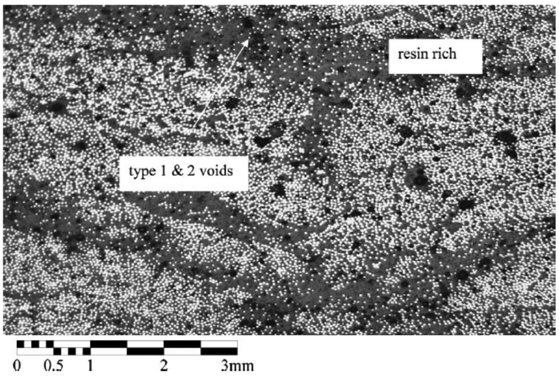

Figure 2.4: Void distribution of type 1 and type 2 in a high quality laminate [8]

The research as presented in Maragoni et al. [36] assumes that in the transverse direction, all the voids are circular. This results in the distribution of the void properties as shown in Figure 2.5. In this figure it can be found that the voids are 'cigar shaped' with the ellipse shape of the void in the longitudinal direction. It can be clearly seen that the void diameter has a Weibull distribution.

Hamidi et al. [24] looked at the correlation between the shape of the voids and the size of the voids. Small voids have an equivalent diameter lower than 50μm, medium voids 50 *to* 100μm, and large voids above 100μm. The void shape is also dependant on the void size. Irregular shaped voids are the most common on the small scale, with both cirular and elliptical voids also being present.

From these three researches it can be found that there is actually no universal characterization

Table 2.2: Distribution of aspect ratio's independent of void content [8]

Aspect Ratio	Percentage [%]
$AR < 1$	0 - 5
$1 < AR < 2$	70 - 80
$2 < AR < 4$	15 - 20
$AR > 4$	0 - 2

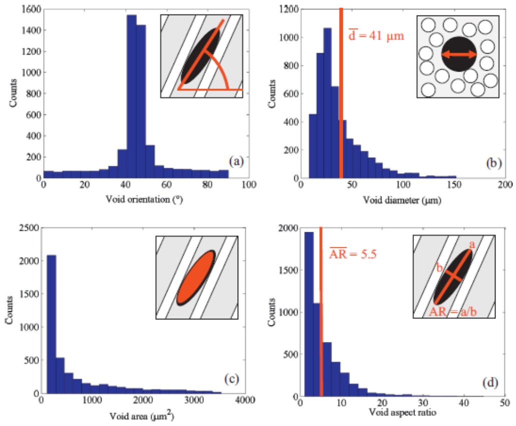

Figure 2.5: Void Characteristics according to Maragoni et al. [36] using a 45 degree ply

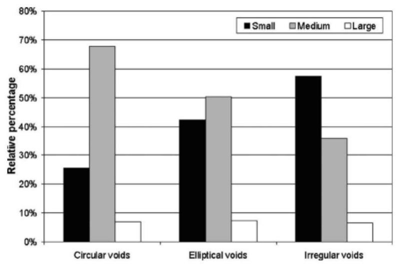

Figure 2.6: Void shape with respect to the size of the voids [24]

of the void parameters on the microscale due to the difficulty in investigating this scale. In this research the focus will lie on the 'type 1' voids, as presented by Chambers et al. [8], as these are on the microscale. The focus will lie on voids with an area equal or lower to that of the fiber present in the composite. The transverse aspect ratio is assumed to be low as is presented by both Chambers et al. [8] and Maragoni et al. [36], resulting in a range between 1 and 1.4. The orientation of these voids are random. In aerospace graded composites a void content below $1-2\%$ is required, while for other applications such as the automotive industry a void content up to 5% is acceptable [22]. In order to determine the detrimental effect of the voids on the microscale, even higher void contents can be investigated.

2.1.2 Numerical examples

Most numerical researches have the voids models on a mesoscale. On this scale the individual fibers are often not modeled [35, 66, 29]. The assumptions for the void characteristics made for these models can be useful for this study.

Lin et al. [35] uses three different parameters to model the voids: the auto-correlation length, the roughness factor and the variance. The influence of these parameters can be found in Figure 2.7. These three parameters enable the possibility to create completely random void shapes. Computationally, these random shapes are difficult to model and result in very fine meshes and hard to converge models when using conventional Finite Element Method (FEM).

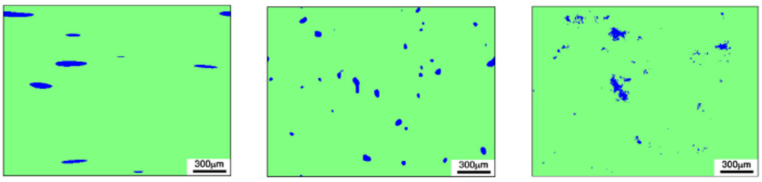

(a) **(b)** **(c)**

Figure 2.7: Voids in blue, composite in Green. (a) High aspect ratio (autocorrelation length) (b) standard settings (c) high roughness factor [35]

Other research assumed circular voids, as is for instance presented by Yu et al. [66]. It was found that the void distribution had a effect on the material properties on the meso scale. In Huang and Talreja [29] it was assumed that the voids are periodically distributed in the material, resulting in the model as shown in Figure 2.8 which uses a unit cell to do a 3-Dimensional (3D) parametric study on the voids parameters.

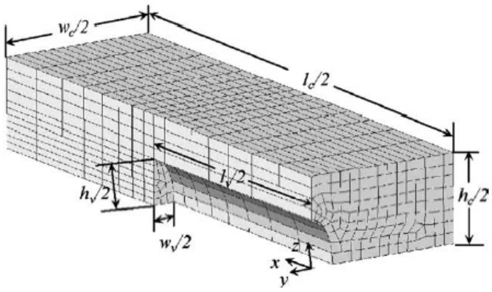

Figure 2.8: Periodic volume cell with a void. Here, a parametric study is done on the geometry of the void [29]

Voids on the micro structure were investigated by Vajari et al. [59, 58]. Here, both the fibers and voids were explicitly modeled. Both studies consisted of a model that contained randomly distributed circular matrix voids and interfiber voids, as was observed previously. The model can be found in Figure 2.9.

This study found that the microscopic voids have a large influence on both the macroscopic strength and propagation of damage. Small microvoids mainly have an influence on the crack path, while large microvoids are decisive for crack initiation [59].

2.2 Cohesive zone model

The fracture mechanics that is used here is the CZM. The CZM is created to overcome some of the issues of the Linear Elastic Fracture Mechanics (LEFM), which are discussed below.

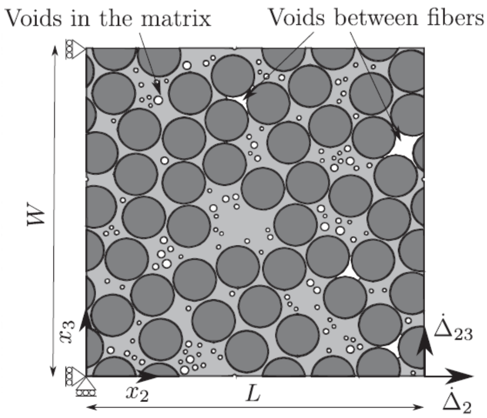

Figure 2.9: Voids modeled in the microscale, containing both voids in the matrix and voids entrapped by fibres [59]

LEFM is a suitable method when the material is brittle and the fracture process zone is small while the global bulk material behaves elastic. However, when the process zone is large, the theory is not valid anymore. Also, when complex failure processes occur, it is difficult to do a parametric study on this. This results in the fact that this method is not valid for this study [46] and the CZM is suitable.

The cohesive zone model overcomes the issue at the process zone. This method can be applied to various materials and structures and enables the combination of both the crack initiation and propagation [17]. Another advantage is its easy incorporation in FEM. The following section will discuss the general theory of the CZM, and its implementation in the FEM.

2.2.1 General Theory

In the classical LEFM, a crack singularity occurs near the crack tip. If the cohesive zone near the crack tip becomes larger than the characteristic length, the assumptions of LEFM do not hold anymore. The equation for the characteristic can be found in Equation (2.1). Here, Γ is the fracture toughness, E is the characteristic elastic modulus. If this is thus larger than the characteristic length, a cohesive zone can then be used to replace the singularity region by introducing a lateral region with non-linear phenomena [2].

$$l^* = \frac{E\Gamma}{\sigma_c^2} \tag{2.1}$$

The theory of the CZM was first introduced by Dugdale [16] and Barenblatt [4]. Dugdale [16] developed the method for materials with yielding near the crack tip and Barenblatt [4] developed a method for brittle materials. Both use the CZM to describe the damage near and ahead of the crack tip. Here the assumptions is that voids form ahead of the crack tip, as is shown in Figure 2.10 at the top left [12]. This void formation ahead of the crack tip results in that less stress can be transferred ahead of the crack tip. This traction ahead of the crack tip is idealized using a cohesive law or Traction-Separation Law (TSL), which is shown in the left bottom image in Figure 2.10. The TSL is explained in greater detail in the next section, where the shape of the TSL is different as is shown in the right side of Figure 2.10. The numerical implementation, as shown in the middle of Figure 2.10, is discussed after the TSL.

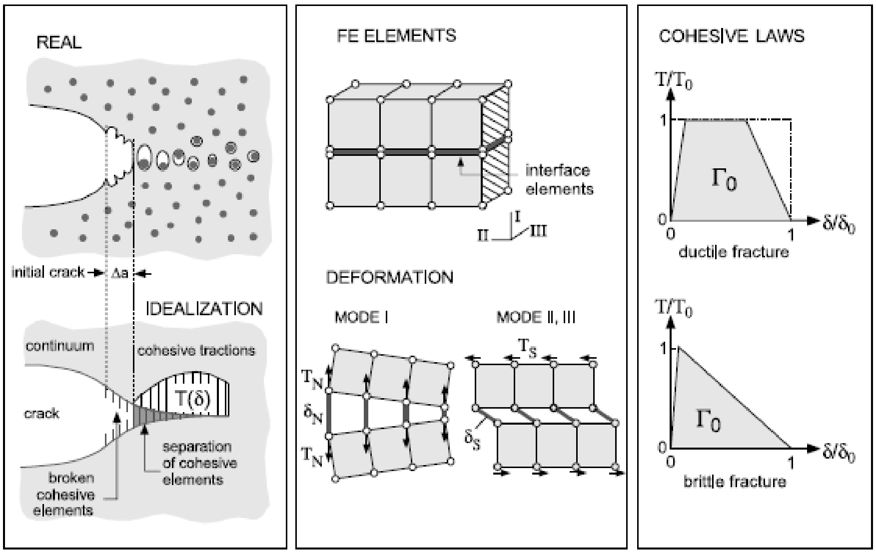

Figure 2.10: The basic concept of the CZM: first on the left the idealization of the real physical problem by the cohesive zone is shown, after which the different modes in FEM models in the middle and on the right some possible cohesive laws [12].

2.2.2 Traction Separation Laws

The TSL is the constitutive relation of the CZM and is used to describe the separation mechanics of the CZM. Different shapes of the TSL are possible. The TSL can be divided into potential based and non-potential based models. The non-potential based methods are dependent on the effective displacement and are relatively simply defined. For the potential based model the TSL is derived from the potential of the fracture energy and its derivatives. This results in a more complicated function but does overcome some limitations of the non-potential based models.

Another difference in the TSL is whether is it an intrinsic or extrinsic model. Here the intrinsic models have an initial traction of zero and because of this have an initial elastic loading. The extrinsic models have an initial traction which is non-zero.

Examples of both intrinsic and extrinsic TSLs can be found in Figure 2.11. The shape of the TSL has to be selected to ensure the proper idealization of the damage model in front of the crack.

A problem of the non-potential based models are that non-physical behavior can occur in Abaqus® since often no negative tangential stiffness within the linear softening region is provided in the model [44]. It is advised that the traction-separation relations have to be selected with care when dealing with mixed-mode failure.

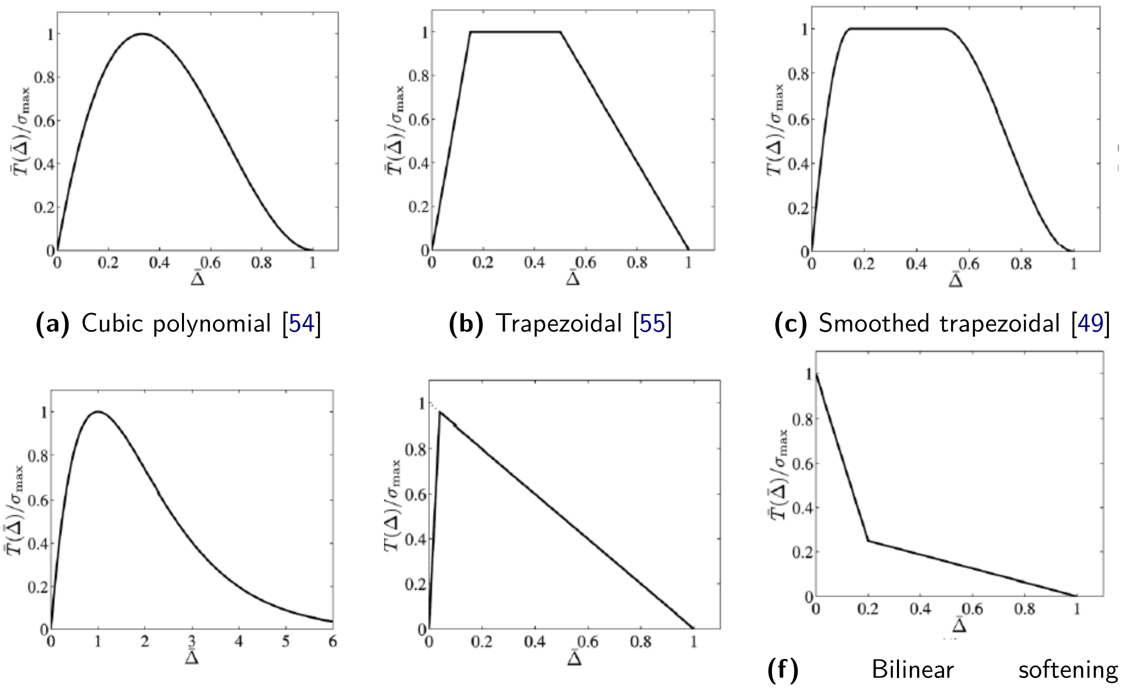

(a) Cubic polynomial [54] **(b)** Trapezoidal [55] **(c)** Smoothed trapezoidal [49]

(d) Exponential [41] **(e)** Linear softening [20, 7, 18] **(f)** Bilinear softening (extrinsic)[45, 65]

Figure 2.11: Different shape of the TSL[43]

2.2.3 Numerical Implementations

The numerical implementation of the CZM in an FEM is usually done using cohesive elements. These cohesive elements have zero thickness and are placed between the continuum elements [39]. The implications and influence of this are discussed below.

Cohesive Element

The cohesive element which is used for the numerical implementation of the CZM is presented in this section. Here, the method of the cohesive element in FEM is mainly discussed. The governing equations of the finite element formulation including the equilibrium equation, natural and essential boundary conditions and the traction continuity are defined as [39]

$$\nabla \cdot \boldsymbol{\sigma} + \boldsymbol{b} = 0 \qquad \boldsymbol{x} \in \Omega \tag{2.2a}$$

$$\boldsymbol{n} \cdot \boldsymbol{\sigma} = \bar{\boldsymbol{t}} \qquad \boldsymbol{x} \in \Gamma_t \tag{2.2b}$$

$$\boldsymbol{u} = \bar{\boldsymbol{u}} \qquad \boldsymbol{x} \in \Gamma_u \tag{2.2c}$$

$$\boldsymbol{n}_d^+ \cdot \boldsymbol{\sigma} = \boldsymbol{t}_c^+; \quad \boldsymbol{n}_d^- \cdot \boldsymbol{\sigma} = \boldsymbol{t}_c^-; \quad \boldsymbol{t}_c^+ = -\boldsymbol{t}_c = -\boldsymbol{t}_c^- \qquad \boldsymbol{x} \in \Gamma_d \tag{2.2d}$$

where $\boldsymbol{\sigma}$ is the Cauchy stress tensor, $\boldsymbol{u}$ the displacement field and $\boldsymbol{b}$ the body force vector.

The weak formulation of these governing equations is found as[5].

$$\delta W^{\text{ext}} = \delta W^{\text{int}} + \delta W^{\text{coh}} \tag{2.3a}$$

$$\delta W^{\text{ext}} = \int_{\Omega} = \delta \boldsymbol{u} \cdot \boldsymbol{b} \, \mathrm{d}\Omega + \int_{\Gamma_t} \delta \boldsymbol{u} \cdot \tilde{\boldsymbol{t}} \, \mathrm{d}\Gamma_t \tag{2.3b}$$

$$\delta W^{\text{int}} = \int_{\Omega} \nabla^s \delta \boldsymbol{u} : \boldsymbol{\sigma} \, \mathrm{d}\Omega \tag{2.3c}$$

$$\delta W^{\text{coh}} = \int_{\Gamma_d} \delta [\![\boldsymbol{u}]\!] \cdot \boldsymbol{t}^{\text{c}} \, \mathrm{d}\Gamma_d \tag{2.3d}$$

where $[\![\boldsymbol{u}]\!]$ is the displacement jump of the cohesive crack. The external work is a function of the internal work and the cohesive work. The solid that contains a cohesive crack can be found in Figure 2.12. For the discretization of the bulk, 2-Dimensional (2D) standard continuum elements are used. The crack is discretized using 1-Dimensional (1D) interface elements of zero thickness. This is visualized in Figure 2.13 [38].

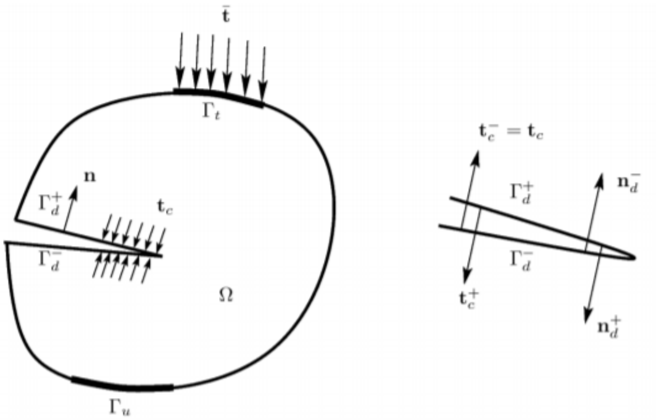

Figure 2.12: A 2D solid that contains a cohesive crack [39]

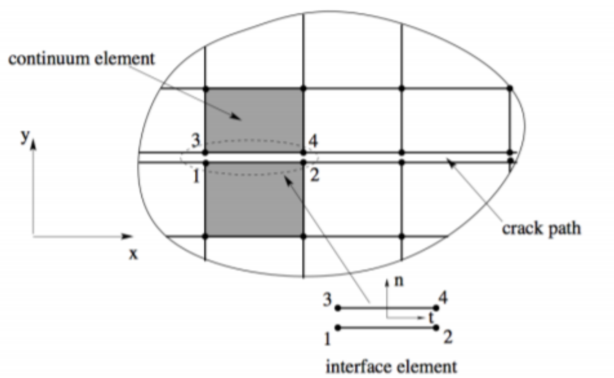

Figure 2.13: Discretization of the solid into continuum elements and zero-thickness interface elements [39]

The displacements of the interface element can be split for the nodes 1-2 (lower bound) and node 3-4 (upper bound) and are as

$$\boldsymbol{u}^{+} = \boldsymbol{N}^{\text{int}}\boldsymbol{u}^{+} \tag{2.4a}$$
$$\boldsymbol{u}^{+} = \boldsymbol{N}^{\text{int}}\boldsymbol{u}^{+} \tag{2.4b}$$

where N^{int} is the matrix of the shape functions for a 4-node element as

$$\boldsymbol{N}^{\text{int}} = \begin{bmatrix} N_1 & 0 & N_2 & 0 \\ 0 & N_1 & 0 & N_2 \end{bmatrix}. \tag{2.5}$$

Using the displacement of the upper and lower bound of the interface element, the displacement jump of the element can be computed as

$$[\![\boldsymbol{u}]\!] = \boldsymbol{u}^{+} - \boldsymbol{u}^{-} = \boldsymbol{N}^{\text{int}}\left(\boldsymbol{u}^{+} - \boldsymbol{u}^{-}\right). \tag{2.6}$$

The displacement of the continuum elements and the virtual displacement are given by

$$\boldsymbol{u} = \boldsymbol{N}\boldsymbol{u} \tag{2.7a}$$
$$\delta\boldsymbol{u} = \boldsymbol{N}\delta\boldsymbol{u}. \tag{2.7b}$$

Using Equation (2.7), Equation (2.6) and substituting these equations into the weak form as found in Equation (2.3), the relation between the forces follows as

$$f^{\text{ext}} = f^{\text{int}} + f^{\text{coh}} \tag{2.8}$$

where f^{ext}, f^{int} and f^{coh} are the external, internal and cohesive force respectively. The internal and external force are computed using the continuum elements of the bulk material, which are denoted using the subscript x_e, and can be found as

$$f_e^{\text{int}} = \int_{\Omega_e} \boldsymbol{B}^T\boldsymbol{\sigma}\,\mathrm{d}\Omega_e \tag{2.9a}$$
$$f_e^{\text{ext}} = \int_{\Omega_e} \boldsymbol{N}^T\boldsymbol{b}\,\mathrm{d}\Omega_e + \int_{\Gamma_{\text{t}}^e} \boldsymbol{N}^T\boldsymbol{t}\,\mathrm{d}\Gamma_{\text{t}}^e. \tag{2.9b}$$

For the cohesive force vector, the subscript x_{ie} is used, since the interface elements are used to determine this force. This cohesive force is a combination of the upper and lower bound as

$$f_{ie,+}^{\text{coh}} = \int_{\Gamma_d} \left(N^{\text{int}}\right)^T \boldsymbol{t}^c\,\mathrm{d}\Gamma_d \tag{2.10a}$$
$$f_{ie,-}^{\text{coh}} = -\int_{\Gamma_d} \left(N^{\text{int}}\right)^T \boldsymbol{t}^c\,\mathrm{d}\Gamma_d. \tag{2.10b}$$

It is assumed in this case, that the nonlinear process is concentrated only on the cohesive crack and thus the bulk is a linear elastic material. The cohesive crack is modeled with a TSL of which the constitutive equations in rate form as

$$\dot{\boldsymbol{\sigma}} = \boldsymbol{D}\dot{\boldsymbol{\epsilon}} \tag{2.11a}$$

$$\dot{\boldsymbol{t}}^c = \boldsymbol{T}[\![\dot{\boldsymbol{u}}]\!] \tag{2.11b}$$

where $\boldsymbol{D}$ is the elasticity matrix and $\boldsymbol{T}$ is the cohesive tangent matrix, which is dependent on the shape of the TSL, as explained previously. Then, by linearization of the internal force, as presented in Equation (2.9a), the tangent stiffness matrix is found as

$$\boldsymbol{K}_c = \int_\Omega \boldsymbol{B}_c^T \boldsymbol{D}\boldsymbol{B}_e \, \mathrm{d}\Omega. \tag{2.12}$$

Substituting the displacement jump, as shown in Equation (2.6), into the constitutive equation of the cohesive zone in Equation (2.11b), results in

$$\dot{\boldsymbol{t}}^c = \boldsymbol{T}\boldsymbol{N}^{\text{int}} \left(\dot{u}^+ - \dot{u}^-\right). \tag{2.13}$$

The traction is then transformed to the global coordinate system by

$$\dot{\boldsymbol{t}}^c = \boldsymbol{Q}\boldsymbol{T}\boldsymbol{Q}^T\boldsymbol{N}^{\text{int}} \left(\dot{u}^+ - \dot{u}^-\right) \tag{2.14}$$

where the tangent matrix $\boldsymbol{T}$ is transformed using the orthogonal transformation matrix as

$$\boldsymbol{Q} = \begin{bmatrix} \boldsymbol{n} & \boldsymbol{s} & \boldsymbol{t} \end{bmatrix}. \tag{2.15}$$

The linearization of the cohesive force, as is shown in Equation (2.10), is done by determining the differentiation of the cohesive force of the upper and lower bound of the interface element, resulting in

$$\begin{bmatrix} \frac{\partial \boldsymbol{f}_{ie,+}^{\text{coh}}}{\partial \boldsymbol{u}} \\ \frac{\partial \boldsymbol{f}_{ie,-}^{\text{coh}}}{\partial \boldsymbol{u}} \end{bmatrix} = \begin{bmatrix} \frac{\partial \boldsymbol{f}_{ie,+}^{\text{coh}}}{\partial \boldsymbol{u}^+} & \frac{\partial \boldsymbol{f}_{ie,+}^{\text{coh}}}{\partial \boldsymbol{u}^-} \\ \frac{\partial \boldsymbol{f}_{ie,-}^{\text{coh}}}{\partial \boldsymbol{u}^+} & \frac{\partial \boldsymbol{f}_{ie,-}^{\text{coh}}}{\partial \boldsymbol{u}^-} \end{bmatrix} \begin{bmatrix} \delta \boldsymbol{u}^+ \\ \delta \boldsymbol{u}^- \end{bmatrix}. \tag{2.16}$$

From this the cohesive element tangent stiffness matrix can derived as

$$\boldsymbol{K}_{ie}^{\text{coh}} = \begin{bmatrix} \int_{\Gamma_d} \boldsymbol{N}^T\boldsymbol{Q}\boldsymbol{T}\boldsymbol{Q}^T\boldsymbol{N} \, \mathrm{d}\Gamma_d & -\int_{\Gamma_d} \boldsymbol{N}^T\boldsymbol{Q}\boldsymbol{T}\boldsymbol{Q}^T\boldsymbol{N} \, \mathrm{d}\Gamma_d \\ -\int_{\Gamma_d} \boldsymbol{N}^T\boldsymbol{Q}\boldsymbol{T}\boldsymbol{Q}^T\boldsymbol{N} \, \mathrm{d}\Gamma_d & \int_{\Gamma_d} \boldsymbol{N}^T\boldsymbol{Q}\boldsymbol{T}\boldsymbol{Q}^T\boldsymbol{N} \, \mathrm{d}\Gamma_d \end{bmatrix} \tag{2.17}$$

Difference Intrinsic and Extrinsic numerical methods

The application of the intrinsic and extrinsic TSL is different due to different initial traction value, as has been explained previously.

The intrinsic method has the cohesive elements inserted into the model before the simulation. The TSL is always activated in the cohesive elements. The initial elastic slope of this TSL creates an artificial compliance [67]. This artificial compliance can be a large issue when the cohesive elements are implemented on the whole domain. The artificial compliance results in a difference in the elastic stress waves in the continuum [38]. A solution for this is to increase the initial elastic slope of the TSL, although this decreases the stability of the model. The implementation of the cohesive element over the complete domain also results in the fact that there is a large increase in Degree of Freedom (DOF), and thus computational time.

With the extrinsic method, only the softening part of the TSL is present. This ensures that no artificial compliance is present in the model [67]. Using the extrinsic method, the cohesive law is added to the mesh when the maximum traction is reached. This decreases the DOF of the model, but does require an additional criterion for the elements [38]. Another disadvantage of the extrinsic models is that there is no possibility of parallelization anymore, resulting in a computationally expensive model.

Mesh Dependency

Often, the cohesive elements are used when the crack path is known a priori, for example when investigating interface debonding or delamination problems. When the crack path is unknown, the cohesive elements can be embedded over the whole domain [3]. This results in the mesh dependency of the crack path and artificial compliance. The cohesive interface elements enable the damage propagation only on the interface of the continuum elements. As a result the fracture energy is larger than that of a straight crack when the interface is not aligned with the crack path [48].

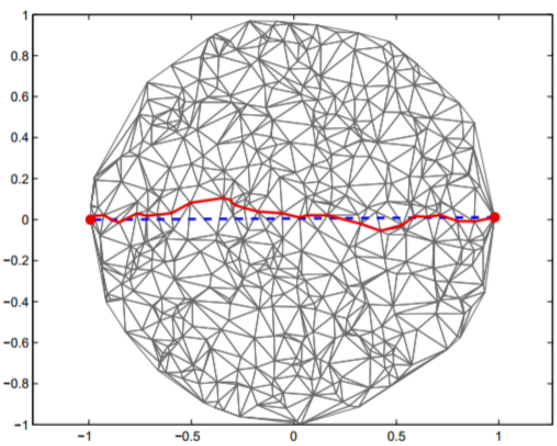

Figure 2.14: Shortest path from left to right with a random mesh [48]

The influence of the mesh on the crack length is shown in Figure 2.14. The difference between the shortest distance from two points is compared to the shortest distance over the mesh boundary. The increase in length of the crack results in that more energy is required. The error between the direct route and over the mesh boundary is defined as

$$\epsilon = \frac{L_g}{L_e} - 1 \tag{2.18}$$

where ϵ is the error, L_g is the length over the mesh (as shown as the red line in Figure 2.14), and L_e is the blue line in Figure 2.14 and is the shortest path. Rimoli and Rojas [48] found a correlation between the fracture process and the crack path length. If the mesh causes the crack to be unable to follow the physically correct path, more energy dissipation is required compared to a continuum crack. This is called mesh-induced toughness [48].

Another effect observer by Rimoli and Rojas [48], is the meshed-induced anisotropy. This occurs when looking at, for example, a structured meshed. If the mesh is aligned with the crack, a lower energy dissipation is observed, but when the crack is in between the orientation of the mesh, the error is maximized.

Several meshing techniques have been researched to determine the mesh dependance of these meshes [48, 34]. Here, it is found that isotropic behavior was found for unstructured meshes, and high anisotropy is found for structures (4K) meshes. For the meshing technique named conjugate directions mesh [48], the anisotropy is completely removed and the mesh-induced toughness is halved compared to an unstructured mesh. However, the quality of the elements decreases significantly.

2.3 Multiscale Analysis

Multiscale analysis is a popular field at the moment, due to the increase of computational power and with it the increase of the possibilities when using the multiscale analysis. In this section first the multiscale concept is discussed. Afterwards, an example of computational homogenization of fracture is shown. Finally, the Representative Volume Element (RVE) and periodicity of the volume element will be discussed.

2.3.1 Multiscale concept

The macroscopic response of a material is often heavily reliant on the microscopic structure, where for instance the size, distribution and properties of the different constituents on the microscale have a significant influence. Also the boundary conditions on the macroscale can have an influence on the microscopic response, such as microscopic cracking [40].

There are different methods to couple the different scales. These multiscale methods are for instance the concurrent, semi-concurrent or hierarchical method. The concurrent methods apply the microscale directly to the larger scale and the computation is done simultaneously. For the hierarchical method the two scales are simulated separately. Below the hierarchical methods are researched further, since for this research it is required that the two scales are separate.

The hierarchical methods require a homogenization of the fine scale to use on the coarse scale. Homogenization methods determine the average behavior of the fine scale and couple it to

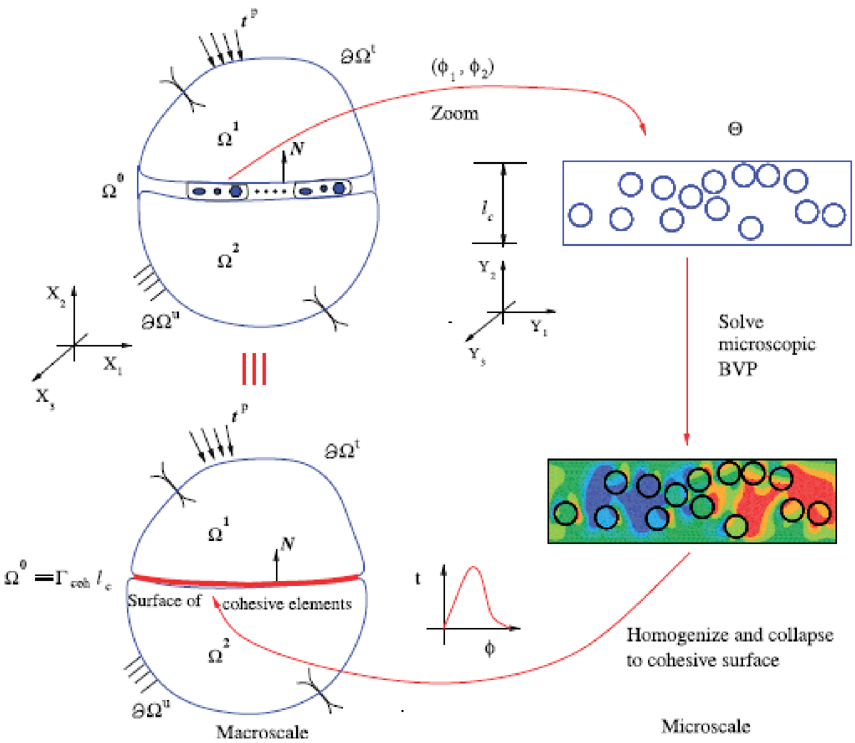

Figure 2.15: The Schematic representation of the cohesive zone computational homogenization technique [33]

a larger scale. Homogenization was first used with the Rule of Mixtures (RoM), developed by Voigt [63], Reuss [47], where the multiphase properties were averaged. Homogenization can be categorized into numerical and computational homogenization techniques. Numerical homogenization uses the unit cell for the numerical solution. A disadvantage is that the unit cell requires a lot of assumptions on the constitutive behavior of the macroscale, resulting it to be less suitable for non-linear problems. The computational homogenization looks to overcome these issues by describing the macroscopic constitutive behavior, using FEM and a Microstructural Volume Element (MVE) [61]. The macroscopic constitutive relations are characterized during the simulation [40]. This is further elaborated in the next section.

2.3.2 Computational Homogenization of fracture

Many different homogenization techniques have been developed. An example of the computational homogenization with microscale fracture is discussed below. In this research a 2D macroscale solid body that has a given displacement field, as is shown in Figure 2.16, is investigated. The quasi-static equilibrium of the body, which is denoted by Ω^{M}, can be written as [61]

$$
\begin{aligned}
\operatorname{div}(\boldsymbol{\sigma}^M) &= \boldsymbol{b}^M \qquad \boldsymbol{x}^M \in \Omega^M && (2.19a)\\
\boldsymbol{\sigma}^{\mathrm{M}} \cdot \boldsymbol{n}^{\mathrm{M}} &= \boldsymbol{t}^M(\tilde{\boldsymbol{u}}^{\mathrm{M}}) \qquad \boldsymbol{x}^{\mathrm{M}} \in \Gamma_d^{\mathrm{M}} && (2.19b)\\
\boldsymbol{\sigma}^{\mathrm{M}} \cdot \boldsymbol{n}^{\mathrm{M}} &= \bar{\boldsymbol{t}}^M \qquad \boldsymbol{x}^{\mathrm{M}} \in \Gamma_{\bar{t}}^{\mathrm{M}} && (2.19c)\\
\boldsymbol{u}^M &= \bar{\boldsymbol{u}}^{\mathrm{M}} \qquad \boldsymbol{x}^{\mathrm{M}} \in \Gamma_{\bar{u}}^{\mathrm{M}} && (2.19d)
\end{aligned}
$$

where the cohesive crack is on Γ_d^{M}, the applied traction on $\Gamma_{\bar{t}}^{\mathrm{M}}$ and the boundary conditions on $\Gamma_{\bar{u}}^{\mathrm{M}}$. The superscript M is to indicate that the variable is on the macroscale. For the microscale the superscript m is used.

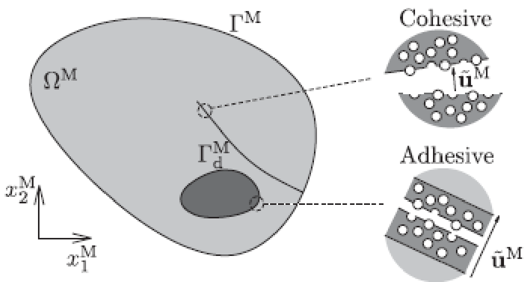

Figure 2.16: The schematic representation of the macroscopic model. The boundary $\Gamma_{\mathrm{d}}^{\mathrm{M}}$ is the cohesive crack [61]

From this macroscopic body, the microscopic RVE is derived. This RVE needs to be consistend with the macroscale in terms of failure models. The RVE and its definition are further discussed in Section 2.3.3. The quasi-static equilibrium for the microscale model can be described by

$$
\begin{aligned}
\operatorname{div}(\boldsymbol{\sigma}^m) &= \boldsymbol{b}^m \qquad \boldsymbol{x}^m \in \Omega^m && (2.20a)\\
\boldsymbol{\sigma}^m \cdot \boldsymbol{n}^m &= \boldsymbol{t}^m(\tilde{\boldsymbol{u}}^m) \qquad \boldsymbol{x}^m \in \Gamma_d^m && (2.20b)\\
\boldsymbol{u}^m &= \bar{\boldsymbol{u}}^m \qquad \boldsymbol{x}^m \in \Gamma_{\bar{u}}^m && (2.20c)
\end{aligned}
$$

.

The similarity to the macroscale equilibrium equation in Equation (2.19) can be seen. The difference, however, is mainly in the Cauchy stress and microscale traction, as these are described using analytical derived quantities. The equations of the traction are missing due to the fact that the boundary conditions on the RVE are solely displacement driven boundary conditions (including periodic boundary conditions).

The schematic representation of the RVE that is used for the homogenization, can be found in Figure 2.17. Here, only one cohesive crack is shown, although multiple cohesive cracks are possible. The homogenized engineering strain $\langle\varepsilon^{\mathrm{m}}\rangle_{\Omega^{\mathrm{m}}}$ can be found in Equation (2.21), which

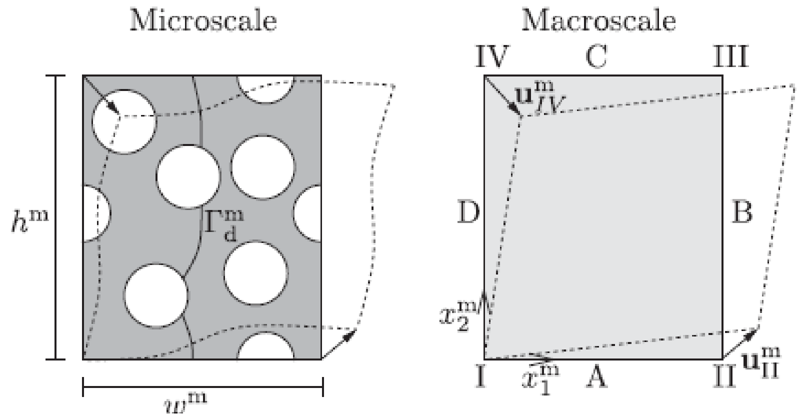

Figure 2.17: The schematic of the homogenization of the bulk properties [61]

is defined as a function of the nodal displacement of the corner nodes due to the periodic boundary conditions resulting in that the integral over the boundary is zero. In order to rewrite the volume integral to a boundary integral, the divergence theorem is used. The engineering strain is defined by

$$\langle \boldsymbol{\epsilon}^{\mathrm{m}} \rangle_{\Omega^{\mathrm{m}}} = \frac{1}{w^{\mathrm{m}} h^{\mathrm{m}}} \int_{\Omega^{\mathrm{m}}} \boldsymbol{\epsilon}^{\mathrm{m}} \,\mathrm{d}\Omega^{\mathrm{m}} = \frac{1}{w^{\mathrm{m}}} \boldsymbol{a}_{\mathrm{II}}^{\mathrm{m}} \otimes^{s} \boldsymbol{n}^{\mathrm{M}} + \frac{1}{h^{\mathrm{m}}} \boldsymbol{a}_{\mathrm{IV}}^{\mathrm{m}} \otimes^{s} \boldsymbol{s}^{\mathrm{M}} \tag{2.21}$$

where $\boldsymbol{a}_{\mathrm{II}}^{\mathrm{m}}$ and $\boldsymbol{a}_{\mathrm{IV}}^{\mathrm{m}}$ are the displacements at the node points II and IV, as is shown in Figure 2.17. Using the Hill-Mandel energy condition [27], the homogenized stress is as shown in Equation (2.22). This is found using the divergence theorem to rewrite the volume integral to a boundary integral. Additionally, the anti-periodicity of the traction of the periodic boundary conditions for the displacements is used. Resulting in the homogenized stress as

$$\langle \boldsymbol{\sigma}^{\mathrm{m}} \rangle_{\Omega^{\mathrm{m}}} = \frac{1}{w^{\mathrm{m}} h^{\mathrm{m}}} \int_{\Omega^{\mathrm{m}}} \boldsymbol{\sigma}^{\mathrm{m}} \,\mathrm{d}\Omega^{\mathrm{m}} = \frac{1}{w^{\mathrm{m}}} \boldsymbol{f}_{B}^{\mathrm{m}} \otimes \boldsymbol{n}^{\mathrm{M}} + \frac{1}{h^{\mathrm{m}}} \boldsymbol{f}_{C}^{\mathrm{m}} \otimes \boldsymbol{s}^{\mathrm{M}}. \tag{2.22}$$

Using the homogenization scheme, as shown in Figure 2.18, the macroscopic TSL can be derived. The effective traction can then be defined as

$$\boldsymbol{t}^{\mathrm{M}} = \boldsymbol{\sigma}^{\mathrm{M}} \cdot \boldsymbol{n}^{\mathrm{M}} = \frac{1}{h^{\mathrm{m}}} \boldsymbol{f}_{\mathrm{B}}^{\mathrm{m}}. \tag{2.23}$$

The macroscopic crack opening is related to the overall displacement of the nodes of the RVE, and can be related to the microscale displacement using

$$\tilde{\boldsymbol{u}}^{\mathrm{M}} = \boldsymbol{u}_{\mathrm{II}}^{\mathrm{m}} = \boldsymbol{a}_{\mathrm{II}}^{\mathrm{m}}. \tag{2.24}$$

Turteltaub et al. [53] has proposed a new multiscale method for the fracture process. This method is used in this research and is further elaborated in Chapter 3.

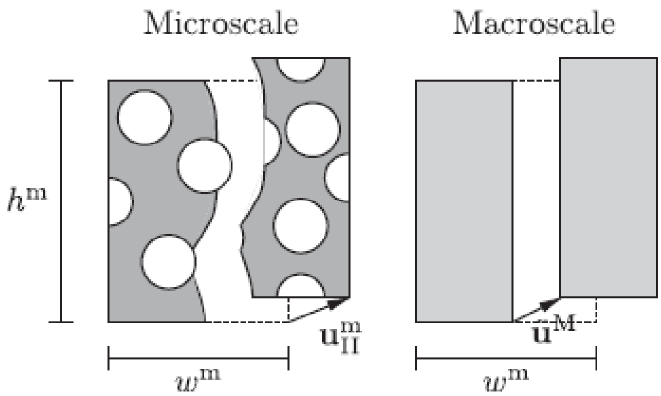

Figure 2.18: The schematic representation of the homogenization of the cohesive fracture [61]

2.3.3 Representative Volume Element

In the academic world the RVE has a lot of different definitions. The most important thing to realize, is that the definition of the RVE is a function of the subject that is being investigated. The overlap of the definitions, as presented in Gitman et al. [23], is apparent, and are summarized below.

- The RVE should contain sufficient inclusions to be statistically representative of the macroscopic response [25, 27]
- The RVE should be large enough to be able to have all the deformation processes, and this remains the same when increasing the volume [52, 19].
- The RVE should be sufficiently smaller than the macroscopic body, also known as the principle of separation of scales [25, 42].

The RVE is thus a relatively small sample of the macroscopic bulk material, which contains sufficient information to be statistically representative. A method to determine the RVE size is to make multiple models with different sizes of the volume element to do a convergence study on the required outputs for the given study. Other methods look at, for instance, the allowed scatter of the results [62].

2.3.4 Periodicity

For the RVE it is required that the boundaries should emulate the surrounding material (although the material is not there), and reduce the effect of the non-physical edges of the RVE [11]. Some commonly used boundary conditions for this are presented in Table 2.3.

In this research the effective stiffness has been compared. The periodic boundary conditions show to have the best estimation for the effective stiffness, which is the case for both periodic

Table 2.3: Often used boundary conditions for the RVE [10]

BC type	Effective stiffness	Localization band
Taylor	strong overestimation	Fully suppressed
Linear	overestimation	Constrained on the boundaries
Periodic	good estimation	Respecting periodicity
Minimal (traction)	underestimation	Sensitive to spurious localization

and random microstructures [10, 37]. This type of boundary condition is often used [31, 32, 33, 61, 3, 40, 10, 9] and is visualized in Figure 2.19. The periodic boundary condition results in that the displacement on the boundary of the RVE equals that on the opposite side of the RVE.

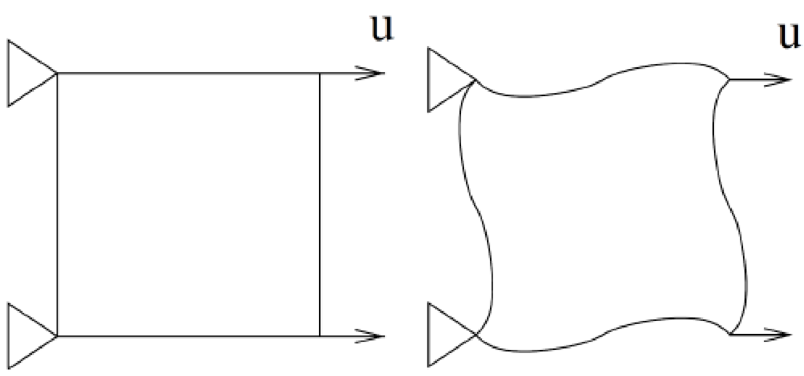

(a) Undeformed (b) Deformed

Figure 2.19: Periodic boundary conditions, where the displacement of on side is equal to the displacement on the opposite side [23]

Next to the periodic boundary conditions, the material can also be periodic. This periodicity is called the no-wall effect and enables inclusions to penetrate the wall and reappear on the other side of the RVE. An example of this is shown in Figure 2.20. It ensures that the RVE is part of a larger structure.

Using both the no-wall effect and the periodic boundary conditions, it is simulated that the volume element is part of a larger structure, as is shown in Figure 2.21.

2.4 Concluding remarks

In this chapter three things have been discussed: voids in a Fiber Reinforced Plastic (FRP), the CZM and multiscale analysis. From the investigation on the microscopic voids, two type of microvoids were found: matrix voids and interfiber voids. The interfiber voids are caused by the inability of resin to flow between multiple fibers, resulting in a void. For the matrix voids it was found that, due to the manufacturing methods, in transverse direction the matrix microvoids have a low aspect ratio.

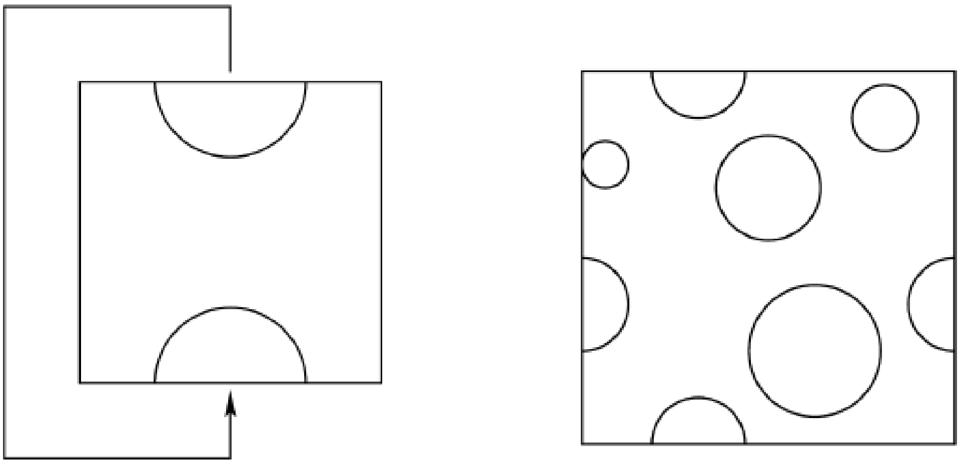

(a) The reappearing of the inclusions (b) Example of the material periodicity

Figure 2.20: Using the no-wall effect using the material periodicity [23]

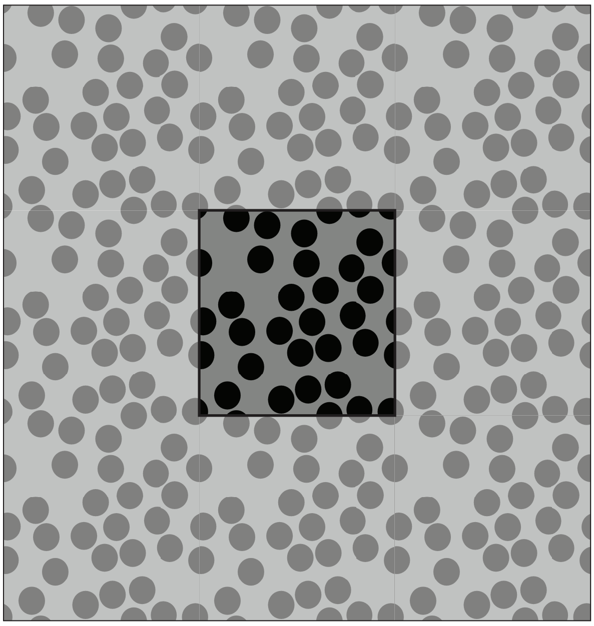

Figure 2.21: The volume element (dark) being part of a larger surrounding structure, where the fibers align due to the no-wall effect

To model the fracture mechanics of an FRP the CZM is very promising. The CZM can describe both the damage initiation and propagation using a TSL. The implementation in FEM can be done using cohesive elements. These cohesive elements are zero-thickness interface elements. If the crack path is known a priori, these can be placed along the crack path. If the crack path is not known before the simulation, the cohesive elements can be placed throughout the domain, although this does cause some issues such as mesh dependency and artificial compliance. Where the mesh dependancy is due to the crack only being able to propagate over the interface of the continuum elements and the artificial compliance is created due to the initial stiffening of the cohesive elements cause by the extrinsic TSL.

Using multiscale modeling to determine the effective properties of a fiber reinforced composite has been proposed. For this the computational homogenization technique is used to determine the macroscopic TSL using the microscopic simulations. To perform this homogenization an RVE is used that contains periodic boundary conditions and for the fibers a no-wall effect is used.

Chapter 3

Methodology

The objective of this thesis is to determine the effect of sub-ply voids of a fiber-reinforced composite, using a multiscale analysis. A multiscale method was developed by Turteltaub et al. [53] to determine the macroscopic Traction-Separation Law (TSL) using a Hill-Mandel homogenization scheme and a Representative Volume Element (RVE) on the microscale.

In this chapter, first the general idea of this theory is discussed in Section 3.1. The geometry of the Microstructural Volume Element (MVE) is discussed in Section 3.2. In Section 3.3 the microscale formulation is discussed. The Scale transition relations is discussed in Section 3.4. Finally, some concluding remarks are made in Section 3.5.

3.1 General idea

As an output of this study the effect of sub-ply voids on the Effective Traction Separation Law (ETSL) is determined. This ETSL that can be used in a macroscopic Cohesive Zone Model (CZM). This is done for arbitrary loading conditions. For the microscale the Fiber Reinforced Plastic (FRP) is assumed to contain defects such as porosities (microvoids) and interfiber voids. The method as proposed by Turteltaub et al. [53] is a numerical discontinuous homogenization method. This means that the microscale simulations and macroscale are done separately. The fracture mechanics of a microstructural RVE are used to determine the TSL on the macroscale. With a predefined macroscopic strain-loading, the microscopic RVE is used to determine the macroscopic TSL and crack properties using a special averaging procedure. From this, a parametric study can be done to see the effect on for instance material properties and different strain-loading conditions.

3.2 Geometry of the Microstructural Volume Element

The definition of an RVE has already been discussed in Section 2.3.3. In this study the RVE is considered representative if the ETSL has converged. This study focuses on a uni-directional

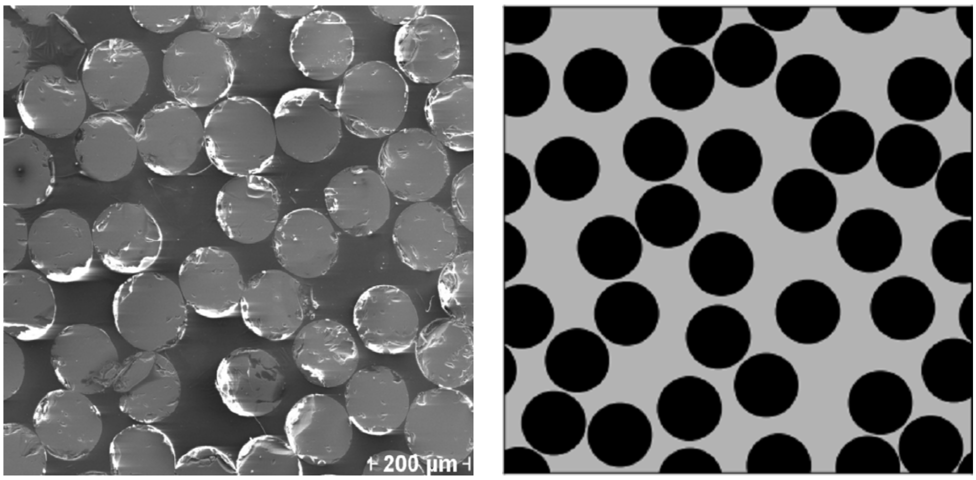

(a) Glass fiber reinforced composite [6] **(b)** The MVE geometry without defects

Figure 3.1: Comparison between the micro structure of a composite (SEM image) and its volume element

fiber reinforced composite that contains sub-ply microscopic defects. The defects considered in this thesis are matrix voids and interfiber gaps caused by closely packed fiber that result in the matrix being unable flow between the fibers. A 2-Dimensional (2D) volume element is used, although the theory can be extended to be able to use 3-Dimensional (3D) models.

From Scanning Electron Microscope (SEM) experiments, a microstructure, as shown in Figure 3.1a, can be found. For the MVE a similar geometry is thus required, as shown in Figure 3.1b.

3.3 Microscale formulation

The microstructural volume element is shown in Figure 3.2. This shows a random geometry with an arbitrary crack. The nomenclature showed in this figure is used throughout the study. The size of the MVE is defined as $l_1 \times l_2$ and is defined as the volume/domain Ω. The boundaries of this volume is $\partial\Omega$, which is defined for each edge with $\partial\Omega_i$, $i = 1, 2, 3, 4$. The boundary also contains an outwards unit vector $\boldsymbol{n}_i$, $i = 1, 2, 3, 4$. The crack is denoted as Γ. The crack can be a combination of multiple different crack segments, which could contain crack bifurcations. The vector $\boldsymbol{m}$ is the normal vector of the crack. By convention, $\boldsymbol{m} = \boldsymbol{m}^-$ and is pointing to the Γ^+ side, $\boldsymbol{m}^+ = -\boldsymbol{m}^-$ which is pointed towards the Γ^- side. This sign convention is chosen arbitrarily, but is used consistently throughout the theory. For the voids present in the MVE, the $\boldsymbol{u}^v$ is the displacement on a location on the boundary and $\boldsymbol{m}^v$ is the normal vector from the void boundary pointing inwards.

A detailed derivation of the boundary value problem for the MVE can be found in Turteltaub et al. [53]. The crack growth is assumed to be a quasi-static process. Thus the MVE always fulfills the equilibrium conditions. With the absence of body forces, this results in the equilibrium equation, as shown in Equation (3.1a). The continuity of the crack surface is denoted, as shown in Equation (3.1b). Equation (3.1c) and Equation (3.1d) show the periodic boundary conditions of the boundaries when no crack is going through the boundary. Since the crack is allowed to move through the external boundary of the domain, Equation (3.1e) and Equation (3.1f) are used to ensure that if the crack moves through the boundary, the Periodic Boundary Conditions (PBC) on opposite sides of the crack are still ensured. The full microscale boundary-value problem is as follows:

$$
\begin{aligned}
&\operatorname{div} \boldsymbol{\sigma}(\boldsymbol{x}, t) = \mathbf{0} && \boldsymbol{x} \text{ in } \Omega \setminus \Gamma && (3.1a)\\
&\boldsymbol{t}^{+}(\boldsymbol{x}^{+}, t) = -\boldsymbol{t}^{-}(\boldsymbol{x}^{-}, t) && \boldsymbol{x} \text{ on } \Gamma && (3.1b)\\
&\begin{aligned}\boldsymbol{u}(\boldsymbol{x} + l_1\boldsymbol{e}_1, t) - \boldsymbol{u}(\boldsymbol{x}, t) &= l_1\bar{\boldsymbol{\epsilon}}(t)\boldsymbol{e}_1\\ \boldsymbol{t}(\boldsymbol{x} + l_1\boldsymbol{e}_1, t) &= -\boldsymbol{t}(\boldsymbol{x}, t)\end{aligned} && \boldsymbol{x} \text{ on } \partial\Omega_3 \setminus \Gamma && (3.1c)\\
&\begin{aligned}\boldsymbol{u}(\boldsymbol{x} + l_2\boldsymbol{e}_2, t) - \boldsymbol{u}(\boldsymbol{x}, t) &= l_2\bar{\boldsymbol{\epsilon}}(t)\boldsymbol{e}_2\\ \boldsymbol{t}(\boldsymbol{x} + l_2\boldsymbol{e}_2, t) &= -\boldsymbol{t}(\boldsymbol{x}, t)\end{aligned} && \boldsymbol{x} \text{ on } \partial\Omega_4 \setminus \Gamma && (3.1d)\\
&\begin{aligned}\boldsymbol{u}^{\pm}(\boldsymbol{x}^{\pm} + l_1\boldsymbol{e}_1, t) - \boldsymbol{u}^{\pm}(\boldsymbol{x}^{\pm}, t) &= l_1\bar{\boldsymbol{\epsilon}}(t)\boldsymbol{e_1}\\ \boldsymbol{t}^{\pm}(\boldsymbol{x}^{\pm} + l_1\boldsymbol{e}_1, t) &= -\boldsymbol{t}^{\pm}(\boldsymbol{x}^{\pm}, t)\end{aligned} && \boldsymbol{x} \text{ on } \partial\Omega_3 \cap \Gamma && (3.1e)\\
&\begin{aligned}\boldsymbol{u}^{\pm}(\boldsymbol{x}^{\pm} + l_2\boldsymbol{e}_2, t) - \boldsymbol{u}^{\pm}(\boldsymbol{x}^{\pm}, t) &= l_2\bar{\boldsymbol{\epsilon}}(t)\boldsymbol{e_2}\\ \boldsymbol{t}^{\pm}(\boldsymbol{x}^{\pm} + l_2\boldsymbol{e}_2, t) &= -\boldsymbol{t}^{\pm}(\boldsymbol{x}^{\pm}, t)\end{aligned} && \boldsymbol{x} \text{ on } \partial\Omega_4 \cap \Gamma && (3.1f)
\end{aligned}
$$

where $\boldsymbol{u}$ is the displacement vector and $\bar{\epsilon}$ is the macroscopic strain tensor. This strain tensor is dependent on time, as the applied macroscopic strain is increased over time. In most of the equations throughout this chapter the time variable is suppressed for simplicity. $\boldsymbol{t}$ is the traction vector acting on a given surface, which can be either the external boundary or the crack. $\Omega\backslash\Gamma$ stands for the bulk without a crack, $\partial\Omega\backslash\Gamma$ is the external boundary without a crack and $\partial\Omega \cap \Gamma$ is location where the crack crosses the external boundary. The crossing of the crack through the boundary, resulting in a periodic crack and the implications of this are discussed in further detail in Section 3.4.3. For all random points that are not part of the crack surface, the displacement and the strain field ϵ are related as

$$\epsilon = \frac{1}{2}\left(\nabla \boldsymbol{u} + \nabla \boldsymbol{u}^T\right). \tag{3.2}$$

3.3.1 Constitutive relations

For the composite material, the constitutive relations and fracture behavior have to be defined. The composite consists of a linear elastic phase and brittle solid phase. At all locations, except the crack, the composite constitutive relation is given by

$$\boldsymbol{\sigma} = \mathbb{C}\boldsymbol{\epsilon} \qquad \text{in } \Omega \setminus \Gamma \tag{3.3}$$

where $\mathbb{C}$ is the stiffness tensor at a given point in the domain. This could be either a matrix element or fiber element. For the modeling of the fracture behavior, and thus the crack surface, the constitutive response is taken as

$$\boldsymbol{t} = \boldsymbol{f}_{coh}\left([\![\boldsymbol{u}]\!], \boldsymbol{\kappa}, \boldsymbol{m}\right) \qquad \boldsymbol{x} \text{ in } \Gamma \tag{3.4}$$

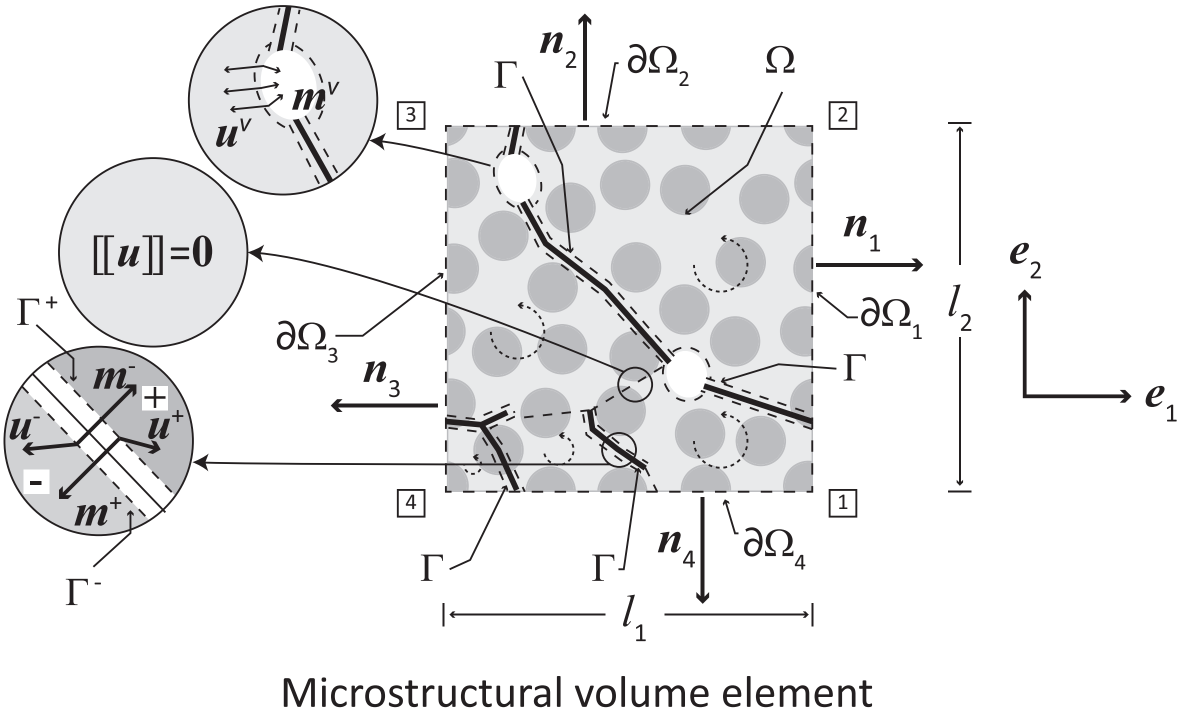

Figure 3.2: The microstructural volume element and its nomenclature, here the domain Ω is decomposed into multiple subdomains with the boundaries as indicated by the dashed lines. The boundary of the subdomains are either the external boundary, the crack surface Γ, the boundary of the voids or uncracked parts.

where the traction is defined using a microscale cohesive relation, f_{coh}, which in this case is a cohesive relation that describes the fracture at a given point $\boldsymbol{x}$. The cohesive relation is a function of the local cohesive opening $[\![\boldsymbol{u}]\!]$, the crack normal $\boldsymbol{m}$ and internal variables κ. The crack opening is defined as the relative opening between the two sides of the crack, which is shown in Figure 3.2, as

$$[\![\boldsymbol{u}]\!] = \boldsymbol{u}^+ - \boldsymbol{u}^- \qquad \boldsymbol{x} \text{ in } \Gamma. \tag{3.5}$$

This crack opening relationship can also be related on the external boundary of the domain, using both Equation (3.5) and Equation (3.1e)-Equation (3.1f). This results in the relation as

$$[\![\boldsymbol{u}(\boldsymbol{x},t)]\!] = [\![\boldsymbol{u}(\boldsymbol{x}+l_1\boldsymbol{e}_1,t)]\!] \qquad \boldsymbol{x} \text{ on } \partial\Omega_3 \cap \Gamma \tag{3.6a}$$
$$[\![\boldsymbol{u}(\boldsymbol{x},t)]\!] = [\![\boldsymbol{u}(\boldsymbol{x}+l_2\boldsymbol{e}_2,t)]\!] \qquad \boldsymbol{x} \text{ on } \partial\Omega_4 \cap \Gamma. \tag{3.6b}$$

3.4 Scale transition relations

The Hill-mandel condition is a scale transition requirement between the micro and macroscale that uses the energy relations. The macroscale behavior can be extracted using the microscopic information on the domain. The extraction of the ETSL is done with a separation between the bulk material ($\Omega \setminus \Gamma$) and actual microscopic crack (Γ).

3.4.1 Bulk and fracture strains

The domain (Ω) can be divided into the subdomains as seen in Figure 3.2 with the dashed lines. This division is done to enable the use of the divergence theorem and a well-defined strain field. Using the divergence theorem on each subdomain results in the microscopic strain tensor as found in Equation (3.7). For the voids the sum of the integrals of the individual parts of the void boundary is the same as the integral over the complete void boundary. A summation of these integrals per void give the additional term to the strain tensor. No distinction is made between voids that are part of the main crack (Γ) and voids that are not part of the crack. This assumption is similar to the assumption made by Turteltaub et al. [53] which assumes that all individual cracks in the MVE have a contribution to the main crack. The microscopic strain tensor can now be expressed as

$$\langle \boldsymbol{\epsilon} \rangle_\Omega := \frac{1}{|\Omega|} \int_{\partial\Omega} [\boldsymbol{u} \otimes \boldsymbol{n}]_{\mathrm{sym}} \, \mathrm{d}s - \frac{1}{|\Omega|} \int_{\Gamma} [[\![\boldsymbol{u}]\!] \otimes \boldsymbol{m}]_{\mathrm{sym}} \, \mathrm{d}s - \sum_{k=1}^{N_v} \frac{1}{|\Omega|} \int_{\partial v_k} [\boldsymbol{u} \otimes \boldsymbol{m}^{\mathrm{v}}]_{\mathrm{sym}} \, \mathrm{d}s \quad (3.7)$$

where $\otimes$ is the tensor product and the symmetric part of the tensor is $[\boldsymbol{X}]_{sym} := \frac{1}{2}(\boldsymbol{X} + \boldsymbol{X}^T)$, the normal vector $\boldsymbol{m}^v$ of the voids is pointed inwards from the boundary of the void. Using Equation 3.7, the relation between the applied strain ($\overline{\boldsymbol{\epsilon}}$) and the internal strain on the bulk, crack and voids is found in Equation 3.8, and ϵ^v is defined as found in Equation 3.9. ϵ^v is the summation of all the changes in size of the voids on the microscale. The applied strain is equal to the strain in the volume element as

$$\overline{\boldsymbol{\epsilon}} = \langle \boldsymbol{\epsilon} \rangle_\Omega + \boldsymbol{\epsilon}^{\mathrm{f}} + \boldsymbol{\epsilon}^{\mathrm{v}} \quad (3.8)$$

where

$$\boldsymbol{\epsilon}^{\mathrm{v}} = \sum_{k=1}^{N_v} \frac{1}{|\Omega|} \int_{\partial v_k} [\boldsymbol{u} \otimes \boldsymbol{m}^{\mathrm{v}}]_{\mathrm{sym}} \, \mathrm{d}s \quad (3.9)$$

and

$$\boldsymbol{\epsilon}^{\mathrm{f}} := \frac{1}{|\Omega|} \int_{\Gamma} [[\![\boldsymbol{u}]\!] \otimes \boldsymbol{m}]_{\mathrm{sym}} \, \mathrm{d}s. \quad (3.10)$$

The volume-averaged stress is defined as

$$\langle \boldsymbol{\sigma} \rangle_\Omega := \frac{1}{|\Omega|} \int_{\partial\Omega} \boldsymbol{t} \otimes \boldsymbol{x} \, \mathrm{d}s \quad (3.11)$$

where $\boldsymbol{t} = \boldsymbol{\sigma}\boldsymbol{n}$ on boundary of the domain ($\partial\Omega$). This can be rewritten as

$$\langle \boldsymbol{\sigma} \rangle_\Omega = \sum_{i=1}^{2} \bar{\boldsymbol{t}}_i \otimes \boldsymbol{e}_i \tag{3.12}$$

where

$$\bar{\boldsymbol{t}}_1 := \frac{1}{|\partial\Omega_1|} \int_{\partial\Omega_1} \boldsymbol{t}\,\mathrm{d}s \tag{3.13a}$$

$$\bar{\boldsymbol{t}}_2 := \frac{1}{|\partial\Omega_2|} \int_{\partial\Omega_2} \boldsymbol{t}\,\mathrm{d}s. \tag{3.13b}$$

The complete derivation can be found in Turteltaub et al. [53], where the derivation is based on the use of Equation (3.1e)-(3.1f).

3.4.2 Rate of work relations

For the Hill-Mandel conditions, the rate of work of the different parts are used. The specific rate of work done on the boundary can be found in Equation (3.14). The stress power in the material can be found in Equation (3.15). The rate of work done on the voids can be defined as the dot product of the traction and opening rate of the void boundary, as is shown in Equation (3.16). The three powers are defined as

$$P^{\mathrm{ext}} := \frac{1}{|\Omega|} \int_{\partial\Omega} \boldsymbol{t} \cdot \dot{\boldsymbol{u}}\,\mathrm{d}s \tag{3.14}$$

$$P^{\mathrm{b}} := \frac{1}{|\Omega|} \int_{\Omega} \boldsymbol{\sigma} \cdot \dot{\boldsymbol{\epsilon}}\,\mathrm{d}v \tag{3.15}$$

$$P^{\mathrm{v}} := \frac{1}{|\Omega|} \sum_{k=1}^{N_v} \int_{\partial v^k} \boldsymbol{t} \cdot \dot{\boldsymbol{u}}\,\mathrm{d}s. \tag{3.16}$$

Using the subdomains as shown in Figure 3.2, the relation between the rate of works follows as

$$P^{\mathrm{ext}} = P^{\mathrm{b}} + P^{\mathrm{f}} - P^{\mathrm{v}} \tag{3.17}$$

where

$$P^{\mathrm{f}} := \frac{1}{|\Omega|} \int_{\Gamma} \boldsymbol{t} \cdot [\![\dot{\boldsymbol{u}}]\!]\,\mathrm{d}s. \tag{3.18}$$

The rate of work of the fracture is shown in Equation (3.18). The rate of work on the voids is negative in Equation (3.17), which follows from the divergence theorem. Another way to determine the sign is by realizing the voids are similar to the external boundary, and should thus be positive on the left side of the equation, and thus it is a negative contribution to internal rate of work.

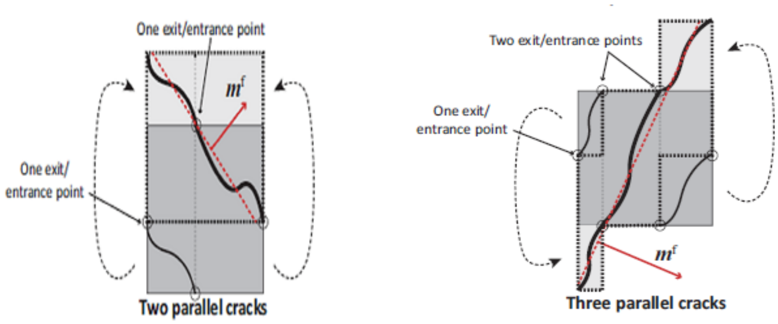

(a) Two parallel cracks

(b) Three parallel cracks

Figure 3.3: Examples of two type of parallel cracks that are made into one continuous crack

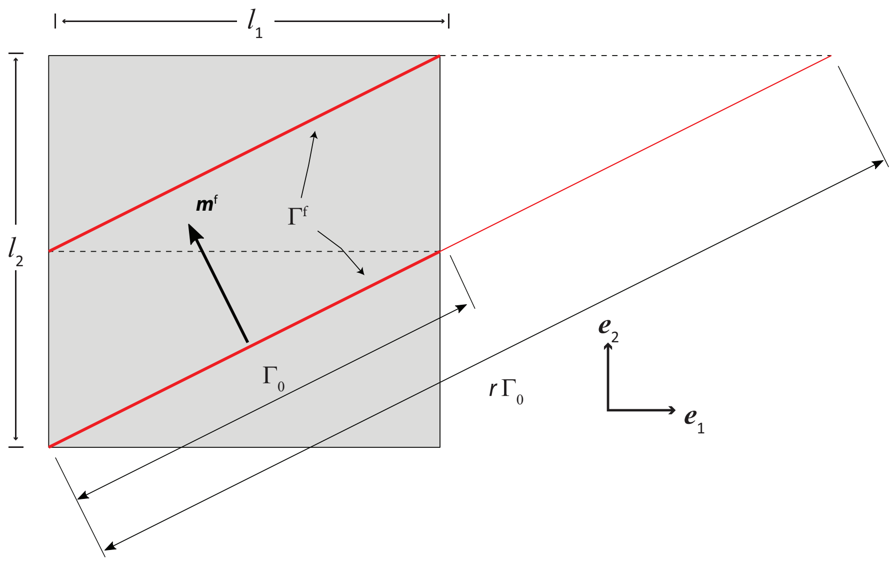

Figure 3.4: The macroscopic crack length. Here the value r is determined using a ratio between the maximum crack length and minimum crack length present in the MVE

3.4.3 Periodic crack

The boundary value problem, as discussed previously, enables the crack to propagate through the boundary of the MVE. Two examples of a possible periodic crack can be found in Figure 3.3 [53]. For simplicity, bifurcations are ignored. The dark gray areas are the original domain and the light gray areas are the parts of the initial domain that have been rearranged to form a single crack. The dark line is the crack, with the thinner lines indicating the parallel cracks to the main crack. Figure 3.3a shows an example which has two parallel cracks. In Figure 3.3b three parallel cracks can be seen. Due to the Boundary Value Problem (BVP), these parallel cracks are actually connected and can be interpreted as one crack, the main crack.

In order to determine the macroscopic crack length, a nominal length is used. The method used can be found in Figure 3.4. The equivalent crack length is estimated using the macroscopic crack normal and the possible amount of crossings through the domain Ω. The equation for the effective crack Γ^f can be found as

$$\left|\Gamma^{\mathrm{f}}\right| = \begin{cases} |\Gamma_0| & if r > r_{max} \\ r\,|\Gamma_0| & otherwise \end{cases} \tag{3.19}$$

where

$$|\Gamma_0| = \min\left(\frac{l_1}{|\boldsymbol{n}_2 \cdot \boldsymbol{m}^{\mathrm{f}}|}, \frac{l_2}{|\boldsymbol{n}_2 \cdot \boldsymbol{m}^{\mathrm{f}}|}\right) \tag{3.20}$$

and

$$r = \frac{\max\left(\frac{l_1}{|\boldsymbol{n}_2 \cdot \boldsymbol{m}^{\mathrm{f}}|}, \frac{l_2}{|\boldsymbol{n}_2 \cdot \boldsymbol{m}^{\mathrm{f}}|}\right)}{\Gamma_0}. \tag{3.21}$$

Using this method, only the effective crack normal and the size of the MVE are required to determine the effective crack length. The void properties are not required to determine the macroscopic crack length.

3.4.4 Hill-Mandel condition

The homogenization is schematically visualized in Figure 3.5. Here the microscale properties of the crack are homogenized using a Hill-Mandel condition. The effective crack normal is determined using a singular value decomposition as follows

$$\boldsymbol{m}^{\mathrm{f}} := \frac{\sum_{i=1}^{2} \mu_i \boldsymbol{m}_i}{\left\| \sum_{i=1}^{2} \mu_i \boldsymbol{m}_i \right\|} \tag{3.22}$$

where i are the unit vectors as shown in Figure 3.2. Now that both the effective crack normal and crack length are determined, the effective (macroscopic) crack opening can be determined as well. This is done using a rank-one approximation of the crack averaged tensor as

$$\left|\Gamma^{\mathrm{f}}\right| [\![\dot{\boldsymbol{u}}]\!]^{\mathrm{f}} = |\Gamma| \left\langle [\![\dot{\boldsymbol{u}}]\!] \right\rangle. \tag{3.23}$$

There is no contribution of the voids in this equation, which will be elaborated on later in this section.

The Hill-Mandel condition for the crack itself is required. From Equation (3.8) and Equation (3.17) the external power done on the volume element can be found in Equation (3.24). The internal power of the voids is the traction that acts on the boundary of the voids, as

$$\langle \boldsymbol{\sigma} \rangle_\Omega \cdot \bar{\dot{\boldsymbol{\epsilon}}} = \langle \boldsymbol{\sigma} \rangle_\Omega \cdot \langle \dot{\boldsymbol{\epsilon}} \rangle_\Omega + \langle \boldsymbol{\sigma} \rangle_\Omega \cdot \dot{\boldsymbol{\epsilon}}^{\mathrm{f}} + \langle \boldsymbol{\sigma} \rangle_\Omega \cdot \dot{\boldsymbol{\epsilon}}^{\mathrm{v}} = \frac{1}{|\Omega|} \int_\Omega \boldsymbol{\sigma} \cdot \dot{\boldsymbol{\epsilon}} \mathrm{d}v + \frac{1}{|\Omega|} \int_\Gamma \boldsymbol{t} \cdot [[\dot{\boldsymbol{u}}]] \mathrm{d}s - \frac{1}{|\Omega|} \sum_{k=1}^{N_v} \int_{\partial v^k} \boldsymbol{t} \cdot \dot{\boldsymbol{u}} \mathrm{d}s. \tag{3.24}$$

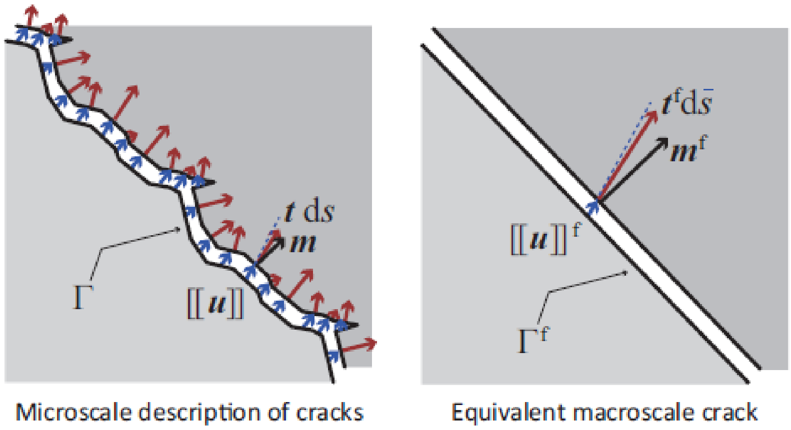

Figure 3.5: Homogenization of the crack using the Hill-Mandel condition.

From Equation (3.24), the Hill-Mandel condition on the crack can be determined as follows

$$\langle \boldsymbol{\sigma} \rangle_\Omega \cdot \dot{\boldsymbol{\epsilon}}^{\mathrm{f}} + \langle \boldsymbol{\sigma} \rangle_\Omega \cdot \dot{\boldsymbol{\epsilon}}^{\mathrm{v}} = \frac{1}{|\Omega|} \int_\Gamma \boldsymbol{t} \cdot [[\dot{\boldsymbol{u}}]] \mathrm{d}s - \frac{1}{|\Omega|} \sum_{k=1}^{N_v} \int_{\partial v^k} \boldsymbol{t} \cdot \dot{\boldsymbol{u}} \mathrm{d}s. \tag{3.25}$$

By making the equation independent on the size of the volume element, both sides of the equation are multiplied by $|\Omega| \, / \, |\Gamma|$, such that

$$\frac{1}{|\Gamma|} \int_\Gamma \langle \boldsymbol{\sigma} \rangle_\Omega \cdot [[\![\dot{\boldsymbol{u}}]\!] \otimes \boldsymbol{m}]_{\mathrm{sym}} \, \mathrm{d}s + \frac{1}{|\Gamma|} \int_{\partial v^k} \langle \boldsymbol{\sigma} \rangle_\Omega \cdot [\dot{\boldsymbol{u}}^v \otimes \boldsymbol{m}^{\mathrm{v}}] \mathrm{d}s = \frac{1}{|\Gamma|} \int_\Gamma \boldsymbol{\sigma} \cdot [[\![\dot{\boldsymbol{u}}]\!] \otimes \boldsymbol{m}]_{\mathrm{sym}} \, \mathrm{d}s - \frac{1}{|\Gamma|} \sum_{k=1}^{N_v} \int_{\partial v^k} \boldsymbol{t} \cdot \dot{\boldsymbol{u}} \mathrm{d}s. \tag{3.26}$$

When using the relation between the traction and stress ($\boldsymbol{t} = \boldsymbol{\sigma u}$) and the fact that $\langle x \rangle_\Gamma = \frac{1}{|\Gamma|} \int_\Gamma x \mathrm{d}s$, Equation 3.26 can be expressed such that

$$\left\langle (\langle \boldsymbol{\sigma} \rangle_\Omega - \boldsymbol{\sigma}) \cdot [[\![\dot{\boldsymbol{u}}]\!] \otimes \boldsymbol{m}]_{\mathrm{sym}} \right\rangle_\Gamma + \left(\frac{1}{|\Gamma|} \sum_{k=1}^{N_v} \int_{\partial v^k} \langle \boldsymbol{\sigma} \rangle_\Omega \cdot [\dot{\boldsymbol{u}}^{\mathrm{v}} \otimes \boldsymbol{m}^v] ds + \frac{1}{|\Gamma|} \sum_{k=1}^{N_v} \int_{\partial v^k} \boldsymbol{t} \cdot \dot{\boldsymbol{u}} \mathrm{d}s \right) = 0. \tag{3.27}$$

In the theory as presented by Turteltaub et al. [53], the Hill-mandel condition as presented above is the same although the part of the voids is not present, namely

$$\left| \Gamma^{\mathrm{f}} \right| \boldsymbol{t}^{\mathrm{f}} \cdot [[\dot{\boldsymbol{u}}]]^{\mathrm{f}} \approx |\Gamma| \, \langle \boldsymbol{t} \cdot [[\dot{\boldsymbol{u}}]] \rangle_\Gamma \tag{3.28}$$

$$\left| \Gamma^{\mathrm{f}} \right| \boldsymbol{t}^{\mathrm{f}} \cdot [[\dot{\boldsymbol{u}}]]^{\mathrm{f}} \approx |\Gamma| \, \langle \langle \sigma \rangle_\Omega \, \boldsymbol{m} \cdot [[\dot{\boldsymbol{u}}]] \rangle_\Gamma \, . \tag{3.29}$$

In the case with voids present, the void parameters are seen as another separate requirement, such that

$$\left(\frac{1}{|\Gamma|}\sum_{k=1}^{N_v}\int_{\partial v^k}\langle\boldsymbol{\sigma}\rangle_\Omega\cdot[\dot{\boldsymbol{u}}^{\mathrm{v}}\otimes\boldsymbol{m}^{\mathrm{v}}]ds+\frac{1}{|\Gamma|}\sum_{k=1}^{N_v}\int_{\partial v^k}\boldsymbol{t}\cdot\dot{\boldsymbol{u}}\mathrm{d}s\right)=0. \tag{3.30}$$

The reason for this separation is explained below. This results in the now three different requirements in Equation (3.28),(3.29) and (3.30). For this thesis it is assumed that the internal pressure of the voids is zero, so that the traction on the void boundary is zero, resulting in that the second term is zero. This implies that the first term of Equation 3.30 has to be equal to zero. From numerical simulations, as is also shown in the verification, it is found that this is approximately the case.

From the fact that the power of the voids is zero, as shown above, it can be assumed that the voids, even when they are part of the main crack, have no effect on the equivalent macroscopic crack. These can then be separated from the requirements as shown in Equation (3.28)-Equation (3.29). Since they have no effect on the equivalent macroscopic crack, it is found that the voids also have no effect on the macroscopic crack opening. From this, it can be concluded that there is also no contribution of the voids in the crack-average tensor, as shown in Equation (3.23).

Since the void contribution in Equation (3.27) is zero, the two separate Hill-Mandel requirements remain the same as in the theory as presented by Turteltaub et al. [53], and can be seen again in Equation (3.28) and Equation (3.29). Using these two requirements, a combination of the effective bulk-averaged traction and crack-averaged traction is used to equal the microscopic traction. From a rate of work view this is

$$\alpha P^{\mathrm{f}}_\Gamma+(1-\alpha)P^{\mathrm{f}}_\Omega\approx P^{\mathrm{f}} \tag{3.31}$$

where

$$P^{\mathrm{f}}_\Gamma=\frac{1}{\Omega}\left|\Gamma^{\mathrm{f}}\right|\boldsymbol{t}^{\mathrm{f}}_\Gamma\cdot[\![\dot{\boldsymbol{u}}]\!]^{\mathrm{f}} \tag{3.32a}$$

$$P^{\mathrm{f}}_\Omega=\frac{1}{\Omega}\left|\Gamma^{\mathrm{f}}\right|\boldsymbol{t}^{\mathrm{f}}_\Omega\cdot[\![\dot{\boldsymbol{u}}]\!]^{\mathrm{f}} \tag{3.32b}$$

$$P^{\mathrm{f}}=\frac{1}{\Omega}\int_\Gamma\boldsymbol{t}\cdot[\![\dot{\boldsymbol{u}}]\!]\,\mathrm{d}\Gamma. \tag{3.32c}$$

The tractions are defined as

$$\boldsymbol{t}^{\mathrm{f}}_\Gamma=\frac{|\Gamma|}{|\Gamma^{\mathrm{f}}|}\langle\boldsymbol{t}\otimes\boldsymbol{m}\rangle_\Gamma\,\boldsymbol{m}^{\mathrm{f}} \tag{3.33a}$$

$$\boldsymbol{t}^{\mathrm{f}}_\Omega=\langle\boldsymbol{\sigma}\rangle_\Omega\,\boldsymbol{m}^{\mathrm{f}} \tag{3.33b}$$

Using the alpha as determined in Equation (3.31), the effective traction can be then be determined using the relation between the crack averaged and bulk averaged traction as

$$\boldsymbol{t}^{\mathrm{f}}=\alpha\boldsymbol{t}^{\mathrm{f}}_\Gamma+(1-\alpha)\boldsymbol{t}^{\mathrm{f}}_\Omega. \tag{3.34}$$

3.5 Remarks

In this chapter the methodology of the numerical homogenization of the MVE has been presented. The theory as presented by Turteltaub et al. [53] was adapted to include voids on the microscale. The verification of this adaptation is discussed in Chapter 5. The method proposed, uses the Hill-Mandel condition to determine the ETSL of a material. This is done using both the bulk and crack averaged properties. The additional term that is added due to the voids, has the added advantages that this enables the possibility to add an internal pressure to the voids which can be caused during the manufacturing. In this study this was assumed to be negligible. In this chapter the theory for a 2D problem was presented, although with minor changes, this method can also be used for 3D cases.

The numerical implementation of this theory is presented in Chapter 4. Here some equations of the theory change due to an adaptation by Hirch [28] which solves an issue which is created by the use of the cohesive elements in the numerical application and ensures that for the effective crack normal no Singular Value Decomposition (SVD) is required. More on this is discussed in Section 4.2.

Chapter 4

Numerical Implementation

In this chapter the numerical implementation of the theory presented in Chapter 3 is implemented. First the pre-processing is discussed in Section 4.1. The Microstructural Volume Element (MVE) is created and implemented into `Abaqus`®. After this the post-processing is discussed in Section 4.2, at which the data extraction, processing and homogenization of the microscopic fracture process is performed, which has been simulated in `Abaqus`®.

4.1 Pre-Processing

The pre-processing can be divided into the model generation, which determines the geometry of the MVE, from which the mesh can be made. After this the boundary conditions can be applied to finally insert these properties in an `Abaqus`® input file.

4.1.1 Model generation

The `python` code to generate the model that is used in `Abaqus`® is split into multiple steps. These steps have been visualized in Figure 4.1. In this flow chart the four dashed lines stand for the different Python scripts. Each block of the model generation is discussed in detail in the next sections.

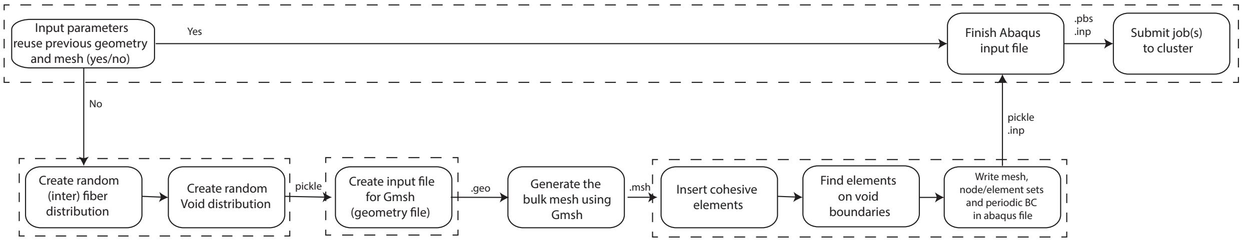

Figure 4.1: Flow chart of the preprocessing computational activities

Input parameters

Before the input parameters are determined, a previously generated geometry can be used and the mesh can be reused, but with different material properties or boundary conditions. This is used to model the same fiber and void distribution but with different loading cases such as constraint extension, biaxial extension-compression (which is the same as a pure shear loading case) and mixed loading of both the constraint extension and pure shear loading case.

The input parameters can be divided into several parts, which are the material properties of the fiber, matrix and interface between the fiber and matrix, but also the properties of the matrix voids and interfiber voids. In this study, the material properties are held constant while the void properties are changed. The material properties that are selected are of the fiber: HexTow® IM7 and matrix: CYCOM® 5230-2 [26, 14]. These properties can be found in Table 4.1. The elasticity modulus of the fiber is that of the transverse direction of the fiber, which is considerably lower than that of the fiber direction. For these two materials the fracture properties were selected using the values as presented by Turteltaub et al. [53]. The fiber-matrix interface has been assumed to be a weak interface.

Table 4.1: Material Properties of the fiber, matrix and the interface [26, 14]

	Fiber	Matrix	Fiber-matrix interface	Unit
Density	$1.8 \cdot 10^{-6}$	$1.31 \cdot 10^{-6}$	-	[kg/mm^3]
Elasticity modulus	19	3.52	-	[GPa]
Poisson's ratio	0.23	0.35	-	[-]
Ultimate traction	100	50	25	[MPa]
Fracture energy	0.1	0.05	0.025	[N/mm]

The input parameters for the defects are divided into the input parameters for the matrix voids and for the interfiber voids and are shown below.

Matrix Voids The matrix voids are randomly distributed over the MVE. The input parameters for these matrix voids are shown in Table 4.2.

Table 4.2: Input parameters for matrix voids

Input Parameter	Range
Void content	$0 - 8\%$
Number of voids	-
Deviation size (S_d)	$0 - 95\%$
Aspect ratio	$1 - 1.4$

The number of voids depends on the desired area or diameter of the individual voids for that given model. The deviation in size of the different voids is determined using a random value generator that has a range from $[1 - S_d, 1 + S_d]$. Here, S_d is the deviation size of the voids. The individual void size is then calculated as,

$$A_v = \frac{V_d}{\sum V_d \cdot V_C \cdot wh} \tag{4.1}$$

where V_d are the values created by the random value generator as explained previously. V_C is the void content and w,h are the dimensions of the MVE. The aspect ratio of the voids is also determined by a random value generator between the lower and upper bound or the aspect ratio. In the literature study it was found that generally, due to the manufacturing methods, the voids have a circular rod like shape, and thus the aspect ratio in transverse direction is generally rather low, resulting in an aspect ratio between 1 and 1.4. Void orientation is another parameter although it does not require a input parameters as it is a random value between 0 and 180 degrees.

The same fiber distribution is used with increasing void content. This is done in order to decrease the scatter that the fiber distribution has on the final results. Two examples with increasing void content are shown in Figure 4.2 and Figure 4.3. First, with a (nearly) constant deviation of the size ($S_d = 1\%$) as is shown in Figure 4.2. Secondly, in Figure 4.3 with large deviation in the size ($S_d = 80\%$). Here, the volume element size is 62.5 by 62.5mm and the aspect ratio is between 1 and 1.4. In these images it can be seen that by using the constant fiber distribution, purely the void parameters will have an effect on the output properties. The difference between the large and small deviation shows a clear difference in void geometry.

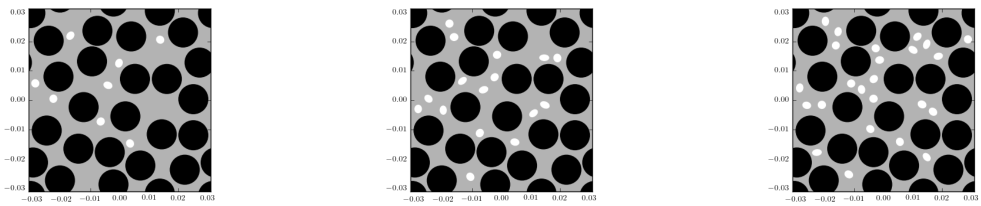

(a) Void content = 2.0 % **(b)** Void content = 4.0 % **(c)** Void content = 6.0 %

Figure 4.2: Increasing void content from 2 % (a) to 6 % in (c). Here, the void aspect ratio has a distribution of 1 to 1.4 and a size deviation of 1%

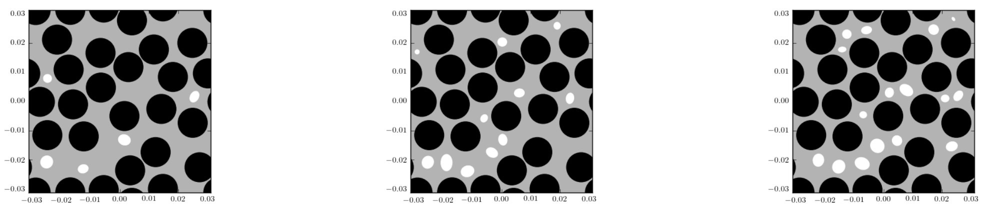

(a) Void content = 2.0 % **(b)** Void content = 4.0 % **(c)** Void content = 6.0 %

Figure 4.3: Increasing void content from 2 % (a) to 6 % in (c). Here, the void aspect ratio has a distribution of 1 to 1.4 and a size deviation of 80%

Interfiber Voids Only two input parameters are required for the interfiber void. The first is the amount of fibers, which is either three or four fibers. The second is whether the interfiber void is actually a void or whether the space between the fibers is filled with matrix. This creates the possibility to have a fiber distribution with multiple interfiber void locations that can have a range of void contents. Using this the effects of the interfiber void content can be determined. In Table 4.3 an overview of the input parameters and the parameters that are randomly generated can be found. The offset parameter, which is used for interfiber voids with four fibers is schematically represented in Figure 4.4, here α is the offset which ranges from 10 to 20 degrees.

Table 4.3: Input parameters and randomly generated parameters for interfiber void

Input Parameter	Range
Type of interfiber voids	3 or 4
Void between fibers	True of False
Randomly generated parameter	Range
Orientation	$0 - 180°$
Offset (only for four fibers)	$10 - 20°$

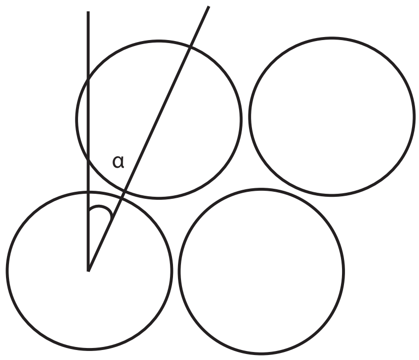

Figure 4.4: Schematic representation of the offset parameter for a interfiber void containing four fibers

In both types of interfiber void, there is still a small opening between the individual fibers. This offset is created to remove the bad aspect ratio mesh at the location where the two fibers would meet without this offset. Another advantage of this opening is that now both interface cohesive elements and matrix cohesive elements are at the weakest location of the interfiber voids. This results in a more accurate representation of the possible cracks that can form at the void boundary. The mesh of the interfiber voids with three fibers and four fibers are shown in Figure 4.5a and Figure 4.5b respectively.

The interfiber voids have a discrete void content. For the interfiber void with three fibers, the method of calculating the void content is by first determining the area of the equilateral triangle which connects the three fibers. Then the area of the fibers that is inside the triangle have to be subtracted, as

$$A_{gap} = A_{\Delta} - 3 \cdot A_{fib} \tag{4.2}$$

where

$$A_{\Delta} = \frac{\sqrt{3}}{4}(2l)^2 \tag{4.3}$$

$$A_{fib} = a^2 \frac{\pi}{6} \tag{4.4}$$

$$l = 1.05 \cos\frac{\pi}{6} 2a \frac{\sqrt{3}}{3} \tag{4.5}$$

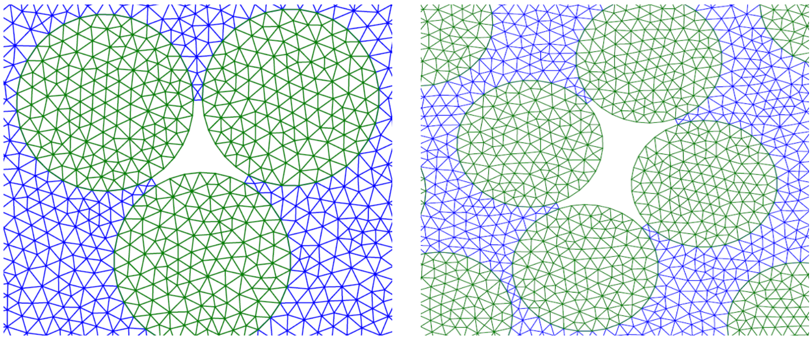

(a) Interfiber void with three fibers in a simulation

(b) Interfiber void with four fibers in a simulation

Figure 4.5: General shape and mesh of the interfiber voids

and where the distance l is the increased distance between the fibers which is required to ensure the proper mesh and can be found in Equation (4.5). Here for both the four and three interfiber void, the distance from the center of the triangle/parallelogram to the fiber origins is increased by 5%.

For the interfiber void with four fibers a similar approach is taken, where instead of the triangle a parallelogram has to be used. The offset angle α, as shown in Figure 4.4, also has an influence on the area, resulting in the calculation of the area as

$$A_{gap} = A_{paral} - 2 * A_{fib1} - 2 * A_{fib2} \tag{4.6}$$

where

$$A_{paral} = l^2 \sin \frac{\pi}{2} - \alpha \tag{4.7}$$

$$A_{fib1} = \pi a^2 \frac{(\frac{\pi}{2} - \alpha)}{2\pi} \tag{4.8}$$

$$A_{fib2} = \pi a^2 \frac{(\frac{\pi}{2} - \alpha)}{2\pi} \tag{4.9}$$

$$l = \frac{\frac{1.05}{2}\sqrt{(2a)^2 + (2a)^2 - 6a^2 \cos \frac{\pi}{2} + \alpha}}{\cos \frac{\frac{\pi}{2} - \alpha}{2}}. \tag{4.10}$$

As an example with a MVE of $62.5 \times 62.5 \mu$m, the void content for a interfiber void created by three fibers is 0.15 %. For the interfiber void containing four fibers, the void content ranges from 0.3 to 0.45 %, which is not constant due to the offset range. An example of these interfiber voids in the MVE can be found in Figure 4.6. Here the void content ranges from 0 to 1.5 % .

4.1.2 Fiber and void distribution

For the distribution of the fibers, matrix voids and interfiber voids, the same method as presented in Westbroek [64] for the fibers is used. In that case, only fibers were present. The

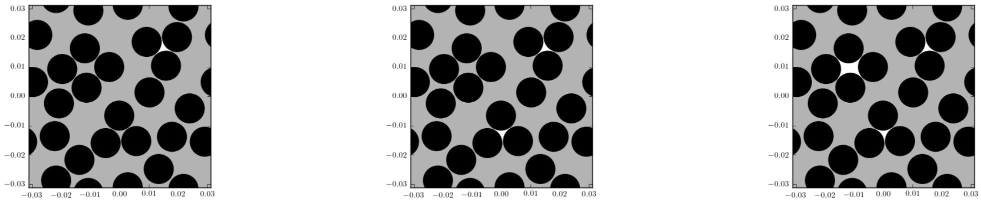

(a) Void content = 0.2 % **(b)** Void content = 0.4 % **(c)** Void content = 1.0 %

Figure 4.6: Increasing void content from 0 % (a) to 1.0 % in (c). Here, two three fiber interfiber voids are used and one four fiber interfiber void

method for a case at which only fibers are present. a grid is created on which the fibers are consecutively placed. When a fiber is placed, the grid locations that have a given distance from the fiber are excluded from the grid for the next fibers. This distance is the fiber radius plus a constant, which is dependent on the mesh size. This is done in order to always have a matrix element between the fibers with a proper aspect ratio. With the exclusion of these grid points for the next fiber, it is ensured that no fibers overlap. The boundaries of this grid for the fiber exceeds the size of the MVE in order to have the no wall effect, resulting in the boundaries of $-a - w/2$ to $a + w/2$ and $-a - h/2$ and $a + h/2$.

This method has been adapted for the matrix voids and interfiber voids as well. This resulted in three separate grids for each item. The grid boundaries of the matrix and interfiber void are different compared to that of the fiber due to the fact the voids will not be able to cross the boundary due to the complications with the periodic boundary conditions and applied loading.

In order to decrease the computational time of the placing of the random distribution of the fibers and voids, first the largest objects are placed. This results in that first the interfiber voids are placed, followed by the fibers and finally the matrix voids.

4.1.3 Mesh generation

Once the fiber and void distribution is known, the mesh has to be generated. This is done by using the random mesh generator of `gmsh` [21]. This mesh generator uses the Delaunay method to create a non structured mesh of triangular elements. As all meshing algorithms, first a 1D Delaunay mesh is constructed on the edges of all the contours using a divide-and-conquer algorithm. Using this algorithm, at the largest adimensional circumradius, new points are added sequentially. In order to reconnect the mesh, the anisotropic Delaunay criterion is used [21]. Once this mesh has been placed, a mesh smoothing of 5 steps is applied as well as a mesh optimizer. The mesh optimizer is used here due to the difficulty of the meshing of the voids. This mesh optimizer ensures that the mesh quality is sufficient at these locations. This will increase the amount of elements with a proper aspect ratio. It is found that with relatively small mesh sizes, such as that of $1e - 3$ mm, the mesh optimization does not have any influence, yet when using larger meshes it does ensure elements of high quality.

The mesh generator also takes the periodic boundary conditions into account by ensuring that the nodes on opposite sides are aligned, for instance for the nodes on the left and right edge: $x_{left} = x_{right} + l$, $y_{left} = y_{right}$. These boundary conditions are discussed in detail in the next section. The mesh generator of `gmsh` only created the bulk elements and nodes. Two examples of a mesh generator by `gmsh` can be found in Figure 4.7. Here, V_C is the void content, R_f is the fiber radius and V_f the fiber content.

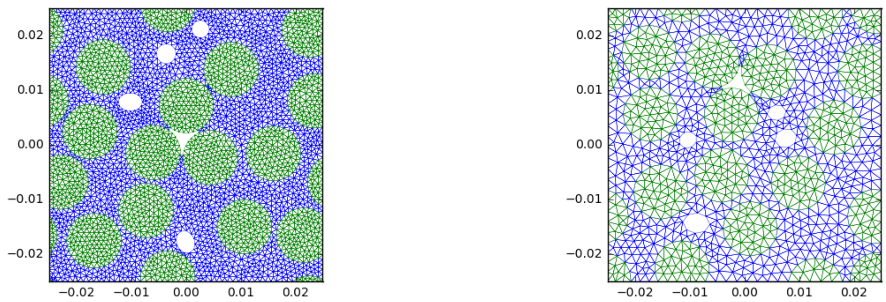

(a) Mesh size $= 1 * 10^{-3} mm$ **(b)** Mesh size $= 2 * 10^{-3} mm$

Figure 4.7: Two examples of a mesh created by `gmsh` with a $V_f = 0.5$, $V_C = 3\%$, $w = h = 5 \cdot 10^{-2}$mm,$R_f = 5 * 10^{-3}$mm

In order to create the cohesive elements, a python script is used as shown in Figure 4.1. First all the nodes are duplicated in order to have multiple unique nodes at each node location and thus the possibility for separation between two bulk elements at that node is enabled. Using these nodes and the common faces between elements, the cohesive elements between the bulk elements are placed.

4.1.4 Boundary conditions

The boundary conditions to ensure the periodicity and apply the displacement gradient on the MVE have been combined. Here first the periodic boundary conditions are discussed. After which the applied displacement boundary conditions are discussed.

The periodic nodes, as created by `gmsh`, have to be given a relation with respect to each other for the `Abaqus`® to process. These periodic boundary conditions ensure that the displacement field on the left side of the MVE is equal to that of the right side, and for the top side equal to the bottom side. This is represented by

$$\Delta \boldsymbol{u}_L = \Delta \boldsymbol{u}_R \tag{4.11}$$
$$\Delta \boldsymbol{u}_T = \Delta \boldsymbol{u}_B. \tag{4.12}$$

This method is straight forward without any cohesive elements present, yet in this study cohesive elements are required to have a progressive damage model with the crack being able to pass through the boundary, consequently the nodes on the boundary have to be duplicated. As it is possible that the same node is duplicated four times on one side while for example only three times on the other side, the duplication is not as straight forward anymore. van Hoorn [60] has proposed a solution for this, as is shown in Figure 4.8. In this Figure it can be seen that only two nodes at each node location are coupled, as is indicated in red. These nodes are part of the elements that have a face on the boundary of the MVE. This method with the coupling of the duplicated nodes, ensures that the crack is able to penetrate the boundary and propagate on the other side of the MVE. For the `Abaqus`® input file this is implemented using a coupling equation between the specific nodes for the displacement.

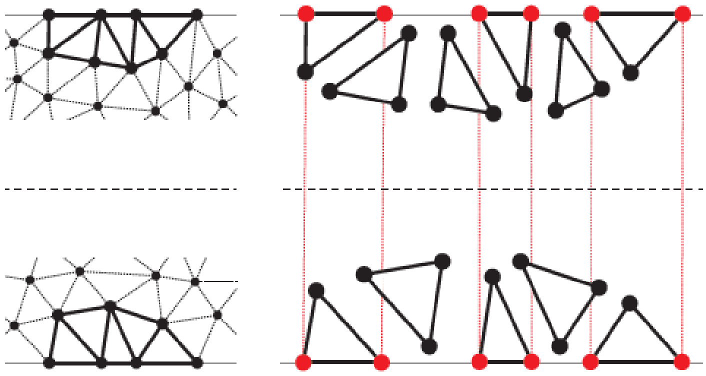

Figure 4.8: Method used to define the nodes pairs, on the left the top and bottom part of the MVE can be found, and on the right the node pairs can be seen in detail in red [60, 53].

For the mechanical boundary conditions, two dummy nodes have been added. The displacement of all the node pairs, as discussed above, is related to the applied displacement of these dummy nodes. For the top and bottom boundary this is related to the dummy node: D-TB and for the left and right boundary the dummy node: D-LR. This has been visualized in Figure 4.9 and is presented for a random node pair on the left and right boundary as

$$\boldsymbol{u}^R - \boldsymbol{u}^L - \begin{bmatrix} \epsilon_{11} w \\ \epsilon_{21} w \end{bmatrix} = \mathbf{0}. \tag{4.13}$$

Three distinct loading cases are used in this study, which are the constraint extension, bi-axial extension-compression (pure shear) and a mixed loading. The strain tensor of these loading cases can be found in Table 4.4. The strain tensor that is used to describe these loading cases is decribed as

$$\boldsymbol{\epsilon} = \begin{bmatrix} \epsilon_{11} & \epsilon_{12} \\ \epsilon_{21} & \epsilon_{22} \end{bmatrix}. \tag{4.14}$$

4.1.5 Abaqus input file

As is mentioned previously, the `Abaqus`® solver is used for the microscale simulations. The `Abaqus`® input file is created by using `python`. In this section some important parts of the input file are discussed in detail.

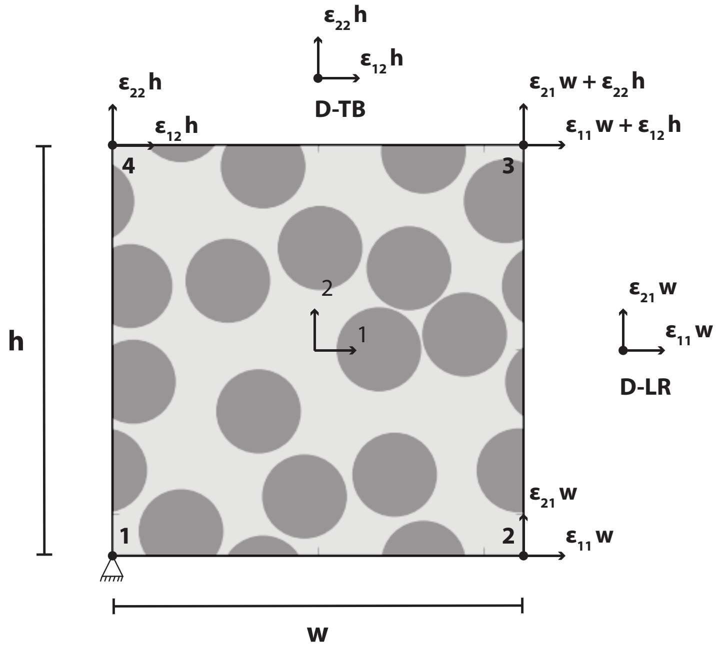

Figure 4.9: An Illustration of the boundary conditions. In the simulations two dummy nodes and the four corner nodes are used to apply the boundary conditions.

Table 4.4: Loading cases and their deformation gradient commonly used in this study.

Loading Case	Deformation Gradient
Constraint Extension	$\begin{bmatrix} \gamma & 0 \\ 0 & 0 \end{bmatrix}$
Pure Shear	$\begin{bmatrix} \gamma & 0 \\ 0 & -\gamma \end{bmatrix}$
Mixed mode	$\begin{bmatrix} 2\gamma & 0 \\ 0 & -\gamma \end{bmatrix}$

Elements The bulk elements that are used for these simulations are the 3-Node (triangular) full-integration plane strain elements, which is the CPE3 element. For the cohesive elements the element COH2D4 is used. The orientation and numbering of these elements can be seen in Figure 4.10. For the cohesive element it can be seen that the number of the nodes of this element is counterclockwise. More on the numbering of this element is discussed at the post processing section. For the cohesive elements, element control is added which contains a viscosity of 0.0001. This viscosity is required to ensure the convergence of the models. These convergence issues mainly arise due to the sudden change of stiffness in the cohesive elements created by the bilinear cohesive law.

Solver Settings In the input file also the solver settings can be adapted in order to improve the convergence of the model significantly. Here, for the static load step, an automatic

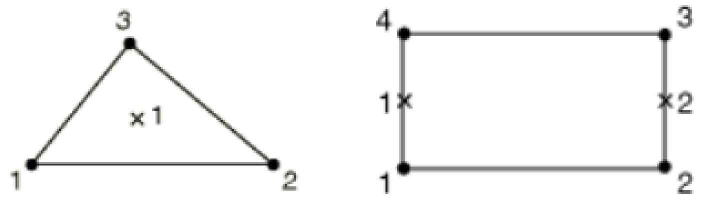

(a) CPE3 **(b)** COH2D4

Figure 4.10: Abaqus elements that are used in the simulations [1]

stabilization option is required. This stabilization gives the `Abaqus`® solver the ability to dissipate energy to cope with sudden loss of stiffness which results in a local instability. The maximum ratio of the stabilization energy with respect to the strain energy is 5%. However, the maximum ratio of 5% is not a boundary for the simulation, and if the simulation requires it, the ratio is increased. If this ratio becomes too large, the simulation loses its physical value, resulting in that for the post-processing this ratio has to always be checked and taken into account.

4.2 Post-Processing

The goal of the computational post processing activities is to determine the effect traction separation. This is determined by using the steps as shown in Figure 4.11. An an output from the `Abaqus`® solver, the .odb file is obtained. This .odb file contains all the information from the simulation of the model. In this section the activities in order to get the Effective Traction Separation Law (ETSL) and its properties.

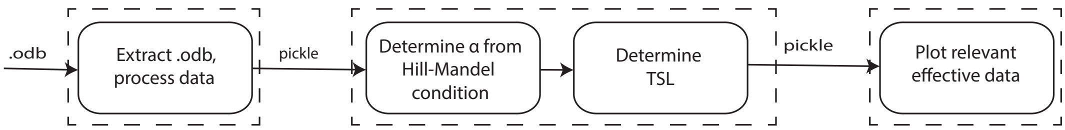

Figure 4.11: Flow chart of the post-processing computational activities

4.2.1 Extract odb and process data

The extraction of the data from the .odb file is done by using a python script. It is possible to use `python` to read that data from the `Abaqus`®.odb file. This is done by using the Abaqus scripting package available in `python`.

The theory of the homogenization has been discussed in detail in Chapter 3. In this section the focus will lie on the implementation of this theory. First, the last increment has to be determined, since the information of the last increment is required for the other time steps. This is done by having the loop run backwards, and thus processing the data from the last increment to the first. In this loop over the time, both the bulk elements and cohesive elements are looped over individually.

Failed cohesive elements First, the failed elements on the microscopic model have to be determined. From a theoretical point of view, a cohesive element has fully failed when the final effective opening (δ_f) has been reached. The selection method in `Abaqus`® the output variable, SDEG. This output variable shows the damage variable of the cohesive element, and is ranged between 0 at which the cohesive element if fully intact and 1 at which the element has completely failed. Since the value 1 might not get reached due to convergence issues and numerical inaccuracies, a cut off value is used which is based on the residual strength. The cut off value was defined as the point when the cohesive element was unable to carry a maximum traction of 20% of an undamaged cohesive element.

The cohesive element that have failed are stored and later used for the crack averaged properties. Here, as stated previously, both the main crack, its bifurcations and isolated parts are taken into account for the crack averaged properties.

Data from failed cohesive elements For the opening of the cohesive element the difference of displacement between the two sides of the cohesive element are used, and is defined as

$$[\![\boldsymbol{u}]\!] = \boldsymbol{u}_4 + \boldsymbol{u}_3 - \boldsymbol{u}_2 - \boldsymbol{u}_1 \tag{4.15}$$

where the numbering 1 to 4 stands for the four different nodes as shown in Figure 4.10.

The singular value decomposition, as was previously required to determine the data from the cohesive element, resulted in loss of information and thus also energy. A solution has been proposed in Hirch [28] which has been slightly altered to increase its readability and for a better understanding of the equations.

The reason why a singular value decomposition was required for the cohesive elements was that the orientation and numbering of the elements could be different for each cohesive element, as has been visualized in Figure 4.12. This resulted in that the normal and opening of the cohesive element could be in opposite directions. When doing the integral over these elements the opening and normal would then cancel each other. At first, to counter-act this, the tensor product was used and because of that also a singular value decomposition of the tensor.

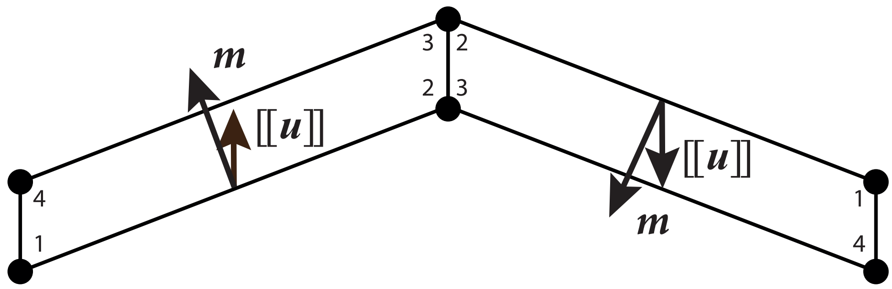

Figure 4.12: Two Cohesive elements with different orientation of the opening and normal, which is created due to the different configuration of the nodes (1-4)

A solution that involves the projection of the opening or normal per element on a reference frame was found. An example of this projection for the element opening is as follows

$$[\![\boldsymbol{u}]\!]^* = \frac{\boldsymbol{m}\cdot\boldsymbol{e}_1}{|\boldsymbol{m}\cdot\boldsymbol{e}_1|}[\![\boldsymbol{u}]\!] \tag{4.16}$$

where m is the element normal, and e_1 is a reference vector, which is in this case the global vector $e_1 = [1, 0]$. $[\![\boldsymbol{u}]\!]$ is the current opening of the element and $[\![\boldsymbol{u}]\!]^*$ is the element opening with the correct 'global' orientation. It should be noted that special configurations can occur where the dot product of these vectors is zero. If this is the case, a different reference vector is selected, $e_2 = [0, 1]$. The value of the fraction in Equation 4.16 is always either 1 or -1. It is -1 if the vector has to be flipped to ensure the alignment with the other elements in the direction of the reference vector. In this study the crack will most likely be either vertical or at an angle of $\pm 45°$, resulting in that this reference vector is sufficient. If a horizontal crack is expected, this reference vector should be changed to for instance the e_2 vector. The same method can be applied for the element opening, as is found Equation (4.16), can also be done to flip the element normal vector and traction in the correct direction as follows

$$\boldsymbol{m}^* = \frac{\boldsymbol{m} \cdot \boldsymbol{e}_1}{|\boldsymbol{m} \cdot \boldsymbol{e}_1|}\boldsymbol{m} \tag{4.17}$$

$$\boldsymbol{t}^* = \frac{\boldsymbol{m} \cdot \boldsymbol{e}_1}{|\boldsymbol{m} \cdot \boldsymbol{e}_1|}\boldsymbol{t}. \tag{4.18}$$

Microscopic properties The microscopic traction on the crack is determined as follows,

$$P_\Gamma = \frac{1}{\Omega}\int_\Gamma \boldsymbol{t}^* \cdot [\![\dot{\boldsymbol{u}}^*]\!] \tag{4.19}$$

where only the cohesive elements that have failed will be used, as have been determined previously. The integral of this equation is calculated in the `python` script, which consist of a summation over the elements, i.e.,

$$\int_\Gamma x = \sum_{i=1}^{N_{coh}^\Gamma} x \cdot l_i \tag{4.20}$$

where l_{coh} is the length of that cohesive element and N_{coh}^Γ are all the cohesive elements that have failed. This method has been used for all the integrals over the crack surface. For the bulk elements a similar approach is used as for the cohesive elements.

Effective properties For the effective properties, both the crack normal and crack averaged traction ($\boldsymbol{t}_\Gamma^f$) are calculated using the normal or traction of the failed cohesive elements and determining the average from that

$$\boldsymbol{m}^{\mathrm{f}} := \frac{1}{|\Gamma|}\int_\Gamma \boldsymbol{m}^* d\Gamma \tag{4.21}$$

$$\boldsymbol{t}_\Gamma^{\mathrm{f}} := \frac{1}{|\Gamma|}\int_\Gamma \boldsymbol{t}^* d\Gamma. \tag{4.22}$$

The effective crack opening vector $[\![\boldsymbol{u}]\!]^f$ is defined as

$$|\Gamma|^{\mathrm{f}} [\![\boldsymbol{u}]\!]^{\mathrm{f}} := |\Gamma| \langle [\![\boldsymbol{u}]\!] \rangle_{\Gamma} \tag{4.23}$$

where it should be noted that this is different to the theory as presented in Chapter 3 as rank-one approximation is not necessary anymore, resulting in that by definition the left and right side should be equal.

4.2.2 Determine Hill-Mandel condition and ETSL

From the effective traction, opening and crack length, the effective rate of work can be determined. As stated previously, a combination of the crack averaged and bulk averaged rate of work has to match the microscopic rate of work. The equations for the microscopic rate of work, crack averaged, bulk averaged and void boundary rate of work can be found in Equation 4.24. The comparison between these stress powers can be found in Figure 4.13. Here the magenta line is the combination between the crack averaged and bulk averaged stress power. The black dotted line is the influence of the voids, as shown in Equation 4.24d. In this figure it is required to look at two things. First, the magenta line should coincide with the brown line. The magenta line is a combination of the blue and red line with the value α. Second, the rate of work of the voids should be approximately zero. The microscopic and macroscopic powers are defined as

$$P_{\Gamma} = \frac{1}{\Omega} \int_{\Gamma} \boldsymbol{t} \cdot [\![\dot{\boldsymbol{u}}]\!] \mathrm{d}\Gamma \tag{4.24a}$$

$$P_{\Gamma}^{\mathrm{f}} = \frac{1}{\Omega} \left|\Gamma^{\mathrm{f}}\right| \boldsymbol{t}_{\Gamma}^{\mathrm{f}} \cdot [\![\dot{\boldsymbol{u}}]\!]^{f} \tag{4.24b}$$

$$P_{\Omega}^{\mathrm{f}} = \frac{1}{\Omega} \left|\Gamma^{\mathrm{f}}\right| \langle \boldsymbol{\sigma} \rangle_{\Omega} \boldsymbol{m}^{\mathrm{f}} \cdot [\![\dot{\boldsymbol{u}}]\!]^{\mathrm{f}} \tag{4.24c}$$

$$P_{\mathrm{v}} = \sum_{k=1}^{N_v} \frac{1}{|\Gamma|} \int_{\partial v^k} \langle \boldsymbol{\sigma} \rangle_{\Omega} \cdot [\dot{\boldsymbol{u}}^{\mathrm{v}} \otimes \boldsymbol{m}^{\mathrm{v}}] \mathrm{d}s. \tag{4.24d}$$

From Figure 4.13 the value of α can be determined, which in this example is 0.6. This is determined by using a combination of the crack averaged properties (blue line) and bulk averaged properties (red line). However it can be seen that the brown line after $t = 0.1s$, does not coincide with the magenta line anymore. When looking at both the energy plot and deformation plot of the model, it can be found that the crack has already fully propagated in the MVE and the regulatiztion is above its threshold.

As explained in the Section 4.1, stabilization is required in the models, in Figure 4.14a it can be checked whether this energy does not exceed the maximum of 5%. The crack formation occurs at $t = 0$ to $t = 0.12$, as seen at the rate of work plot. At these this it can be seen that it does not exceed the 5%.

Using the value of α as determined from using the stress power, the effective traction separation law can be determined. For this, the macroscopic traction is plotted with respect to the macroscopic opening, as are presented above. For this, both a tangential traction (mode II) and normal (mode I) traction with respect to the macroscopic crack orientation can be

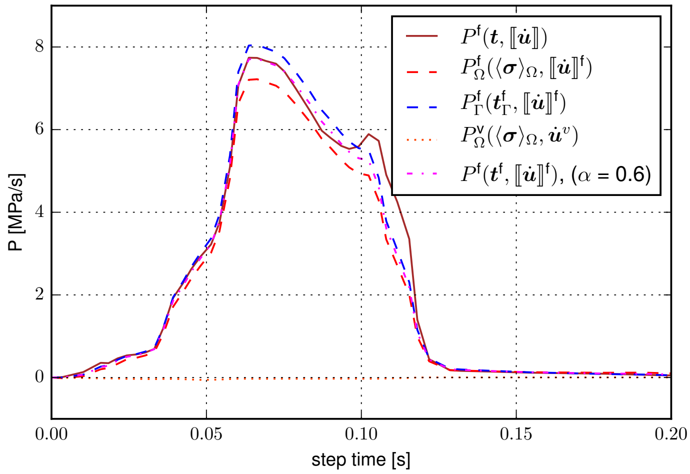

Figure 4.13: The stress power of a simulation.

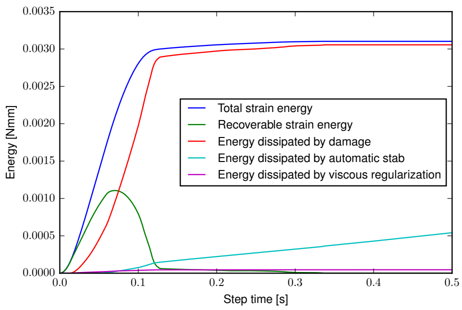

(a) The energy plot.

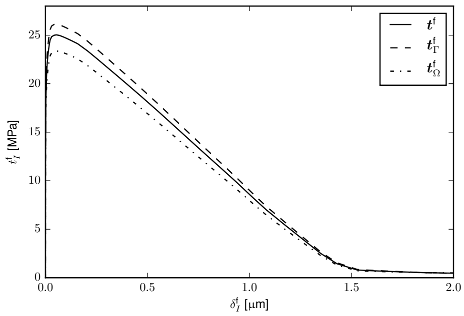

(b) The normal (mode I) ETSL with $\alpha = 0.6$

Figure 4.14: The energy and ETSL a simulation

plotted. In Figure 4.14b an example of the in normal direction ETSL is shown. Since a constraint extension force was applied, the tangential traction is negligible. It can be seen that the final ETSL is a combination of the crack averaged and bulk averaged Traction-Separation Law (TSL).

Chapter 5

Verification and Convergence Studies

In this chapter the verification of the theory, mesh convergence and Representative Volume Element (RVE) convergence are discussed. Two verifications are performed in this chapter. First the verification of the rate of work of the voids is done in Section 5.1. Followed by the verification of the vector decomposition as presented in the previous chapter in Section 5.2. After this the mesh convergence study for each Microstructural Volume Element (MVE) size is done. A small mesh convergence is done for the interfiber voids to determine the effect of the mesh size and interfiber orientation. Finally the mesh converged MVE sizes are used to determine the RVE size.

5.1 Verification of the Hill-Mandel condition in the presence of voids

For the verification of the voids that have been added on the microstructural volume element, two numerical models have been created. These numerical models have large, critical voids in the assumed crack path, as is shown in Figure 5.1. Here, Figure 5.1a has a constraint extension boundary condition and will thus have a vertical crack. Figure 5.1b has a biaxial extension-contraction (pure shear) boundary condition, which results in the crack at 45°. These three large voids ensure a crack path in which it is expected that the voids have a large impact on the properties. For simplicity in the models, no fibers are modeled in order to keep the voids the primary parameter.

For the constraint extension load case, two extra voids are modeled which are expected to not be part of the main crack. This is done to see the effect of these voids on the properties while they are not part of the main crack. The deformation for the constraint extension and pure shear cases can be seen in Figure 5.2a and Figure 5.2b respectively.

For the verification, it has to be determined whether the rate of work on the void boundary is approximately zero. This ensures that the assumptions done in Chapter 3 are valid. The rate of work plot, is shown in Figure 5.3a for constraint extension and in Figure 5.3b for pure shear.

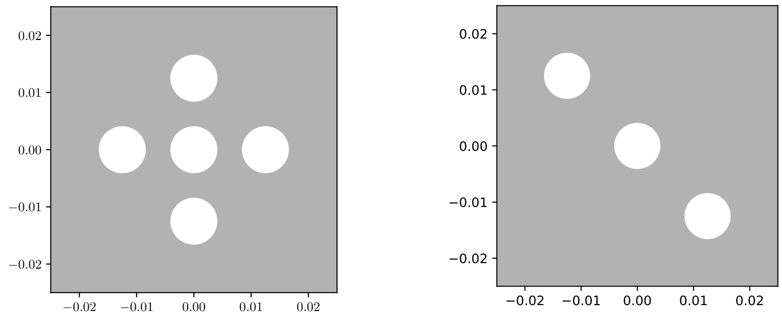

(a) Constraint extension verification case, with a void content of 10%

(b) Pure shear verification case, with a void content of 6%

Figure 5.1: Verification cases voids, geometry

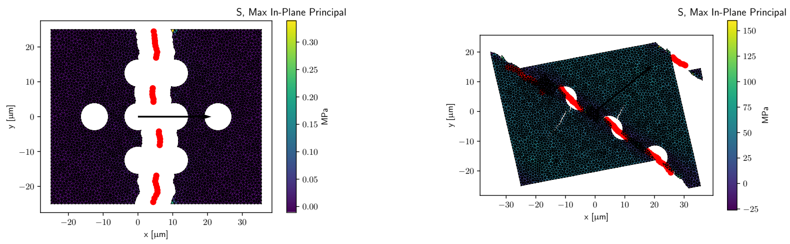

(a) Constraint extension with a void content of 10%.

(b) Pure shear with a void content of 6%.

Figure 5.2: Verification cases voids, deformation of the numerical models. Here, the red dots are the failed cohesive elements

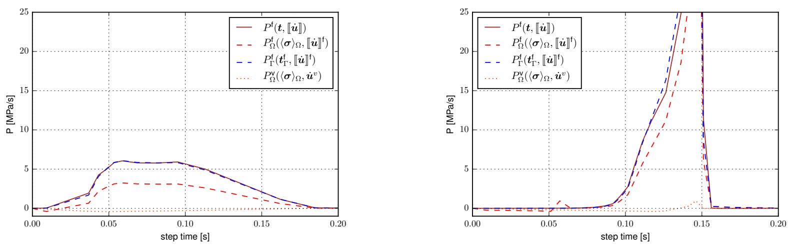

(a) Constraint extension with a void content of 10%.

(b) Pure shear with a void content of 6%.

Figure 5.3: Verification cases voids, rate of work of the numerical models

The dashed line is the first part of Equation 3.30. In the constraint extension case, it can be found that it is approximately zero. For the shear case it can be found that when the other powers go to infinity, the rate of work on the voids also increases, yet in comparison to the power of the microstructure, this can be neglected. It can be concluded that in both the constraint extension and pure shear mode the rate of work of the voids is approximately zero. This results in that there is no effect of the voids on the crack, from which it can be found that the change of theory and assumptions as discussed in Chapter 3 are valid.

5.2 Verification of the Vector decomposition

The verification of the vector decomposition will look at the rate of work (power) of the model and it will show how the Hill-Mandel condition is satisfied. The effective traction separation law is also shown to see the effect of the change on the effective properties. This is done for constraint extension, pure shear and a mixed mode loading case. The three loading cases are shown in Table 5.1. For the pure shear loading, the boundary condition is chosen so that the deformation of the volume element is pure shear under 45°. The MVE geometry is fiber reinforced composite without any defects.

Table 5.1: Loading cases and their deformation gradient for the verification of the first adaptation.

Loading Case	Deformation Gradient
Constraint Extension	$\begin{bmatrix} \gamma & 0 \\ 0 & 0 \end{bmatrix}$
Pure Shear	$\begin{bmatrix} \gamma & 0 \\ 0 & -\gamma \end{bmatrix}$
Mixed mode	$\begin{bmatrix} 2\gamma & 0 \\ 0 & -\gamma \end{bmatrix}$

Constraint Extension loading case

In order to verify the vector decomposition method, and its difference to the previous method using an Singular Value Decomposition (SVD), the rate of work of both methods are shown. These type of plots show the macroscopic effective rate of work using either the crack averaged properties or the bulk averaged properties and the microscopic rate of work. It is required that a combination of the macroscopic crack averaged (P^f_Γ) and bulk averaged (P^f_Ω) rate of work equals the microscopic rate of work.

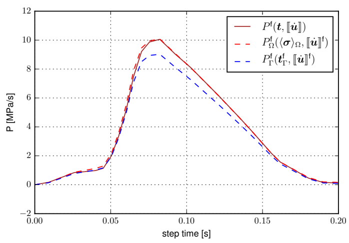

(a) The SVD method

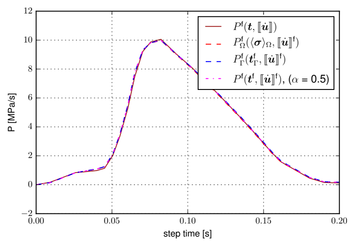

(b) The vector decomposition method

Figure 5.4: Crack averaged, bulk averaged and microstructural rate of work for a constraint extension loading case

In Figure 5.4 it is found that with the initial methodology the rate of work of the bulk-averaged effective rate of work (P^f_Ω) is found to coincide with the microscopic rate of work of the crack. For the crack-averaged effective power this is not the case. With the vector decomposition it can be found that there is a clear improvement as now also the P_Γ^f coincides with the microscopic rate of work.

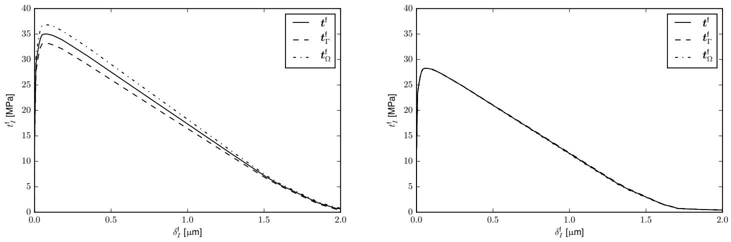

(a) The SVD method **(b)** The vector decomposition method

Figure 5.5: Normal traction separation law in case of a constraint extension load case

For the effective traction, as is shown in Figure 5.5, it can be found that both the crack-averaged effective traction ($\boldsymbol{t}_\Gamma^f$) and bulk-averaged effective traction ($\boldsymbol{t}_\Omega^f$) decrease. In Figure 5.5 the microscopic rate of work and the macroscopic rate of works coincided with the vector decomposition method. In models which have crack bifurcations, these do not coincide, but with the new theory the macroscopic rate of works do converge to the microscopic rate of power and thus the overall method is improved.

Shear loading case

In case of the pure shear (biaxial extension-compression) the rate of work is shown in Figure 5.6. In these figures it can be seen that the rate of works of the macroscale properties do not coincide with the microscopic rate of work such as in the constraint extension case. However, it does converge towards the microscopic rate of work. The overall traction decreases as is found in Figure 5.7

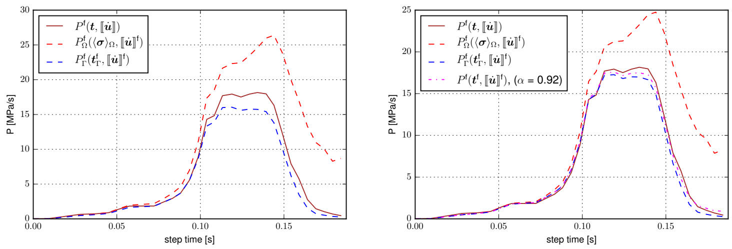

(a) The SVD method **(b)** The vector decomposition method

Figure 5.6: Crack averaged, bulk averaged and microstructural rate of work for a pure shear loading case

Mixed Mode loading case

It can be found in Figure 5.8, that for the mixed mode loading case the microscale rate of work gets outside of the two averaged rate of works. For this loading case, in the first part

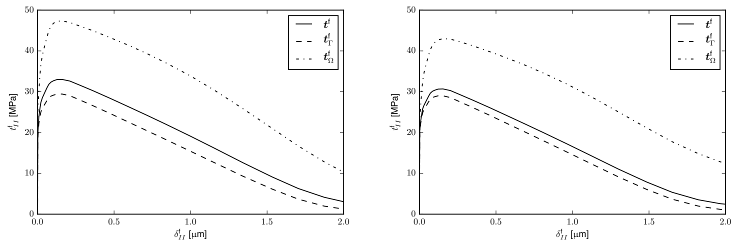

(a) The SVD method **(b)** The vector decomposition method

Figure 5.7: Transverse traction separation law in case of a shear load

of the numerical model (until $t = 0.15$), the vector decomposition method shows that the macroscale rate of work was closer to the microscale. However, at the large peak of the rate of work the SVD method is more accurate. The numerical model showed that after $t = 0.15$ the volume element already has a complete crack and numerical errors occur such as mesh overlapping and since a high viscous regulation is required. From this it can be concluded that the first part of the rate of work is the most important and the vector decomposition method works better at this location for the mixed mode loading.

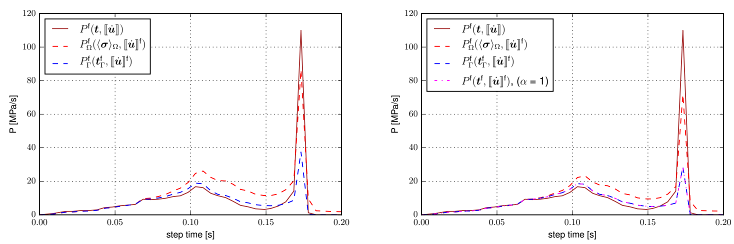

(a) The SVD method **(b)** The vector decomposition method

Figure 5.8: Crack averaged, bulk averaged and microstructural rate of work for a mixed mode loading case

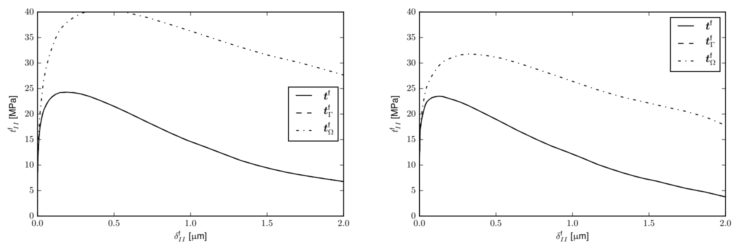

(a) The SVD method **(b)** The vector decomposition method

Figure 5.9: Transverse traction separation law in case of a mixed loading for both methods

5.3 Mesh Convergence

The mesh convergence is performed for each loading case at each volume element size. For each mesh size at each loading case, five realizations are made. The volume element sizes that are modeled are $25 \times 25\mu$m, $37.5 \times 37.5\mu$m, $50 \times 50\mu$m, $62.5 \times 62.5\mu$m, $75 \times 75\mu$m and $100 \times 100\mu$m. In the mesh convergence, not only the effect of the different loading, but also the effect of the voids is an important aspect. It is assumed that the void area and void type do not have impact on the convergence study. It is chosen that the void content, void area and distribution of void aspect ratio remains constant, with a void content of 3%. This results in an increasing number of voids with respect to the volume element. For the smaller volume elements (25×25,37.5×37.5 and 50×50) the mesh sizes of 3μm, 2μm, 1μm and 0.5μm are used. For the three larger volume elements, due to the increase in computation time the mesh size of 0.5μm is not modeled. Example of the mesh sizes of $25 \times 25\mu$m, $50 \times 50\mu$m, $75 \times 75\mu$m and $100 \times 100\mu$m can be found in Figure 5.10, 5.11, 5.12 and 5.13 respectively. It can be seen that due to the mesh optimization, a mesh refinement near the voids occurs.

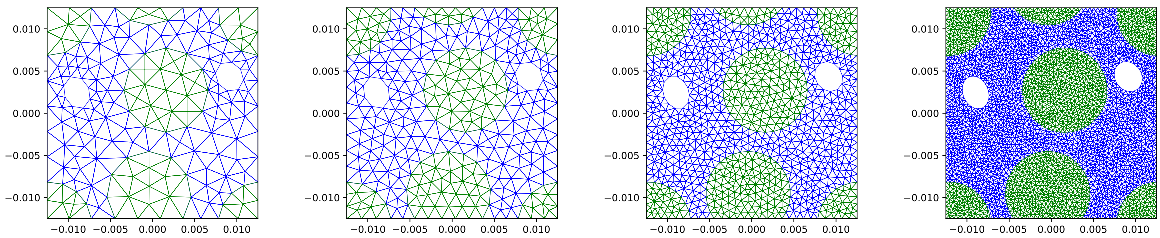

(a) Grid size of 3 μm **(b)** Grid size of 2 μm **(c)** Grid size of 1 μm **(d)** Grid size of 0.5 μm

Figure 5.10: Example of volume element of 25X25 μm, using finer meshes with a constant fiber and void distribution

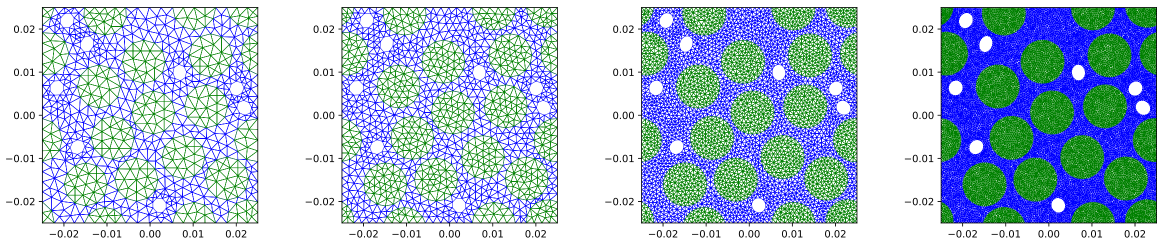

(a) Grid size of 3 μm **(b)** Grid size of 2 μm **(c)** Grid size of 1 μm **(d)** Grid size of 0.5 μm

Figure 5.11: Example of volume element of 50X50 μm, using finer meshes with a constant fiber and void distribution

For the mesh convergence, the Effective Traction Separation Law (ETSL) and the crack content is used. The crack content is used to determine the fraction of the crack, which could be in the matrix of the composite or on the interface between the fiber and matrix. The crack content is evaluated here as the mesh size can negatively impact the crack content and should thus be converged. For the ETSL the convergence is determined using the scatter of the smallest mesh. It is assumed that is the ETSL of a larger mesh size is within this scatter, that mesh size will be the converged mesh size. Here N_R is the amount of realizations used.

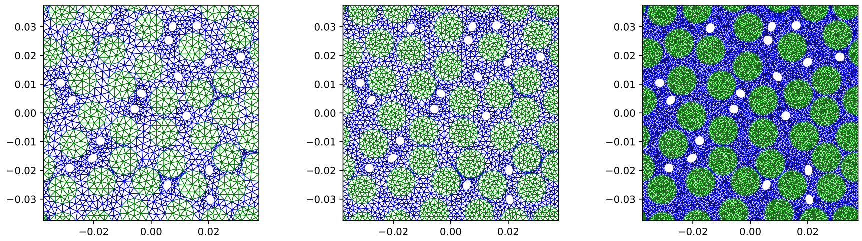

(a) Grid size of 3 μm **(b)** Grid size of 2 μm **(c)** Grid size of 1 μm

Figure 5.12: Example of volume element of 75X75 μm, using finer meshes with a constant fiber and void distribution

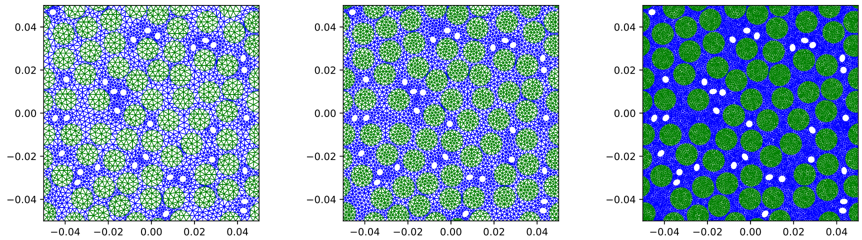

(a) Grid size of 3 μm **(b)** Grid size of 2 μm **(c)** Grid size of 1 μm

Figure 5.13: Example of volume element of 100X100 μm, using finer meshes with a constant fiber and void distribution

The effect of the mesh sizes is determined for each loading case and for each MVE size. For each loading case the mesh convergence is discussed below.

5.3.1 Constraint Extension loading case

With the constraint extension case, the crack mainly opens in a normal direction, and thus for the convergence, this direction is used. The ETSL for each volume element can be found increasing order in Figure 5.14 to Figure 5.19. In each ETSL a dot can be found where the line is thinner afterward, this indicates the location at which the viscous energy is too large.

Table 5.2: The converged mesh size for each MVE size for the constraint extension loading case

MVE size [μm]	Converged Mesh Size
25×25	3
37.5×37.5	2
50×50	1
62.5×62.5	3
75×75	3
100×100	3

The table of the converged mesh sizes can be found in Table 5.2. The crack content seemed to have converged for all cases although at the MVE size of $62.5 \times 62.5\mu$m and $75 \times 75\mu$m the crack content seems to diverge with increasing mesh density.

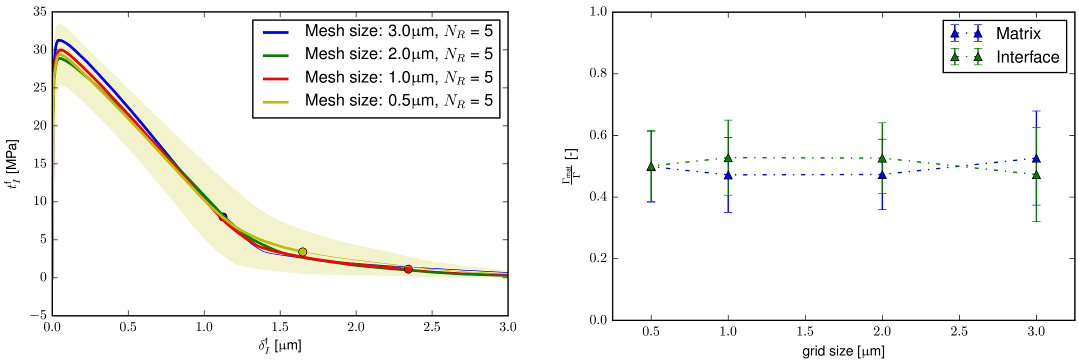

(a) ETSL normal to the crack (mode I)

(b) Crack content

Figure 5.14: Constraint extension with a volume element size of $25x25\mu$m

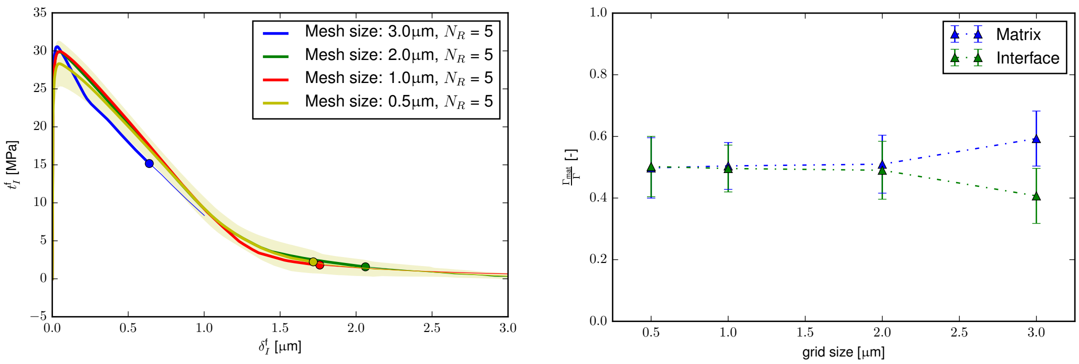

(a) ETSL normal to the crack (mode I)

(b) Crack content

Figure 5.15: Constraint extension with a volume element size of 37.5x37.5 μm

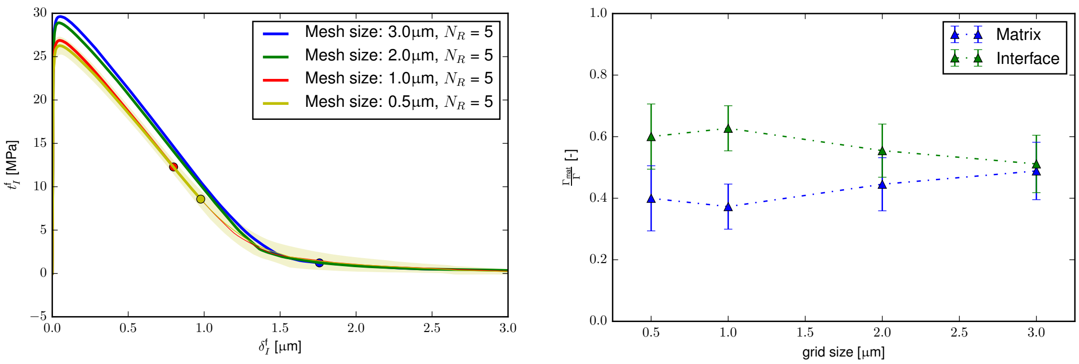

(a) ETSL normal to the crack (mode I)

(b) Crack content

Figure 5.16: Constraint extension with a volume element size of 50x50 μm

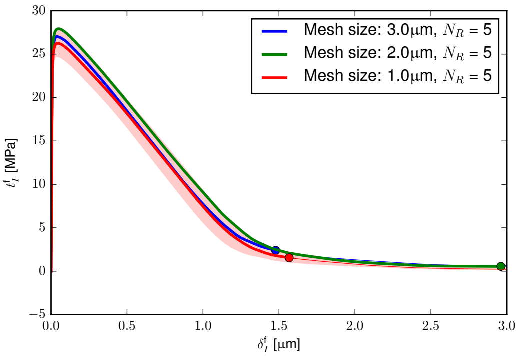

(a) ETSL normal to the crack (mode I)

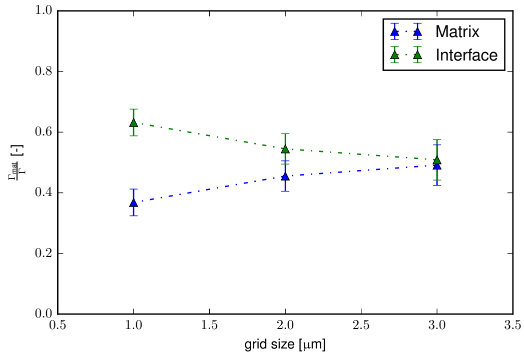

(b) Crack content

Figure 5.17: Constraint extension with a volume element size of 62.5x62.5 μm

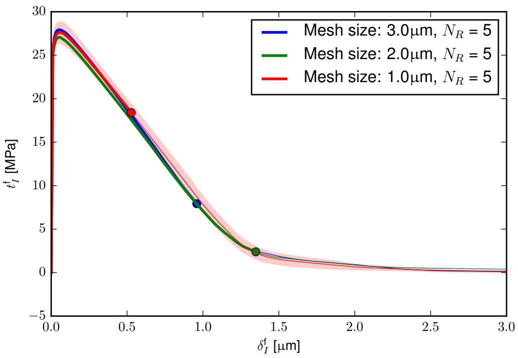

(a) ETSL normal to the crack (mode I)

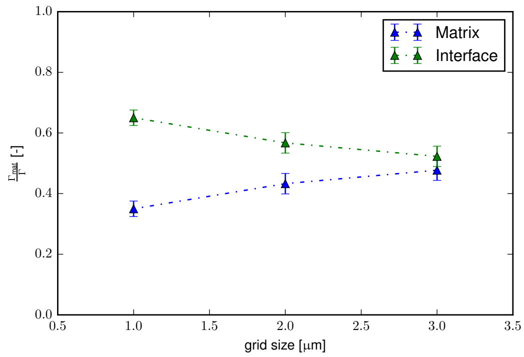

(b) Crack content

Figure 5.18: Constraint extension with a volume element size of 75x75 μm

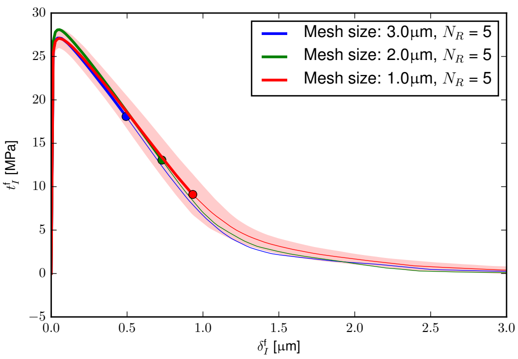

(a) ETSL normal to the crack (mode I)

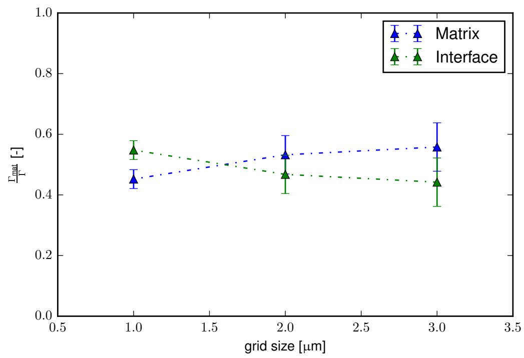

(b) Crack content

Figure 5.19: Constraint extension with a volume element size of 100x100 μm

5.3.2 Pure Shear loading case

For the pure shear case, the tangential ETSL with respect to the crack normal is the most critical, which is denoted in the figures as mode II. The ETSL and crack content for increasing MVE size can be seen in Figure 5.20 to Figure 5.25.

In Table 5.3 the converged mesh sizes can be found for each MVE size in a pure shear loading case. It can be seen that with increasing MVE size on average the mesh size can also be larger.

Table 5.3: The converged mesh size for each MVE size for the pure shear loading case

MVE size [μm]	Converged Mesh Size [μm]
25×25	1
37.5×37.5	0.5
50×50	0.5
62.5×62.5	2
75×75	1
100×100	1

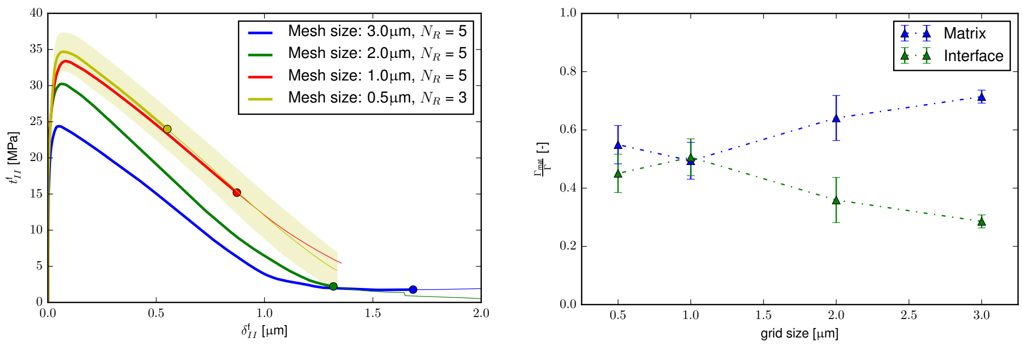

(a) ETSL transverse to the crack (mode II) **(b)** Crack content

Figure 5.20: Shear loading with a volume element size of 25x25 μm

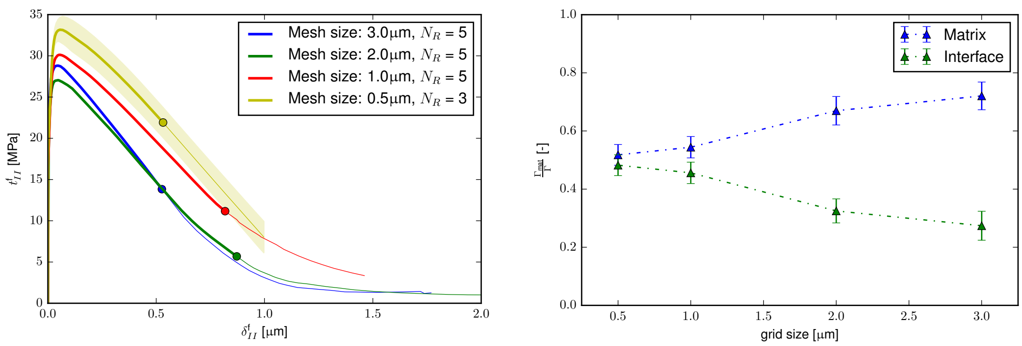

(a) ETSL transverse to the crack (mode II) **(b)** Crack content

Figure 5.21: Shear loading with a volume element size of 37.5x37.5 μm

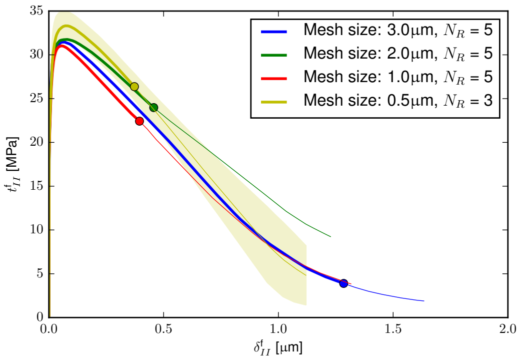

(a) ETSL transverse to the crack (mode II)

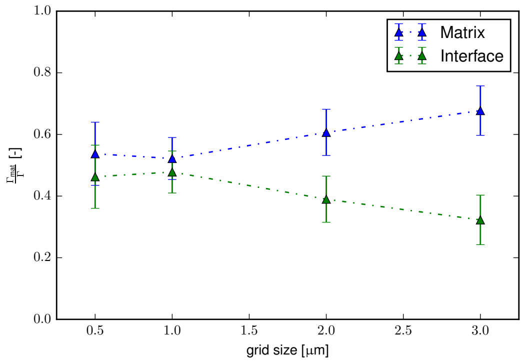

(b) Crack content

Figure 5.22: Shear loading with a volume element size of 50x50 μm

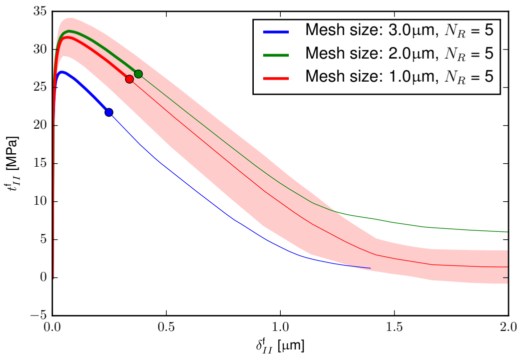

(a) ETSL transverse to the crack (mode II)

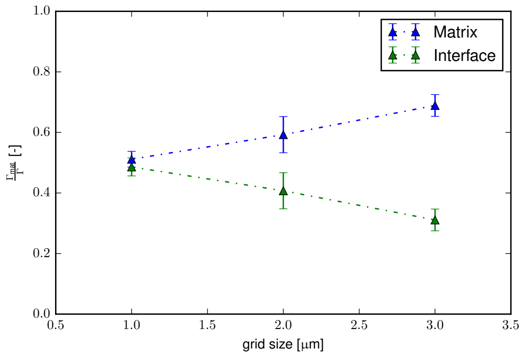

(b) Crack content

Figure 5.23: Shear loading with a volume element size of 62.5x62.5 μm

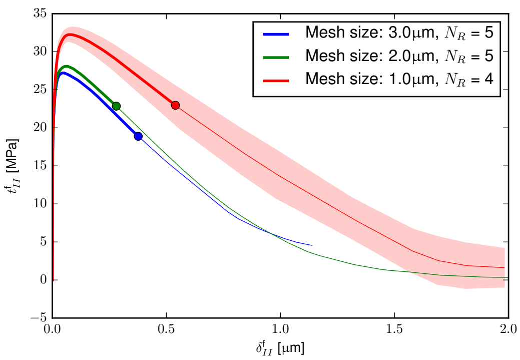

(a) ETSL transverse to the crack (mode II)

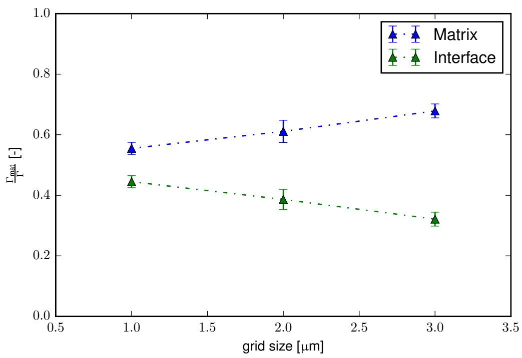

(b) Crack content

Figure 5.24: Shear loading with a volume element size of 75x75 μm

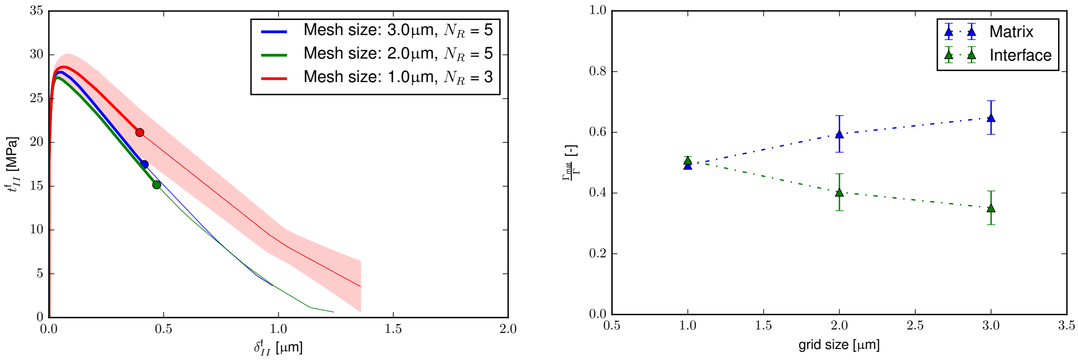

(a) ETSL transverse to the crack (mode II)

(b) Crack content

Figure 5.25: Shear loading with a volume element size of 100x100 μm

5.3.3 Mixed Mode loading case

For the mixed mode loading both the tangential component and normal component are significant. For the convergence study only the tangential component is evaluated to ensure consistency. The ETSL and crack content for increasing MVE size can be seen in Figure 5.26 to Figure 5.31.

Table 5.4: The converged mesh size for each MVE size for the mixed mode loading case

MVE size [μm]	Converged Mesh Size [μm]
25×25	2
37.5×37.5	2
50×50	0.5
62.5×62.5	2
75×75	1
100×100	1

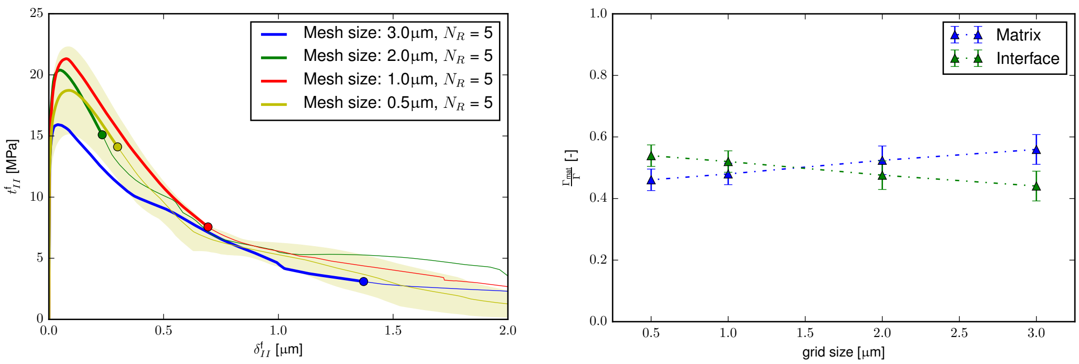

(a) ETSL transverse to the crack (mode II)

(b) Crack content

Figure 5.26: Mixed mode loading with a volume element size of 25x25 μm

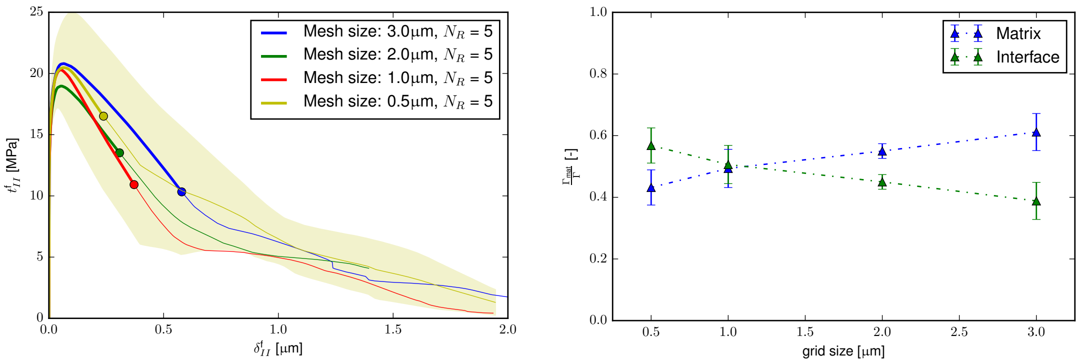

(a) ETSL transverse to the crack (mode II) **(b)** Crack content

Figure 5.27: Mixed mode loading with a volume element size of 37.5x37.5 μm

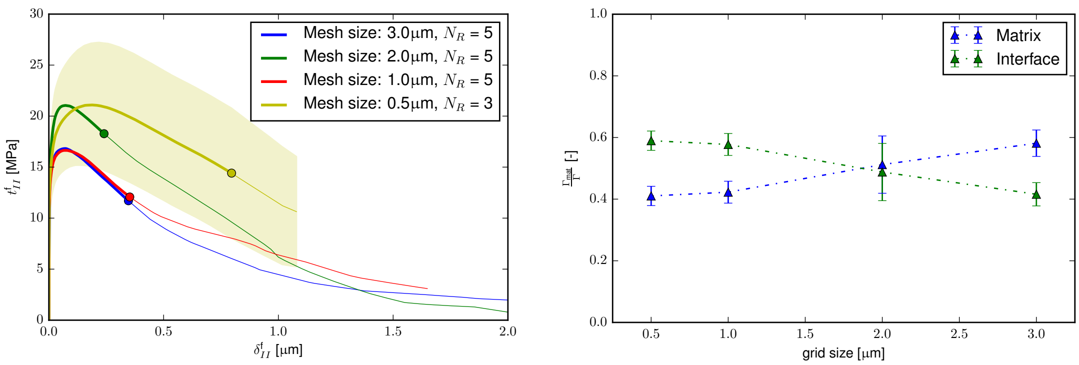

(a) ETSL transverse to the crack (mode II) **(b)** Crack content

Figure 5.28: Mixed mode loading with a volume element size of 50x50 μm

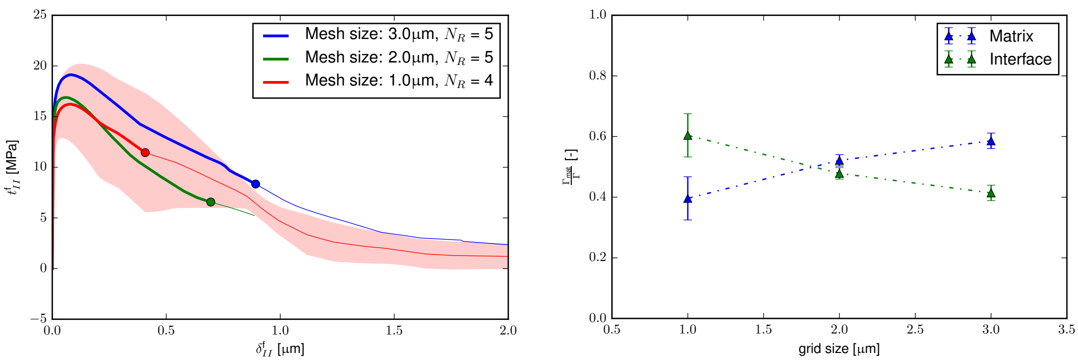

(a) ETSL transverse to the crack (mode II) **(b)** Crack content

Figure 5.29: Mixed mode loading with a volume element size of 62.5x62.5 μm

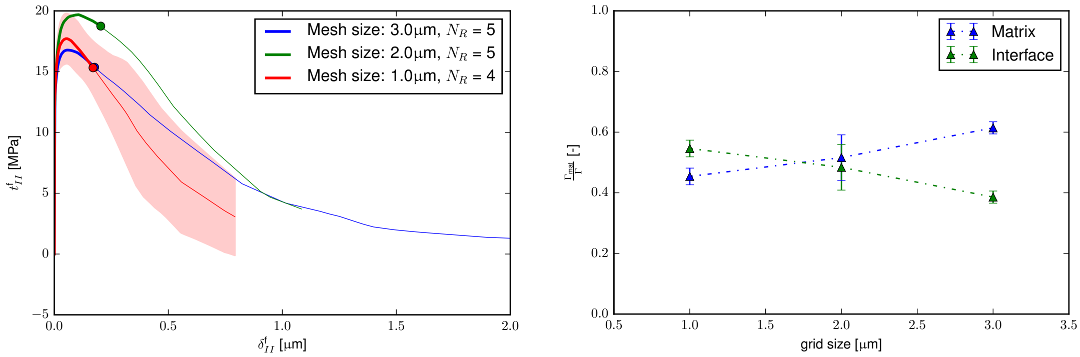

(a) ETSL transverse to the crack (mode II) **(b)** Crack content

Figure 5.30: Mixed mode loading with a volume element size of 75x75 μm

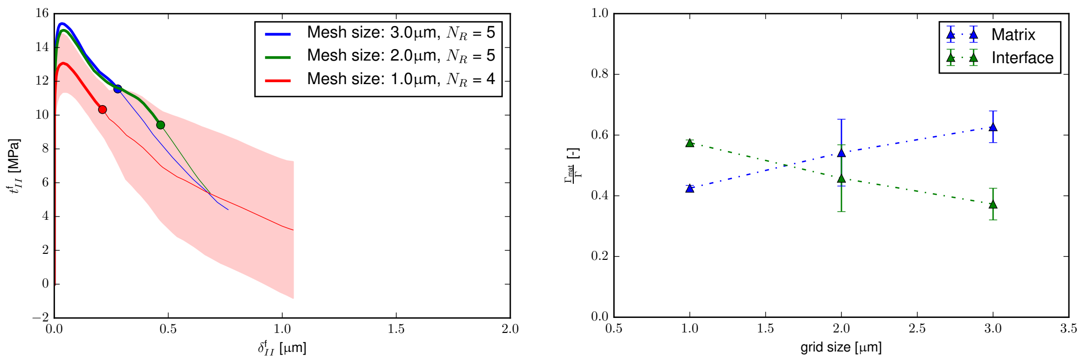

(a) ETSL transverse to the crack (mode II) **(b)** Crack content

Figure 5.31: Mixed mode loading with a volume element size of 100x100 μm

5.3.4 Mesh Convergence Remarks

In conclusion, it can be found that with increasing MVE size, the mesh size can become large, as the details become less prominent. For the pure shear and mixed mode loading case, a much smaller mesh size is required than for the constraint extension loading case. This is mainly attributed to the difficulty of the pure shear and mixed mode crack to grow.

Table 5.5: The converged mesh size for each MVE size and for each loading case

	Constraint Extension	Pure Shear	Mixed Mode
$25 \times 25\mu$m	3	1	2
$37.5 \times 37.5\mu$m	2	0.5	2
$50 \times 50\mu$m	1	0.5	0.5
$62.5 \times 62.5\mu$m	3	2	2
$75 \times 75\mu$m	3	1	1
$100 \times 100\mu$m	3	1	1

5.4 Interfiber Void Mesh Convergence

In order to determine the effect of the mesh size on the interfiber voids, a small mesh convergence study has been performed. It consists of a single interfiber void with three fibers. The loading condition both the constraint extension and pure shear case have been investigated. The mixed mode case has not been investigated as the effect of the mixed mode is assumed to be similar to a combination of the two other loading conditions. Both the effect of the mesh and the effect of the angle of the interfiber void will be investigated for each loading condition. The mesh of the three cases can be found in Figure 5.32.

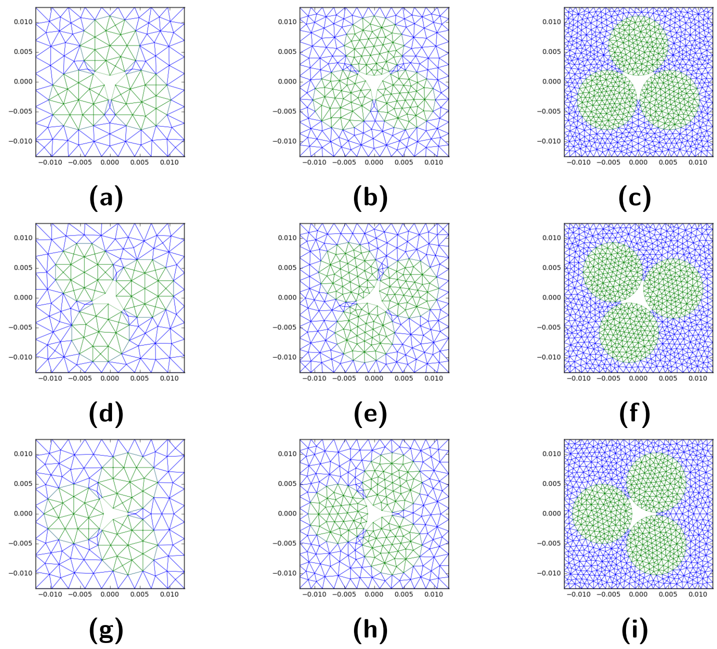

Figure 5.32: The mesh of the interfiber voids used to determine the convergence mesh size. From left to right the mesh size are $3 \cdot 10^{-3}\mu$m, $2 \cdot 10^{-3}\mu$m to $1 \cdot 10^{-3}\mu$m. From top to bottom the orientation θ of the interfiber void is $\theta = 0$ rad, $\frac{\pi}{4}$ rad and $\frac{\pi}{2}$ rad. These geometries are used for both the constraint extension and pure shear loading condition.

5.4.1 Constraint Extension loading case

For the three orientations the ETSL can be found in Figure 5.33. No clear convergence can be found when looking at the individual orientations. However, the influence of the angle of the interfiber void can be evaluated. When looking at different orientations, it can be seen that in the case of a mesh size of both 1μm and $2 \cdot \mu$m , the ETSL remains constant over the orientations. From this it is assumed that interfiber void mesh in the case of a constraint extension loading is converge red from a mesh size of 2μm.

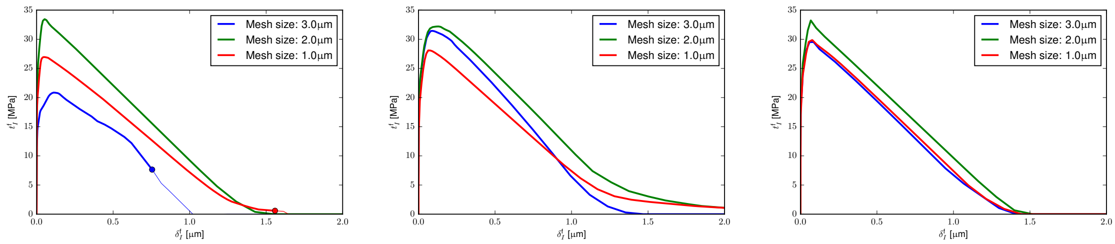

(a) $\theta = 0$ (b) $\theta = \frac{\pi}{4}$ (c) $\theta = \frac{\pi}{2}$

Figure 5.33: The ETSL for a single Interfiber void at different angles with a constraint extension boundary condition. The effect of the mesh size for each orientation is shown.

5.4.2 Pure Shear loading case

For the pure shear, the three orientations can be found in Figure 5.34. For both the interfiber void with orientation of 0° and 90° the mesh size of 1μm the simulation crashed before the crack was properly formed. From this no conclusion can be made for the mesh convergence. Resulting in the assumption that the mesh size as found in the MVE mesh convergence study is sufficient for the interfiber voids.

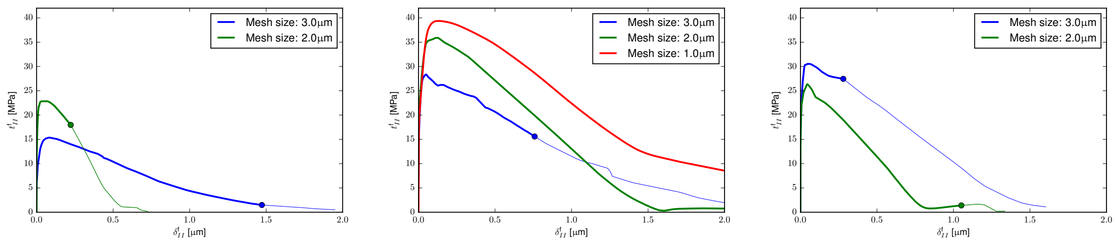

(a) $\theta = 0$ (b) $\theta = \frac{\pi}{4}$ (c) $\theta = \frac{\pi}{2}$

Figure 5.34: The ETSL for a single interfiber void at different angles with a pure shear boundary condition. The effect of the mesh size for each orientation is shown.

5.5 RVE Convergence

For the RVE convergence the method as presented by Gitman et al. [23] is used. The voids in the MVE influence the ETSL properties. Since these voids are randomly placed in the MVE, to determine the RVE the scatter on the ETSL properties is important. In the RVE convergence study, both the ETSL and the scatter of the ETSL properties are evaluated. The effective fracture (ultimate) strength and effective fracture energy are used to show the scatter. The MVEs with the converged mesh as presented previously in this chapter is used.

5.5.1 Constraint Extension

In the constraint extension case, the ETSL seems to have converged at a low volume element size. However, when looking at the individual parameters of the ETSL, the effective fracture strength converges at a rather low MVE size. The fracture energy requires a larger MVE size to converge. From this it is assumed that in the case of a constraint extension loading case, the volume element can be assumed to be representative at a size of 50×50 μm with a mesh size of 1μm.

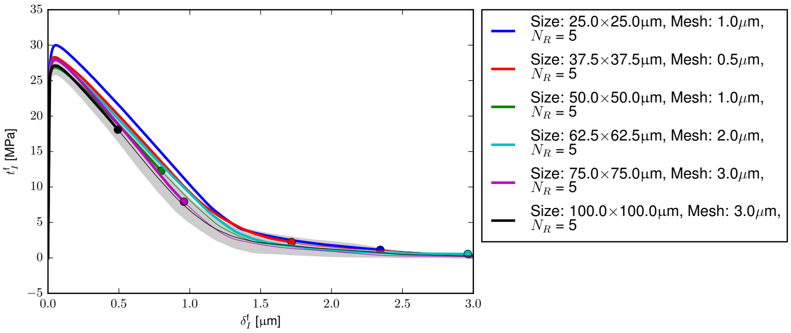

(a) The ETSL

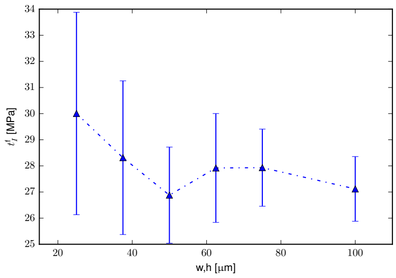

(b) The effective normal strength

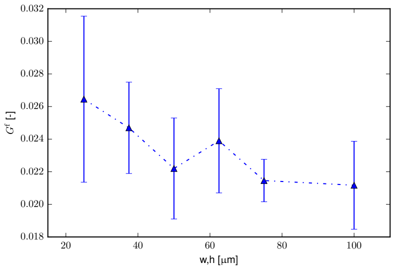

(c) The effective fracture energy

Figure 5.35: The RVE convergence study for a constraint extension loading case.

5.5.2 Pure Shear

In Figure 5.36a it can be found that there is a large deviation between the MVE size of $100 \times 100\mu$m and the other MVE sizes. Because of this the MVE size of $100 \times 100\mu$m is discarded in the convergence study.

For pure shear the scatter in the case of an MVE with the size of 62.5 μm or 75 μm, the standard deviation of the fracture energy is very large, as can be found in Figure 5.36c. This can mainly be explained by the fact that the convergence of these simulations is difficult, which results in the fact that some simulations can be cut early and the fracture energy is arbitrarily lower than expected. For the fracture strength little convergence can be found.

5.5.3 Mixed Mode

For the mixed mode again, similar to the pure shear loading case, the volume element of $100 \times 100\mu$m is discarded. When comparing the smaller MVE sizes, no clear convergence can be found. This can be seen in Figure 5.37

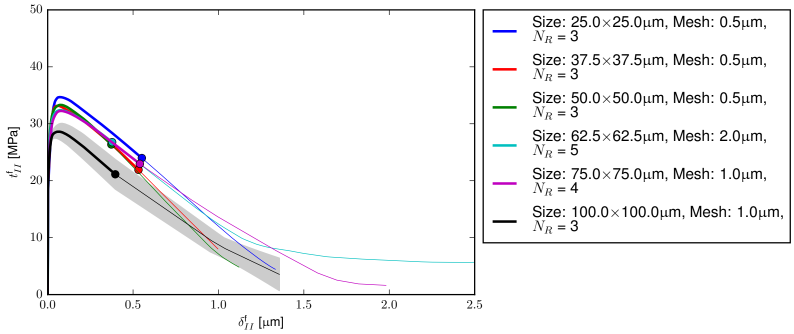

(a) The ETSL

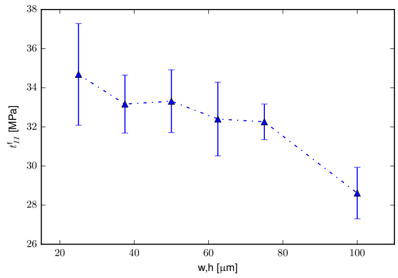

(b) The effective tangential strength

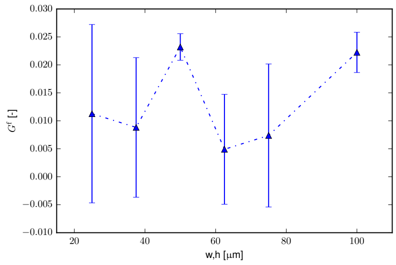

(c) The effective fracture energy

Figure 5.36: The RVE convergence study for a pure shear loading case.

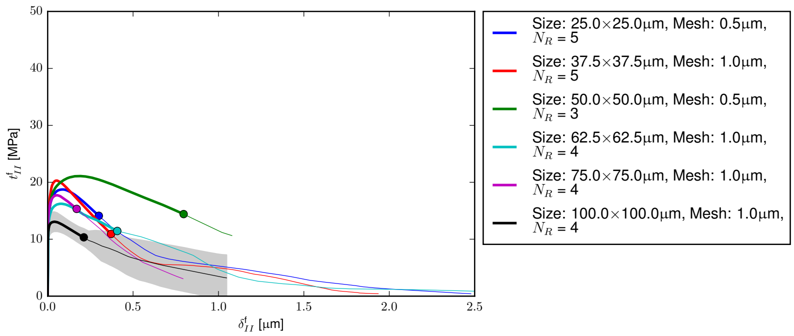

(a) The ETSL

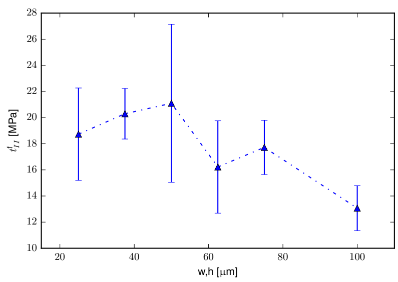

(b) The effective tangential strength

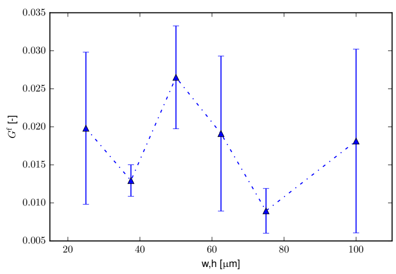

(c) The effective fracture energy

Figure 5.37: The RVE convergence study for a mixed mode loading case.

5.5.4 RVE Convergence Remarks

In both the pure shear and mixed mode loading case, the tangential properties at a volume element size of $100 \times 100\mu$m was found to deviate too much and was thus discarded.

Both the pure shear and mixed mode loading case show no clear convergence in the effective properties. It is assumed that the convergence will occur at larger MVE sizes than investigated here. No larger MVE sizes have been investigated due to the computational limitations of this project. In this study the MVE size of $75 \times 75\mu$m will be used. Yet further research is required on the RVE size. It is assumed here that the trends that are found using this MVE size are similar to that of the larger RVE.

For the constraint extension case. a clear convergence is found. Although it is convenient to take the same volume element size for all the load cases. In this case the same geometry can be used, resulting in less scatter between the different loading cases and speeds up the pre-processing. For all three loading cases a volume element of $75 \times 75\mu$m is used. The mesh size will also remain constant over the different loading cases to ensure that the mesh influence on the crack is equal on all loading cases, and is thus a mesh size of 1μm is used.

Chapter 6

Investigation of the different void parameters

In this chapter the investigation of the effect of the void parameters on the effective properties is discussed. First, the general idea behind the different studies are discussed in Section 6.1, and the three void cases are presented here. Using these three void cases the effect of the void parameter is determined. The results for each separate void case is discussed in Section 6.2 to Section 6.4. These three void cases are compared in Section 6.5. The concluding remarks are made in Section 6.6.

6.1 General Idea

In order to determine the effect of the sub-ply defects on the effective traction separation properties on the macroscale, three studies have been performed. All studies determine the effect of an increasing void content with different input parameters. The void contents that have been investigated are 0, 1, 2, 4, 6 and 8 %. For each study eight models with the same fiber distribution have been evaluated with increasing void content. These fiber distributions are unique for each loading case and are done to reduce the scatter per case. Examples of this can be found in the individual sections below.

The first study has matrix voids with nearly constant diameters. This is done to see the general effect of the matrix voids and to have a baseline for the two other studies. The second study aims to look at what the effect of the interfiber voids are on the effective properties. The third study aims to determine what the effect is of large matrix voids on the microscale. This is simulated by having a large deviation in the diameter of the voids. As presented in the previous chapter, all simulations will have a Microstructural Volume Element (MVE) size of $75 \times 75\mu$m. For both the pure shear and mixed mode, no Representative Volume Element (RVE) convergence was found. Due to computational limitations, this MVE size has been selected. As explained previously, it is assumed that the trends that are found with

Table 6.1: Loading cases and their deformation gradient

Loading Case	Deformation Gradient
Constraint Extension	$\begin{bmatrix} \gamma & 0 \\ 0 & 0 \end{bmatrix}$
Pure Shear	$\begin{bmatrix} \gamma & 0 \\ 0 & -\gamma \end{bmatrix}$
Mixed mode	$\begin{bmatrix} 2\gamma & 0 \\ 0 & -\gamma \end{bmatrix}$

this MVE size are similar to that of the trends with the larger RVE size. For each study the geometry is discussed in greater detail in each respective section.

For all the void cases, the three loading cases, as also done for the convergence study, are used. These are summarized in Table 6.1. For each loading case eight fiber distributions are made with increasing void content from 0 to 8 %. These eight realizations per void content ensure that sufficient realizations are available for the comparison.

For the output the Effective Traction Separation Law (ETSL) and their respective effective fracture strength and energy are shown. A relation between the fracture strength and energy is made using a second order polynomial fit for the energy and a linear fit for the effective fracture strength. These type of fits have been selected as they proved to be the most suitable for results of the specific parameters. Here, the fitting of the effective properties is mainly used to see the trend of the properties due to the increase in void content, while not looking for a true relation between the void content and effective properties. The color of the effective properties per void case is chosen to have the same color when comparing the different three void cases.

6.2 Constant diameter matrix voids

For the constant diameter matrix voids, the size of the voids has a small deviation of 0.1% and the aspect ratio ranges from 1 to 1.4. The average void size is calculated by dividing the total void content by the amount of voids present in the RVE, as is shown in Section 4.1.1. The number of voids is equal to six times the percentage of void content (2% results in 12 voids). Eight fibre distributions with each the six possible void content properties are created, and thus in total 48 models. Examples of the geometry with increasing void content are shown in Figure 6.1.

6.2.1 Constraint Extension

For the constraint extension case the ETSL, as is found in Figure 6.2a, are determined. The scatter of both the effective fracture strength and energy can be found in Figure 6.2b and Figure 6.2c respectively. From this, it is found that the effective fracture strength does not change with increasing void content. However, the effective fracture energy does show a clear decreasing trend with respect to the void content.

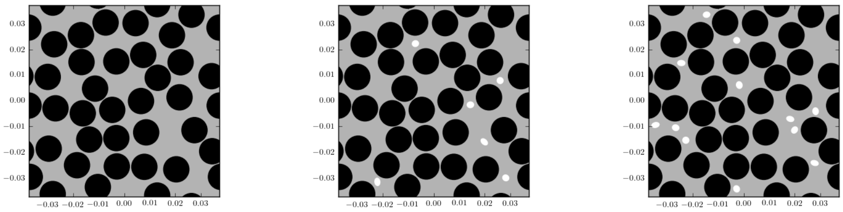

(a) Void content = 0.0 % **(b)** Void content = 1.0 % **(c)** Void content = 2.0 %

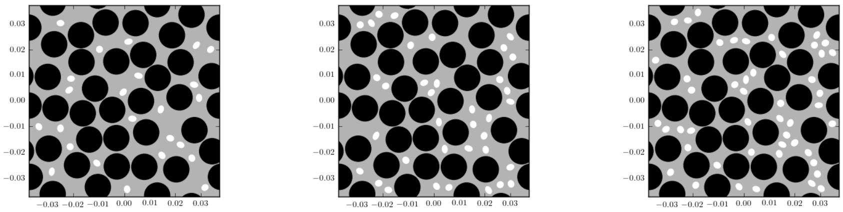

(d) Void content = 4.0 % **(e)** Void content = 6.0 % **(f)** Void content = 8.0 %

Figure 6.1: Increasing void content from 0 % (a) to 8 % in (e), here the void aspect ratio has a distribution of 1 to 1.4 and the size deviation is 1%

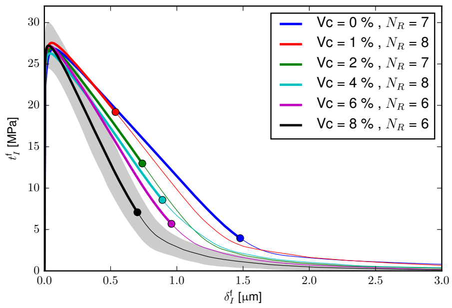

(a) The ETSL in normal direction

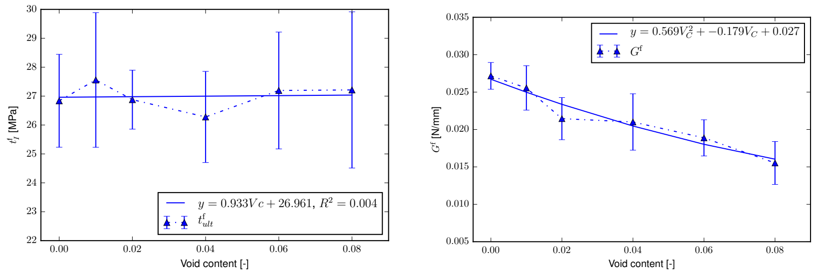

(b) The effective fracture strength **(c)** The effective fracture energy

Figure 6.2: The TSL and its fracture properties with respect to the void content for constant diameter voids with a constraint extension loading case. Here the properties are normal to the crack.

6.2.2 Pure Shear

For the pure shear loading case, the ETSL for each void content can be found in Figure 6.3a. First thing to notice here is that the number of realizations (N_R) is very low for the void content of 8%. This is due to the fact that either the model crashed before a periodic crack could fully form, or that the Hill-Mandel condition did not hold.

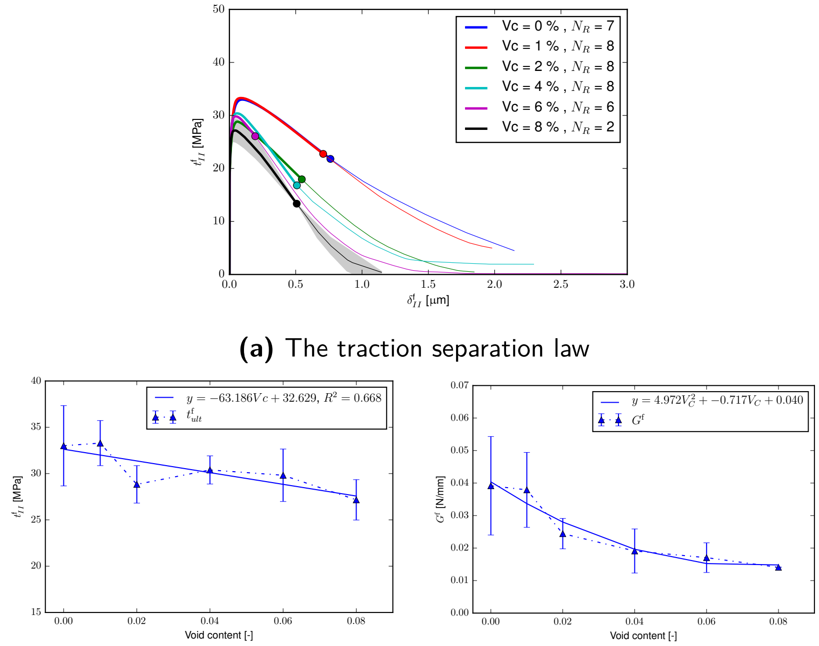

(a) The traction separation law

(b) The effective fracture strength **(c)** The effective fracture energy

Figure 6.3: The TSL and its fracture properties with respect to the void content for constant diameter voids with a pure shear loading case. Here the properties are tangential taken normal to the crack.

The effective fracture strength and energy can be found in Figure 6.3b and Figure 6.3c respectively. For both effective properties it can clearly be seen that there is a declining trend with increasing void content. Although at a void content of 1% the properties have barely decreased and are still within the standard deviation of the models without voids. From which it can be concluded to not have a significant effect on the properties at low void content, and a critical value is present. The effective properties also seem to flatten with increasing void content, which could be explained by the fact that at such high void contents, the crack can already form at such ease.

6.2.3 Mixed Mode

The mixed mode loading case shows a rather complicated crack path. The orientation of the crack is shown in Figure 6.4d. Here, it can be found that the crack angle has a small, yet not significant decrease. From the scatter it can be found that at low void contents the scatter is high, yet decreases with increasing void content.

The tangential ETSL and its properties can be found in Figure 6.4. For the tangential a clear decrease of the properties can be found, with a flattening of the fracture energy. Again, a critical value can be seen at a void content of 1%.

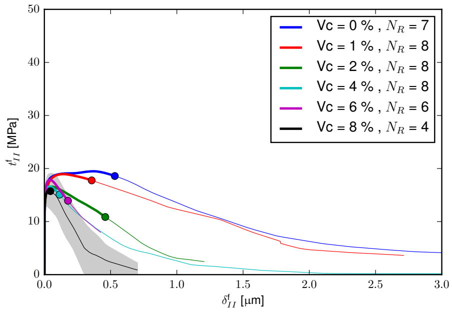

(a) The ETSL in tangential direction

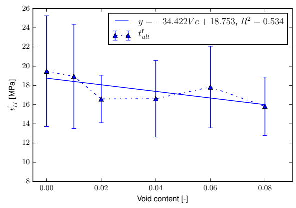

(b) The effective fracture strength

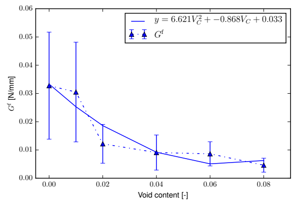

(c) The effective fracture energy

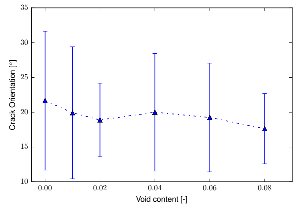

(d) The average crack orientation

Figure 6.4: The ETSL, its fracture properties and crack orientation with respect to the void content for constant diameter voids with a mixed mode loading case. Here the properties are tangential to the crack.

6.3 Interfiber voids

The interfiber voids have a discreet void content. In order to compare the results with the previous case, similar void contents are required. To ensure this matrix voids are added to the simulations of the interfiber void to reach the void content required. The percentage of interfiber voids to the total void content is around 25%. The parameters used are shown in Table 6.2.

Table 6.2: Input parameters for the interfiber void case

Void Content	0.0 %	1.0 %	2.0 %	4.0 %	6.0 %	8.0 %
InterFiber Voids	[-]	[3]	[3, 3]	[3, 3, 4]	[3, 3, 4, 4]	[3, 3, 4, 4, 4]
Number of voids	-	5	10	20	29	39

Here, the interfiber voids indicate whether a three fiber or four fiber interfiber void is present. The number of matrix voids is selected to ensure that the average matrix void size is equal to that of the previous study with the constant diameter matrix voids, while having the same void content. This is done to ensure the fact that the comparison between the constant diamater matrix voids and interfiber voids only has one parameter different, which is that 25% of the total void content are interfiber voids. Examples of this study can be found in Figure 6.5.

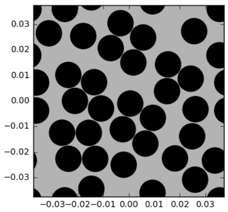

(a) Void content = 0.0 %

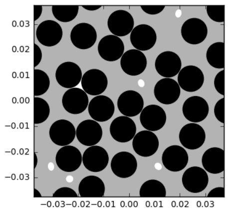

(b) Void content = 1.0 %

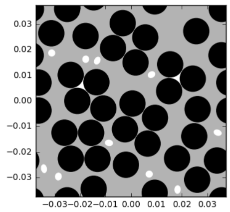

(c) Void content = 2.0 %

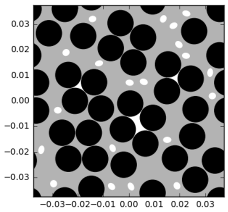

(d) Void content = 4.0 %

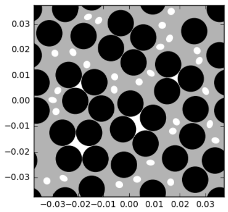

(e) Void content = 6.0 %

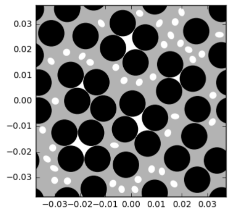

(f) Void content = 8.0 %

Figure 6.5: Increasing void content from 0 % (a) to 8 % in (e), here the void aspect ratio has a distribution of 1 to 1.4 and the size deviation of 1%

6.3.1 Constraint Extension

For the constraint extension loading case the ETSL and its properties can be found in Figure 6.6.

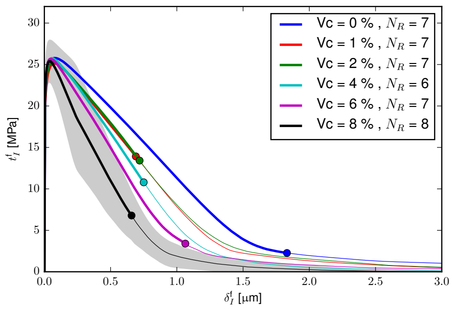

(a) The ETSL in normal direction of the crack

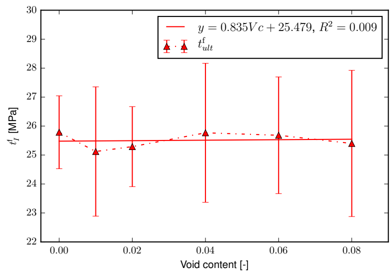

(b) The effective fracture strength

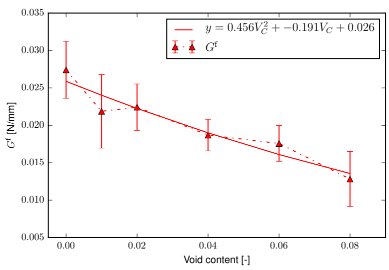

(c) The effective fracture energy

Figure 6.6: The TSL and its fracture properties with respect to the void content for constant diameter voids with a constraint extension loading case. Here the properties are normal to the crack.

The microscopic voids show to have little influence on the effective fracture strength , while for the fracture strength a clear , fairly linear, decrease can be found, as can be found in Figure 6.6b and Figure 6.6c.

6.3.2 Pure Shear

In the pure shear loading case for the interfiber voids both the fracture strength and fracture energy decrease, as can be found in Figure 6.7b and Figure 6.7c respectively. In this case the critical value of 1% is again obvious.

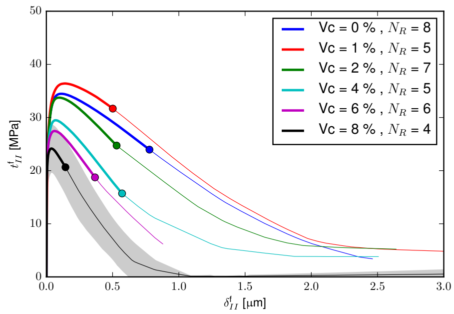

(a) The ETSL in tangential direction of the crack

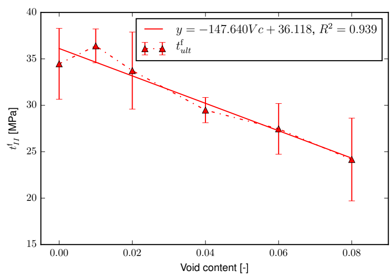

(b) The effective fracture strength

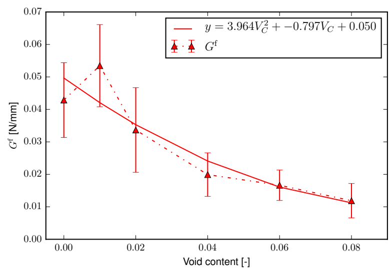

(c) The effective fracture energy

Figure 6.7: For the interfiber void case TSL and its fracture properties with respect to the void content for constant diameter voids with a shear loading case. Here the properties are normal to the crack.

6.3.3 Mixed Mode

At a void content of 4% the interfiber void with four fibers is used first. When looking at the orientation of the crack as shown in Figure 6.8d, the crack orientation decreases when these four fiber interfiber voids are first used.

For the fracture strength and energy, as shown in Figure 6.8b and Figure 6.8c respectively, both the strength and energy decrease with increasing void content.

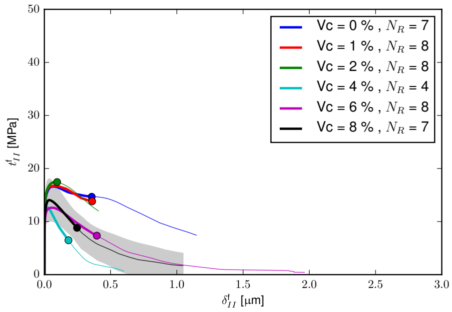

(a) The ETSL in tangential direction

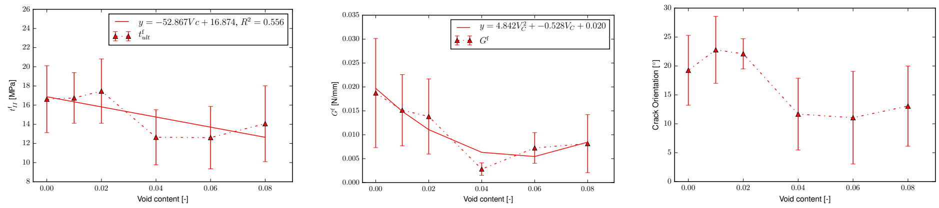

(b) The effective fracture strength **(c)** The effective fracture energy **(d)** The average crack orientation

Figure 6.8: The ETSL, its fracture properties and crack orientation with respect to the void content for constant diameter voids with a pure shear loading case. Here the properties are tangential taken normal to the crack.

6.4 Large range in diameter of the matrix voids

In order to determine whether the size of the matrix voids have an influence on the size of the voids is changed. A large deviation for the void diameter is used to have both small and large voids.

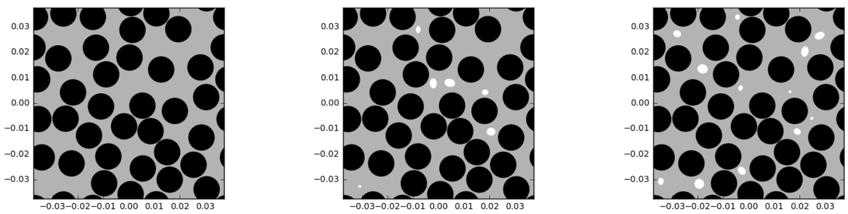

(a) Void content = 0.0 % **(b)** Void content = 1.0 % **(c)** Void content = 2.0 %

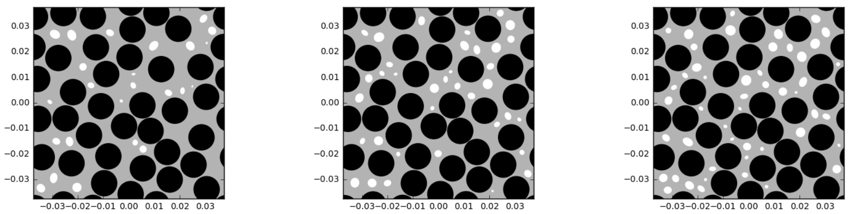

(d) Void content = 4.0 % **(e)** Void content = 6.0 % **(f)** Void content = 8.0 %

Figure 6.9: Increasing void content from 0 % (a) to 8 % in (e), here the void aspect ratio has a distribution of 1 to 1.4 and the size deviation is 83%

The deviation in size is now 83%, while the possible aspect ratio is kept constant at the range of 1 to 1.4. The number voids per void content is kept the same compared to the constant diameter voids. Examples for this configuration can be found in Figure 6.9.

6.4.1 Constraint Extension

For the constraint extension loading case, the effective properties and their scatter are found in Figure 6.10. From this it is found that there is no effect on the effective fracture strength when increasing the void content. The effective fracture energy does show a clear decline with increasing void content.

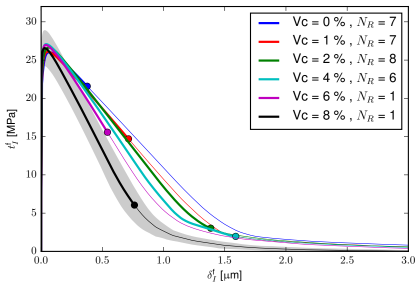

(a) The ETSL in normal direction of the crack

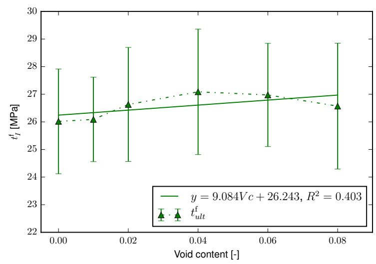

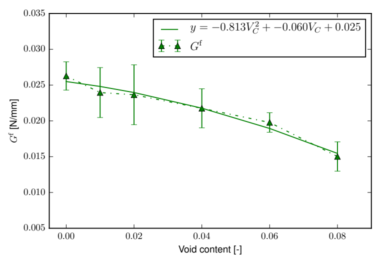

(b) The effective fracture strength **(c)** The effective fracture energy

Figure 6.10: The TSL and its fracture properties with respect to the void content for voids with a large devaition in diameter with a constraint extension loading case. Here the properties are normal to the crack.

6.4.2 Pure Shear

In the pure shear case that contains matrix voids with a large deviation in diameter, again the decrease in both the effective strength and energy is found, as is shown in Figure 6.11. A critical value can be seen for the fracture strength, at which until a void content of 2% the voids have little influence on the fracture strength, after which a clear decline can be seen.

6.4.3 Mixed Mode

For the effective fracture properties the fracture strength seem to stay rather constant with increasing void content while the fracture energy shows a clear decline, as is shown in Figure 6.12.

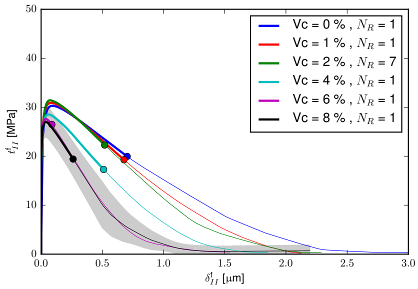

(a) The ETSL in tangential direction of the crack

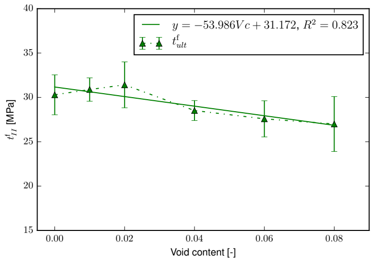

(b) The effective fracture strength

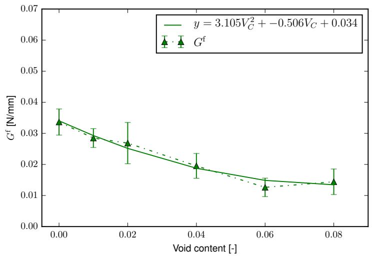

(c) The effective fracture energy

Figure 6.11: The TSL and its fracture properties with respect to the void content for voids with a large deviation in diameter with a pure shear loading case. Here the properties are normal to the crack.

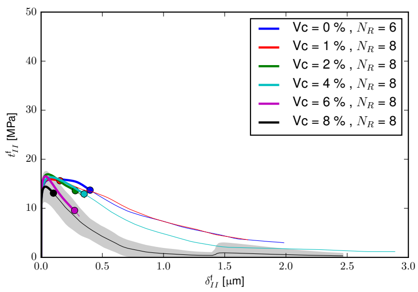

(a) The ETSL in tangential direction

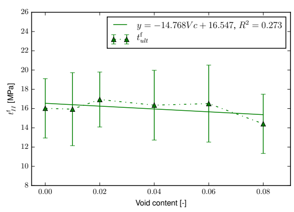

(b) The effective fracture strength

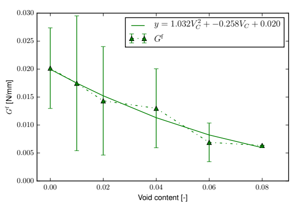

(c) The effective fracture energy

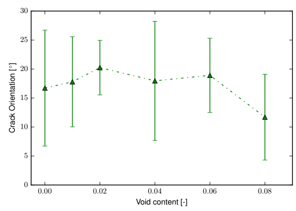

(d) The average crack orientation

Figure 6.12: The ETSL, its fracture properties and crack orientation with respect to the void content for constant diameter voids with a mixed mode loading case. Here the properties are tangential taken normal to the crack.

The orientation of the crack is found to be relatively constant with increasing void content, as is shown in Figure 6.12d.

6.5 Comparison of the different void case

In the previous section the three studies of the constant diameter void, interfiber voids and voids with a large deviation of diameter were presented separately. The comparion between these three casesis done below. The effective fracture strength and energy are compared per loading case.

6.5.1 Constraint Extension

The effective fracture strength can be found in Figure 6.13a. Here it can be seen that for the interfiber void case, the fracture strength is significantly lower. This is explained by the fact that the fibers in this case are forced into a fiber distribution with fiber rich and matrix rich regions on the microscale. These fiber and matrix rich regions resulted in an overall weaker volume element. During the RVE convergence, this was not taken into account. Since at a void content of 0% the volume elements should be the same, for each effective fracture property an average over all realizations is taken. This is indicated as the black marker henceforth. The fitting have been adapted to use this new initial value, as this new initial value is more representative than the individual initial values. The effective fracture energy for the constraint extension case can be found in Figure 6.13b. In this case all three different cases seem to be within the standard deviation of the other cases.

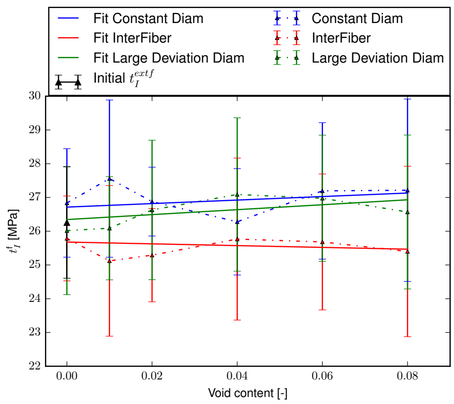

(a) The effective fracture strength

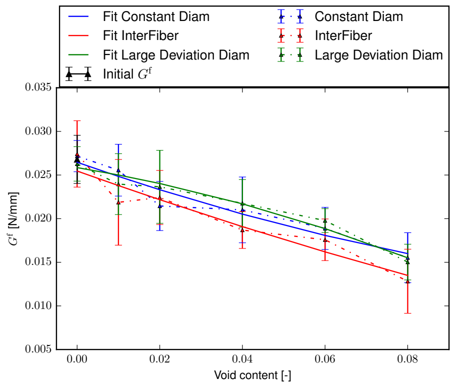

(b) The effective fracture energy

Figure 6.13: For the constraint extension loading case the effective properties of the three different studies

6.5.2 Pure Shear

When looking at the pure shear boundary condition, for the effective fracture strength, as shown in Figure 6.14a, there is a much larger decrease in the strength when looking at the interfiber voids compared to the matrix voids cases. This is because the interfiber voids have a larger influence on the initiation of the crack compared to these matrix voids, although when looking at the scatter it is only a small influence.

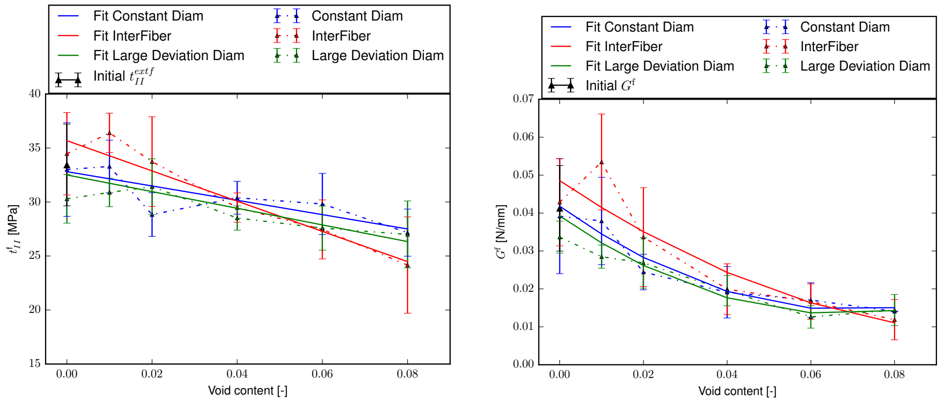

(a) The effective fracture strength **(b)** The effective fracture energy

Figure 6.14: For the pure shear loading case the effective properties of the three different studies

In Figure 6.14b the effective fracture energy can be found. Here energy at a void content of 0% seem to be fairly similar. The fit of the interfiber void seems to deviate a lot from the other cases, which is mainly caused by a large deviation at the 1% void content. At large void contents the fracture energy converge to one another.

6.5.3 Mixed Mode

The effective fracture strength tangential to the macroscopic crack is shown in Figure 6.15a.

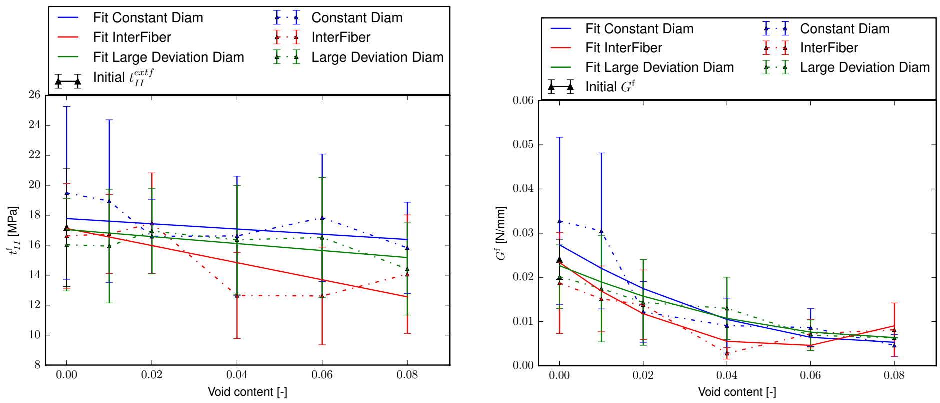

(a) The effective fracture strength **(b)** The effective fracture energy

Figure 6.15: For the mixed mode loading case the effective properties of the three different studies

When comparing the three fracture strengths as a function of the void content, little difference can be found when taken the scatter into account. For the fracture energy, as found in

Figure 6.15b, the same can be found. Although for the fracture strength the interfiber void properties are slightly lower due to the fiber distribution.

6.5.4 Discussion of the comparison

The difference between the three cases seems to be very minimal. Here in all three loading cases the properties have been within each others standard deviation and show the same trend. This shows that when looking at the influence of the sub-ply voids on the effective properties, the most important constant is the void content and the other microscale parameters seem to be second order.

When comparing the fracture energy of the pure shear loading case and constraint extension loading case, it can be found that the pure shear fracture energy is almost twice as high as the fracture energy for the constraint extension case. This can mainly be attributed to the fact of increasing viscosity due to the high compressive stresses caused by sliding of the crack.

6.6 Concluding remarks

In this chapter the results of three different void cases were presented, which were voids with nearly constant diameter, interfiber voids and large deviation of the diameter void.

For the constraint extension boundary condition all three cases show that the void content has little effect on the effective fracture strength. The effective fracture energy does show a significant decrease in its property. When comparing the three cases, it is found that there is little difference in terms of fracture energy. For the fracture strength the interfiber void case does show a significantly lower value compared to the other cases, which is mainly due to the fact that the interfiber voids force the fiber distribution for the volume element to have fiber rich and matrix rich regions.

For both the pure shear and mixed mode boundary condition it is found that the void content has a significant effect on the effective properties, while there is little difference between the different void cases. Because of this it can be concluded that when looking at sub-ply voids the most important parameter is the void content and the individual void parameters are only a second order parameter.

Chapter 7

Conclusions

7.1 Conclusion

During the manufacturing of fiber reinforced composites, defects can be created. These defects can often have a detrimental effect on the properties of the composite. In this project the effect of sub-ply defects, mainly voids, on the failure properties of the composite have been determined. The objective of the project is repeated below:

The objective of this MSc. Thesis it to determine the influence of sub-ply defects and its parameters to a micromechanically derived Traction-Separation Law (TSL), by using multiscale modeling with a computational homogenization technique and a cohesive zone damage model.

For the multiscale analysis, the method of Turteltaub et al. [53] is used. However, this method does not take defects on the microscale into account. Subsequently, this method had to be adapted. The defects on the microvoids resulted in an additional discontinuity on the microscale. This added an additional term in the strain tensor and finally in an additional requirement in the Hill-Mandel condition. Since it is assumed that the void has no outward pressure on the surrounding material i.e. the air inside the void has no influence on the material. The rate of work done on the voids also has to be zero. From the verification it is found that this rate of power is negligible.

The adapted theory had to be numerically implemented. The creation of the Microstructural Volume Element (MVE) is done using `python`, where the random mesh is generated using `gmsh`. The MVE created is able to generate the microstructure containing randomly distributed fibers, matrix voids and interfiber voids. The fracture mechanism is modeled using cohesive elements. The Finite Element (FE) model was then implemented into `Abaqus`®. Then `Abaqus`® is used to simulate the fracture in the microstructure. The microstructural fracture information is extracted from `Abaqus`® and used for the further processing and determination Effective Traction Separation Law (ETSL) for various configurations.

The Representative Volume Element (RVE) size was determined using the method as proposed by Gitman et al. [23]. The MVE size was increased until the fracture behavior was converged.

Both the RVE and mesh convergence was done for the three loading cases at a void content of 3%. For the pure shear and mixed mode loading case no RVE convergence was found. Due to the computational limitations the MVE size of $75 \times 75\mu$m was used for further research. It was assumed that the trends found at this MVE size are similar to that of the larger RVE.

Using this MVE size the effect of different void parameters was investigated. To do this three different void cases were simulated. Each void case is tested for a void content in the range of 0% to 8% for the three loading cases. To reduce the scatter for each void content eight volume elements are used. This resulted in 48 simulations per void case. The initial void case is a benchmark case containing nearly constant diameter matrix voids. The second void case is with 25% of the total void content being interfiber voids, where the effect of the interfiber voids on the fracture properties were investigated. Finally, the third case contains matrix voids with a large deviation in the diameter of the voids to investigate the effect of the larger voids in the microstructural volume element.

Overall, for the constraint extension loading case it can be found that the effective fracture strength remains constant with increasing void content. However, for the interfiber void case, the fracture strength is lower. This is mainly contributed to the fact that the interfiber voids have an arbitrary distribution of the fibers, resulting in fiber rich and matrix rich regions, which show an influence on the effective fracture strength. This effect was not taken into account during the RVE convergence. The fracture energy for the different void cases show a similar decline within the standard deviation of each other.

For the pure shear loading case for all three cases, the fracture strength shows a critical value at which the voids start to have an influence on the fracture strength after a void content of 1%. The fracture energy does not show this critical value. The interfiber void shows a sharper decline in the fracture strength which can be contributed due to the interfiber voids having a larger influence on the failure initiation.

The mixed mode loading cases shows a similar effect for the fracture strength with the interfiber void decreasing more compared to the other cases. In the mixed mode the critical value is also present.

From these three loading cases it can be concluded that the type of void does not have a significant influence on the effective properties and the main parameter is the void content, where the effective properties decrease significantly with increasing void content. The critical value seems to be mainly present in the tangential component (with respect to the macroscopic crack). The type of voids present on the sub-ply do not have a mayor influence on the effective fracture properties and can be seen as a second order variable.

7.2 Recommendations

The objective to determine the effect of sub-ply voids on the effective fracture properties has been achieved. The voids show the expected result of decreasing the effective fracture properties. To further improve the method, the following recommendations are made:

- Currently, the effective traction is defined using a best fit of the Hill-Mandel condition of the bulk averaged and crack averaged properties. This fitted value, α, is constant over the simulation. To further improve the method, in future research a more flexible method should be investigated, which results in a perfect fit between the macroscopic and microscopic properties over time.

- In a lot of the simulations, the viscous energy that is added by the automatic stabilization exceeds the threshold of 5%. As a result, the energy is dissipated in order to have a stable simulation. Removing this automatic stabilization results in the divergence and reducing the stabilization results in a very high computational cost. This has to be taken into account for further research or an advanced method to incorporate this effect in the homogenization could be researched.
- In this thesis, the MVE is on a 2-Dimensional (2D) plane. In order to model all the possible failure mechanisms and have a more accurate representation of the defects, a 3-Dimensional (3D) model could be developed. The presented theory is applicable to 3D with only minor changes.
- In this research to ensure the direction of the properties of the cohesive element, a reference vector is used. To properly select this reference vector, an initial guess of the crack normal has to be made. This dependency of the input on the output should be investigated and if possible be decoupled.

Different manufacturing defects can occur in a fiber reinforced composite. Currently, only the sub-ply voids have been investigated. To further investigate the effect of the manufacturing defects on the composite structure, further research can be done on the effect on the effective properties by for instance the following defects:

- Imperfect bonding between the fibers and matrix. From the literature study it was found that parts of a fiber can be improperly bonded to the matrix due the fiber not being processed correctly before combining the fiber and matrix [15].
- Fiber weaving or misalignment of the fibers, in this case the longitudinal plane on the microscale will have to be used.
- The effect of the bonding between two plies and possible defects on this interface. Currently this effect of the bonding between two plies is being investigated using a 2D model.

In this research it has been assumed that the internal pressure of the voids is negligible. The theory that was developed is however able to model this effect. Further research can be done on the effect of this internal pressure on the failure mechanisms on the microscale. As this internal pressure can be possible for specific manufacturing techniques.

References

[1] *Abaqus Analysis User Guide*, Abaqus 6.14 edition.

[2] M. Alfano, F. Furgiuele, A. Leonardi, C. Maletta, and G. H. Paulino. Cohesive zone modeling of mode i fracture in adhesive bonded joints, 2007.

[3] M. V. C. Alfaro, A. S. J. Suiker, C. V. Verhoosel, and R. de Borst. Numerical homogenization of cracking processes in thin fibre-epoxy layers. *European Journal of Mechanics a-Solids*, 29(2):119–131, 2010.

[4] G. I. Barenblatt. The mathematical theory of equilibrium cracks in brittle fracture. *Advances in Applied Mechanics*, 7:55–129, 1962.

[5] T. Belytschko, W. K. Liu, B. Moran, and K. Elkhodary. *Nonlinear Finite Elements for Continua and Structures.* John Wiley & Sons Ltd., Hoboken, NJ, 2nd edition, 2003. ISBN:978-1-119-63270-3.

[6] D. S. Brauer, C. Rüssel, S. Vogt, and M. Schnabelrauch. Degradable phosphate glass fiber reinforced polymer matrices: Mechanical properties and cell response. *J. Mater. Sci. Mater. Med.*, 19(1):121–127, 2008.

[7] G. T. Camacho and M. Ortiz. Computational modelling of impact damage in brittle materials. *International Journal of Solids and Structures*, 33(20-22):2899–2938, 1996.

[8] A. R. Chambers, J. S. Earl, C. A. Squires, and M. A. Suhot. The effect of voids on the flexural fatigue performance of unidirectional carbon fibre composites developed for wind turbine applications. *International Journal of Fatigue*, 28(10):1389–1398, 2006.

[9] E. W. C. Coenen, V. G. Kouznetsova, E. Bosco, and M. G. D. Geers. A multi-scale approach to bridge microscale damage and macroscale failure: a nested computational homogenization-localization framework. *International Journal of Fracture*, 178(1-2):157–178, 2012.

[10] E. W. C. Coenen, V. G. Kouznetsova, and M. G. D. Geers. Multi-scale continuous-discontinuous framework for computational-homogenization-localization. *Journal of the Mechanics and Physics of Solids*, 60(8):1486–1507, 2012.

[11] E. W. C. Coenen, V. G. Kouznetsova, and M. G. D. Geers. Novel boundary conditions for strain localization analyses in microstructural volume elements. *International Journal for Numerical Methods in Engineering*, 90(1):1–21, 2012.

[12] A. Cornec, I. Scheider, and K. H. Schwalbe. On the practical application of the cohesive model. *Engineering Fracture Mechanics*, 70(14):1963–1987, 2003.

[13] M. L. Costa, S. F. M. de Almeida, and M. C. Rezende. The influence of porosity on the interlaminar shear strength of carbon/epoxy and carbon/bismaleimide fabric laminates. *Composites Science and Technology*, 61(14):2101–2108, 2001.

[14] *CYCOM 5320-1 Epoxy Resin System.* Cytec Industries Inc., 2014. Rev. October 2015.

[15] G. de Jong. A review of state-of-the-art multiscale methods, cohesive zone modeling and typical voids in fibre-reinforced composites. Literature report, Delft University of Technology (TU Delft), Delft, May 2017.

[16] D. S. Dugdale. Yielding of steel sheets containing slits. *Journal of the Mechanics and Physics of Solids*, 8(2):100–104, 1960.

[17] M. Elices, G. V. Guinea, J. Gomez, and J. Planas. The cohesive zone model: advantages, limitations and challenges. *Engineering Fracture Mechanics*, 69(2):137–163, 2002.

[18] H. D. Espinosa and P. D. Zavattieri. A grain level model for the study of failure initiation and evolution in polycrystalline brittle materials. part i: Theory and numerical implementation. *Mechanics of Materials*, 35(3-6):333–364, 2003.

[19] P. Evesque. Fluctuations, correlations and representative elementary volume (REV) in granular materials. *Poudres Grains*, 11:6–17, 2000.

[20] P. H. Geubelle and J. S. Baylor. Impact-induced delamination of composites: a 2d simulation. *Composites Part B-Engineering*, 29(5):589–602, 1998.

[21] C. Geuzaine and J.-F. Remacle. *Gmsh Reference Manual*, April 2017. `gmsh` 3.0.

[22] S. R. Ghiorse. Effect of void content on the mechanical-properties of carbon epoxy laminates. *Sampe Quarterly-Society for the Advancement of Material and Process Engineering*, 24(2):54–59, 1993.

[23] I. M. Gitman, H. Askes, and L. J. Sluys. Representative volume: Existence and size determination. *Engineering Fracture Mechanics*, 74(16):2518–2534, 2007.

[24] Y. K. Hamidi, L. Aktas, and M. C. Altan. Formation of microscopic voids in resin transfer molded composites. *Journal of Engineering Materials and Technology-Transactions of the Asme*, 126(4):420–426, 2004.

[25] Z. Hashin. Analysis of Composite Materials - A Survey. *J. Appl. Mech.*, 50(3):481–505, 1983.

[26] *HexTow® IM7.* Hexcel Corporation, 2016.

[27] R. Hill. Elastic Properties of Reinforced Solids: Some Theoretical Principles. *J. Mech. Phys. Solids*, 11(5):357–372, 1963.

[28] C Hirch. Multiscale mixed-mode fracture analysis and deduction of effective traction-separation relations for anisotropic composites. Master's thesis, TU Delft and Technische UniversitÃďt Dresden, 2017. MSc, Thesis.

[29] H. Huang and R. Talreja. Effects of void geometry on elastic properties of unidirectional fiber reinforced composites. *Composites Science and Technology*, 65(13):1964–1981, 2005.

[30] H. Jeong. Effects of voids on the mechanical strength and ultrasonic attenuation of laminated composites. *Journal of Composite Materials*, 31(3):276–292, 1997.

[31] Varavara G. Kouznetsoave. *Computational homogenization for the multi-scale analysis of multi-phase materials*. PhD thesis, Technical university of Eindhoven, 2002.

[32] V. Kouznetsova, M. G. D. Geers, and W. A. M. Brekelmans. Multi-scale constitutive modelling of heterogeneous materials with a gradient-enhanced computational homogenization scheme. *International Journal for Numerical Methods in Engineering*, 54(8): 1235–1260, 2002.

[33] M. G. Kulkarni, K. Matous, and P. H. Geubelle. Coupled multi-scale cohesive modeling of failure in heterogeneous adhesives. *International Journal for Numerical Methods in Engineering*, 84(8):916–946, 2010.

[34] S. E. Leon, D. W. Spring, and G. H. Paulino. Reduction in mesh bias for dynamic fracture using adaptive splitting of polygonal finite elements. *International Journal for Numerical Methods in Engineering*, 100(8):555–576, 2014. ISSN 1097-0207. doi: 10.1002/nme.4744. URL http://dx.doi.org/10.1002/nme.4744.

[35] L. Lin, J. Chen, X. A. Zhang, and X. M. Li. A novel 2-d random void model and its application in ultrasonically determined void content for composite materials. *Ndt and E International*, 44(3):254–260, 2011.

[36] L. Maragoni, P. A. Carraro, and M. Quaresimin. Effect of voids on the crack formation in a 45/-45/0 (s) laminate under cyclic axial tension. *Composites Part a-Applied Science and Manufacturing*, 91:493–500, 2016.

[37] C. Miehe. Strain-driven homogenization of inelastic microstructures and composites based on an incremental variational formulation. *Int. J. Numer. Meth. Engng*, 55(11): 1285–1322, 2002.

[38] V. P. Nguyen. Discontinuous galerkin/extrinsic cohesive zone modeling: Implementation caveats and applications in computational fracture mechanics. *Engineering Fracture Mechanics*, 128:37–68, 2014.

[39] Vinh Phu Nguyen. An open source program to generate zero-thickness cohesive interface elements. *Advances in Engineering Software*, 74:27 – 39, 2014. ISSN 0965-9978. doi: https://doi.org/10.1016/j.advengsoft.2014.04.002. URL http://www.sciencedirect.com/science/article/pii/S0965997814000660.

[40] Vinh Phu Nguyen, Martijn Stroeven, and Lambertus Johannes Sluys. Multiscale continuous and discontinuous modelling of heterogeneous materials: A review on recent developments. *Journal of Multiscale Modelling*, 3(4):229 – 270, 2011. ISSN 1756-9737. doi: 10.1142/S1756973711000509.

[41] M. Ortiz and A. Pandolfi. Finite-deformation irreversible cohesive elements for three-dimensional crack-propagation analysis. *International Journal for Numerical Methods in Engineering*, 44(9):1267–1282, 1999.

[42] M. Ostoja-Starzewski. Microstructural randomness versus representative volume element in thermomechanics. *J. Appl. Mech.*, 69(1):25–35, 2002.

[43] K. Park and G. H. Paulino. Cohesive zone models: A critical review of traction-separation relationships across fracture surfaces. *Applied Mechanics Reviews*, 64(6), 2011.

[44] Kyoungsoo Park, Habeun Choi, and Glaucio H. Paulino. Assessment of cohesive traction-separation relationships in abaqus: A comparative study. *Mechanics Research Communications*, 78:71 – 78, 2016. ISSN 0093-6413. doi: https://doi.org/10.1016/j.mechrescom.2016.09.004. URL http://www.sciencedirect.com/science/article/pii/S0093641316301628. Recent Advances in Multiscale, Multifunctional and Functionally Graded Materials.

[45] Per-Erik Petersson. *Crack growth and development of fracture zones in plain concrete and similar materials*. PhD thesis, Lund University, 1981.

[46] Timon Rabczuk. Computational methods for fracture in brittle and quasi-brittle solids: State-of-the-art review and future perspectives. *ISRN Applied Mathematics*, 2013:38, 2013.

[47] A. Reuss. Berechnung der Fließgrenze von Mischkristallen auf Grund der Plastizitätsbedingung für Einkristalle. *Zeitschrift für Angewandte Mathematik und Mechanik*, 9:49–58, 1929.

[48] J. J. Rimoli and J. J. Rojas. Meshing strategies for the alleviation of mesh-induced effects in cohesive element models. *INTERNATIONAL JOURNAL OF FRACTURE*, 193(1): 29–42, MAY 2015. ISSN 0376-9429. doi: {10.1007/s10704-015-0013-6}.

[49] I. Scheider and W. Brocks. Simulation of cup-cone fracture using the cohesive model. *Engineering Fracture Mechanics*, 70(14):1943–1961, 2003.

[50] J. Summerscales. *Microsctructural characterisation of fibre-reinforced composites*. Woodhead Publishing Limited, Cambridge, England, 1998.

[51] J. M. Tang, W. I. Lee, and G. S. Springer. Effects of cure pressure on resin flow, voids, and mechanical-properties. *Journal of Composite Materials*, 21(5):421–440, 1987.

[52] P. V. Trusov and I. E. Keller. *The Theory of Constitutive Relations. Part I.* Perm State Technical University, Perm, 1997. [in Russian].

[53] S. Turteltaub, N. van Hoorn, W Westbroek, and C. Hirsch. Multiscale mixed-mode failure criterion and traction-separation relation for composite materials. 2017. Preprint submitted.

[54] V. Tvergaard. Effect of fiber debonding in a whisker-reinforced metal. *Materials Science and Engineering a-Structural Materials Properties Microstructure and Processing*, 125 (2):203–213, 1990.

[55] V. Tvergaard and J. W. Hutchinson. The influence of plasticity on mixed-mode interface toughness. *Journal of the Mechanics and Physics of Solids*, 41(6):1119–1135, 1993.

[56] D. A. Vajari. *Micromechanical failure in fiber-reinforced composites*. PhD thesis, Technical University of Denmark, 2014.

[57] D. A. Vajari. A micromechanical study of porous composites under longitudinal shear and transverse normal loading. *Composite Structures*, 125:266–276, 2015.

[58] D. A. Vajari, B. N. Legarth, and C. F. Niordson. Micromechanical modeling of unidirectional composites with uneven interfacial strengths. *European Journal of Mechanics a-Solids*, 42:241–250, 2013.

[59] D. A. Vajari, C. Gonzalez, J. Llorca, and B. N. Legarth. A numerical study of the influence of microvoids in the transverse mechanical response of unidirectional composites. *Composites Science and Technology*, 97:46–54, 2014.

[60] N. van Hoorn. Multiscale fracture simulations for composite materials; developing a failure criterion: Proof of concept. Master's thesis, Delft University of Technology, 2016.

[61] C. V. Verhoosel, J. J. C. Remmers, M. A. Gutierrez, and R. de Borst. Computational homogenization for adhesive and cohesive failure in quasi-brittle solids. *International Journal for Numerical Methods in Engineering*, 83(8-9):1155–1179, 2010.

[62] O. Vinogradov. On a representative volume in the micromechanics of particulate composites. *Mechanics of Composite Materials*, 37(3):245–250, May 2001. ISSN 1573-8922. doi: 10.1023/A:1010646702365. URL https://doi.org/10.1023/A:1010646702365.

[63] W. Voigt. Über die Beziehung zwischen den beiden Elasticitätconstanten isotroper Körper. *Annalen der Physik*, 274:573–587, 1889.

[64] W. Westbroek. Multiscale Modeling of Fracture in Composites; A progressive failure model for cryogenic Applications. Master's thesis, TU Delft, Delft, July 2017.

[65] F. H. Wittmann, K. Rokugo, E. BrÃijhwiler, H. Mihashi, and P. Simonin. Fracture energy and strain softening of concrete as determined by means of compact tension specimens. *Materials and Structures*, 21(1):21–32, 1988. ISSN 1871-6873. doi: 10.1007/bf02472525. URL https://doi.org/10.1007/BF02472525.

[66] Y. L. Yu, J. R. Ye, Y. Wang, B. M. Zhang, and G. C. Qi. A mesoscale ultrasonic attenuation finite element model of composites with random-distributed voids. *Composites Science and Technology*, 89:44–51, 2013.

[67] Zhengyu (Jenny) Zhang, Glaucio H. Paulino, and Waldemar Celes. Extrinsic cohesive modelling of dynamic fracture and microbranching instability in brittle materials. *International Journal for Numerical Methods in Engineering*, 72(8):893–923, 2007. ISSN 1097-0207. doi: 10.1002/nme.2030. URL http://dx.doi.org/10.1002/nme.2030.